Relation between growth rate, material quality, and device grade condition for intrinsic microcrystalline silicon:

From layer investigation to the application to thin-film tandem solar cells

Stephan Yann Michard

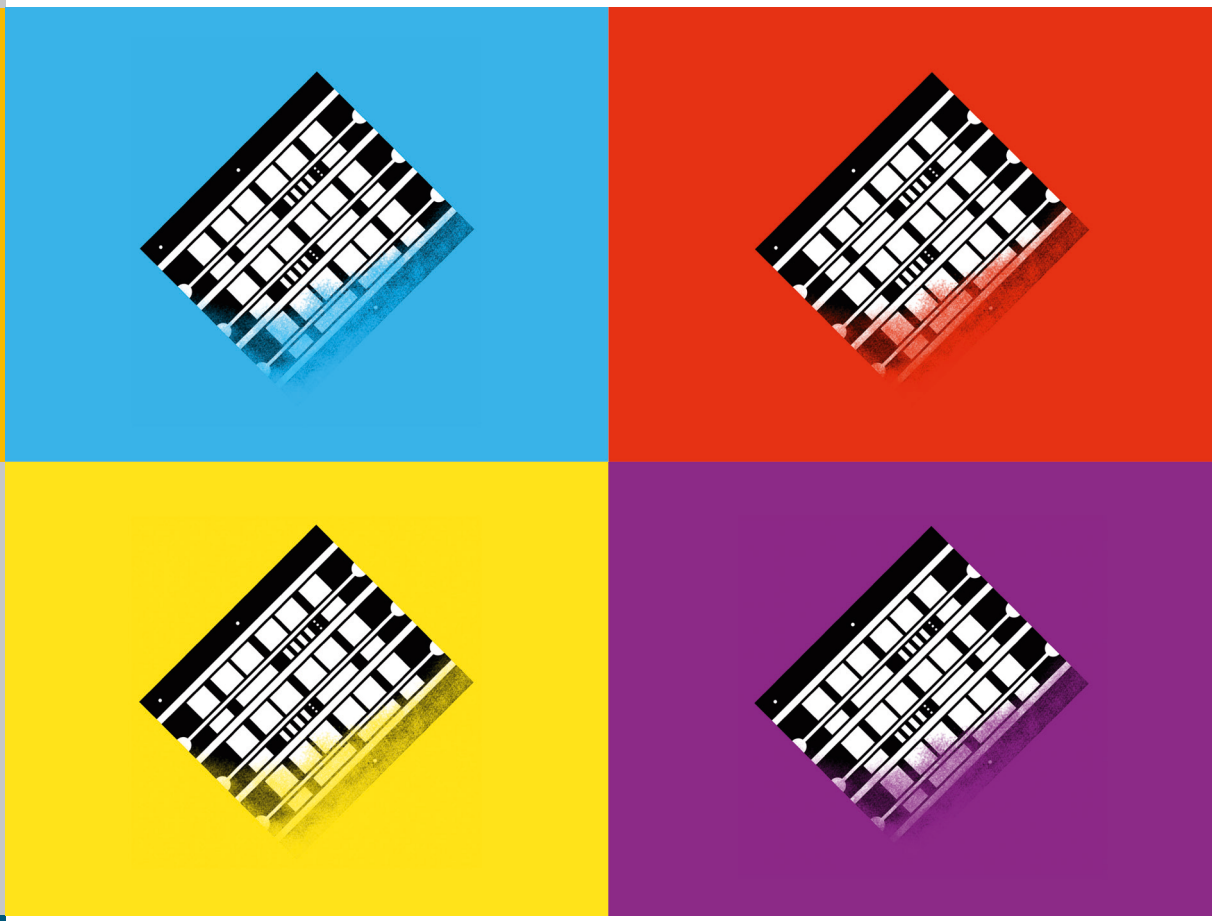

Energie & Umwelt / Energy & Environment
Band / Volume 259
ISBN 978-3-95806-048-7

JÜLICH
FORSCHUNGSZENTRUM

Schriften des Forschungszentrums Jülich
Reihe Energie & Umwelt / Energy & Environment Band / Volume 259

Forschungszentrum Jülich GmbH
Institute of Energy and Climate Research
IEK-5 Photovoltaics

Relation between growth rate, material quality, and device grade condition for intrinsic micro-crystalline silicon:

From layer investigation to the application to thin-film tandem solar cells

Stephan Yann Michard

Schriften des Forschungszentrums Jülich
Reihe Energie & Umwelt / Energy & Environment Band / Volume 259

ISSN 1866-1793 ISBN 978-3-95806-048-7

Bibliographic information published by the Deutsche Nationalbibliothek.
The Deutsche Nationalbibliothek lists this publication in the Deutsche
Nationalbibliografie; detailed bibliographic data are available in the
Internet at http://dnb.d-nb.de.

Publisher and Distributor: Forschungszentrum Jülich GmbH
Zentralbibliothek
52425 Jülich
Tel: +49 2461 61-5368
Fax: +49 2461 61-6103
Email: zb-publikation@fz-juelich.de
www.fz-juelich.de/zb

Cover Design: Grafische Medien, Forschungszentrum Jülich GmbH

Printer: Grafische Medien, Forschungszentrum Jülich GmbH

Schriften des Forschungszentrums Jülich
Reihe Energie & Umwelt / Energy & Environment, Band / Volume 259

D 82 (Diss. RWTH Aachen University, 2015)

ISSN 1866-1793
ISBN 978-3-95806-048-7

The complete volume is freely available on the Internet on the Jülicher Open Access Server (JuSER)
at www.fz-juelich.de/zb/openaccess.

The research described in this dissertation was supported partly by the "Bundesministerium für Umwelt, Naturschutz und Reaktorsicherheit" (Project "Quick μc-Si", Contract No. 0325260C). A part of this work was carried out in the framework of the FP 7 project "Fast Track", funded by the European Union under grant agreement No. 283501.

Stephan Yann Michard
Dissertation - RWTH Aachen University

The manuscript was composed with the typesetting system LaTeX using the "Legrand Orange Book" template created by Mathias Legrand made publicly available through "`www.latextemplates.com`" (October 2013).

Apart from the pictures listed below the copyright of the pictures heading each chapter is either owned by the Forschungszentrum Jülich GmbH or the author of this thesis:

- Contents: "Water drop 2" by Bill Brine licensed under CC BY 2.0 (`https://www.flickr.com/photos/8099556@N08/3576638958/`)
- Introduction: "Earth at Night" by Michael Coté licensed under CC BY 2.0 (`http://www.flickr.com/photos/cote/67919646/`)
- Conclusion: "earth" by Beth Scupham licensed under CC BY 2.0 (`https://www.flickr.com/photos/bethscupham/7663247816/`)
- List of Figures: "Coloured pencil" by Johann Dréo licensed under CC BY-SA 2.0 (`https://www.flickr.com/photos/nojhan/3391216263/`)
- List of Tables: "Ruler" by Scott Akerman licensed under CC BY 2.0 (`https://www.flickr.com/photos/sterlic/4299631538/`)
- Bibliography: "Library" by Stewart Butterfield licensed under CC BY 2.0 (`https://www.flickr.com/photos/stewart/99129170`)
- Publications List: "Paper pile - April 2011" by Sebastien Wiertz licensed under CC BY 2.0 (`https://www.flickr.com/photos/wiertz/5624281846`)

Details on the licensing terms of the Creative Commons initiative can be found online (`https://creativecommons.org/licenses/by/2.0/` or `https://creativecommons.org/licenses/by-sa/2.0/`).

First printing, May 2014

Abstract

Investigations on the relation between the growth rate, material quality, and device grade condition for intrinsic microcrystalline silicon is presented in this thesis. Hydrogenated microcrystalline silicon deposited by plasma enhanced chemical vapor deposition is a widely used material for the absorber layer of the bottom solar cell in silicon thin-film tandem solar cells. Microcrystalline silicon is a mixed phase material consisting of crystal grains, amorphous phase, grain boundaries, and voids. To guarantee sufficient light absorption absorber layer thicknesses of more than $1\,\mu m$ to $3\,\mu m$ are required for the absorber layer of the bottom solar cell. The increase of the deposition rate for intrinsic microcrystalline silicon is one essential point for cost reduction in the mass production of thin-film solar cells. The combination of excitation frequencies in the very high frequency range altogether with the application of the high pressure depletion regime enabled to reach deposition rates up to $2.8\,nm/s$ for optimal phase mixture material, which is until today considered to be of device grade quality. According to conductivity, electron spin resonance, and Raman measurements the quality properties of the material deposited at high deposition rates is similar to reference material deposited at low deposition rates. Nevertheless this material showed to be susceptible to oxygen uptake, which was shown to occur along the grain boundaries. Furthermore a decrease in crystal grain size with a simultaneous increase in tensile stress was observed by X-ray diffraction and Raman measurements, respectively. Thickness dependent Raman measurements showed a decrease in incubation layer thickness with increasing deposition rate. The investigations performed by X-ray diffraction and thickness dependent Raman measurements were supported by investigations performed with transmission electron microscopy. With this work it was found that the present criteria to classify microcrystalline silicon being of device grade quality should be extended for deposition rates beyond $1\,nm/s$. In addition to the measures describing the optimal phase mixture quantities describing the materials microstructure, the tendency for oxygen uptake, and the mechanical stress should be taken into account.

The device performance of microcrystalline thin-film single junction as well as of amorphous / microcrystalline thin-film tandem solar was observed to decrease with increasing deposition rate. The decrease in device performance was shown to be either related to inferior material quality of the microcrystalline absorber layer with increasing deposition rate and to an impairment of the pi-interface of the microcrystalline (sub) solar cell. Simulations on the impact of ions in matter showed that a damage of the pi-interface by ion bombardment is unlikely. As possible sources for the impairment of the pi-interface a variation of the nucleation conditions and structural inhomogeneities at the substrate/film interface are discussed. Despite the decrease in device performance

of the amorphous / microcrystalline thin-film tandem solar cells calculations showed that the output of deposition systems in produced Watt per hour can be increased by more than a factor of two. An increase in system output leads to a decrease in costs per produced unit and can lead to a decrease in initial investment costs.

Zusammenfassung

In dieser Arbeit wird der Zusammenhang zwischen der Depositionsrate, der Materialqualität und der Eignung für die Herstellung von Dünnschichtsolarzellen von intrinsischem mikrokristallinem Silizium beschrieben. Das durch die chemische Gasphasenabscheidung hergestellte hydrogenisierte mikrokristalline Silizium ist ein weiterverbreitetes Materialsystem für die Absorberschicht der Bottom-Solarzelle einer Silizium-Dünnschicht Tandem-Solarzelle. Mikrokristallines Silizium ist ein Phasengemisch bestehend aus kristallinen Säulen, amorpher Phase, Korngrenzen und Leerstellen. Zur Gewährleistung einer ausreichenden Absorption des Lichtes werden, aufgrund der indirekten Bandlücke von mikrokristallinem Silizium, Schichtdicken jenseits von $1\,\mu m$ bis $3\,\mu m$ für die Absorberschicht benötigt. Die Steigerung der Depositionsrate ist ein wesentlicher Ansatzpunkt für die Reduktion der Herstellungskosten von Dünnschicht-Solarzellen. Die Verwendung von Anregungsfrequenzen jenseits von $13.56\,MHz$ sowie die Anwendung eines Depositionsregimes mit hohen Prozessdrücken und einer hohen Gasausnutzung ermöglichen Depositionsraten bis zu $2.8\,nm/s$ für das Material des optimalen Phasengemischs. Dieses wird allgemein akzeptiert als geeignet für den Einsatz in Dünnschicht-Solarzellen angesehen. Die Ergebnisse von Leitfähigkeits, Elektronenspinresonanz und Raman-Messungen weisen ähnliche Werte wie jene des Referenzmaterials, welches bei niedrigen Depositionsraten hergestellt wurde, auf. Jedoch zeigt das Material eine Tendenz zur Sauerstoffaufnahme entlang der Säulengrenzen. Darüber hinaus wird mit steigender Depositionsrate eine Abnahme der Kristallitgröße sowie eine Zunahme an mechanischem Stress festgestellt. Zudem zeigen tiefenaufgelöste Raman-Messungen eine Verringerung der Inkubationsschichtdicke mit steigender Depositionsleistung. Diese Arbeit zeigt, dass die aktuellen Kriterien zur Beurteilung, inwieweit mikrokristallines Silizium geeignet für den Einsatz in Dünnschicht-Solarzellen ist, erweitert werden sollten für Depositionsraten jenseits von $1\,nm/s$. Zusätzlich zu den Kriterien des optimalen Phasengemischs sollten Messgrößen berücksichtigt werden, welche die Mikrostruktur, die Tendenz zur Sauerstoffaufnahme sowie den mechanischen Stress des Materialsystems berschreiben.

Mit steigender Depositionsrate wird eine Abnahme der Leistung sowohl von mikrokristallinen Dünnschicht-Solarzellen als auch von amorph / mikrokristallinen Tandem-Solarzellen beobachtet. Die Einbußen der Leistung werden zurückgeführt auf eine mit steigender Depositionsrate verminderte Materialqualität der mikrokristallinen Absorberschicht und einer Beeinträchtigung der pi-Grenzfläche der mikrokristallinen Dünnschicht-Solarzelle. Berechnungen über die Einwirkungen eines Ionenbeschusses auf Materie lassen eine Beeinträchtigung der pi-Grenzfläche aufgrund des Ionenebeschusses als unwahrscheinlich erscheinen. Die Beeinträchtigungen der pi-Grenzfläche sind möglicherweise zurück

zu führen auf veränderte Nukleationsbedingungen oder strukturelle Inhomogenitäten an der Substrat zu Schicht Grenzfläche.

Trotz der Abnahme der Bauelementleistung mit steigender Depositionsrate zeigen Berechnungen die Möglichkeit auf, die Produktionskapazität in produzierten Watt pro Stunde um mehr als einen Faktor von 2 zu steigern. Eine Steigerung der Produktionskapazität führt zu verminderten Stückkosten je produzierter Einheit und kann sich auch in verminderten Investitionskosten widerspiegeln.

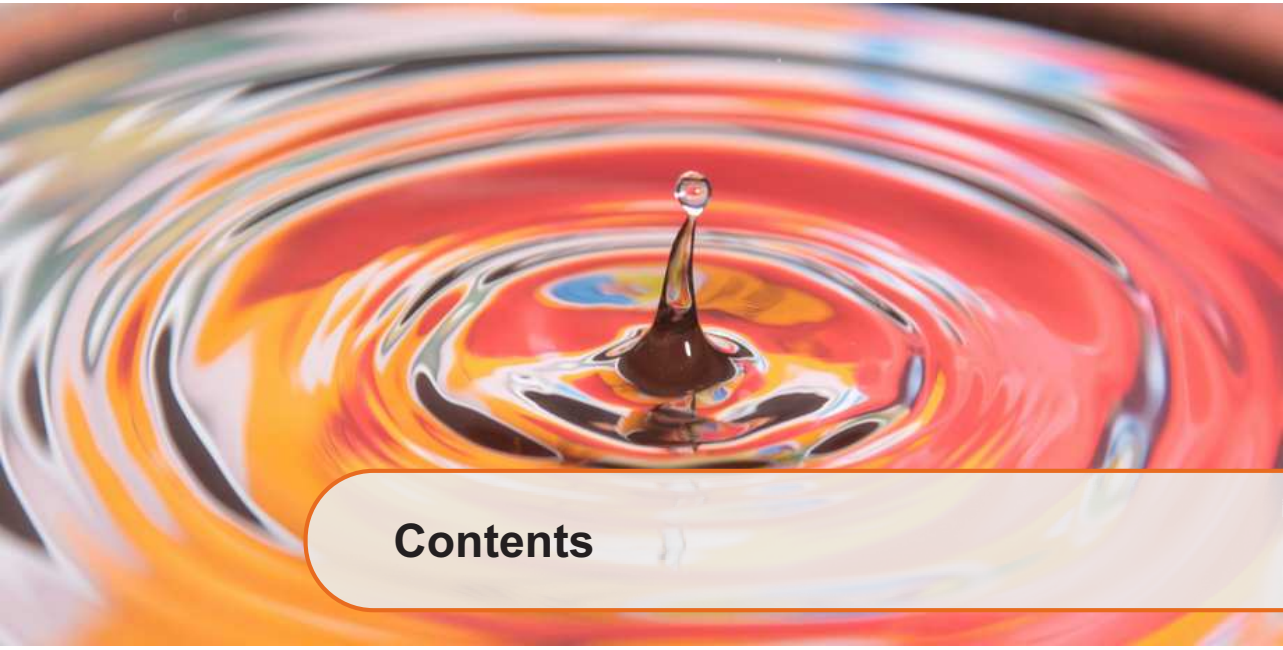

Contents

1 - Introduction

The necessity to increase the energy production through renewable processes is evident due to the finite supply of fossil fuels. Focusing on renewable energy production is one way to establish a sustainable energy production. According to the United Nations World Commission on Environment and Development report "Our Common Future" published in 1987 sustainable processes ensure to meet the worlds needs today without compromising the ability of future generations to meet their own needs [1]. The use of the sun as an energy source is predesignated for a sustainable energy production since its energy supply in one hour exceeds the yearly worlds energy needs by several orders of magnitude [2].

The first silicon based solar cell of technological importance was presented in 1954 by Chapin, Fuller, and Pearson [3]. Due to technological progress crystalline silicon single junction solar cells nowadays reach conversion efficiencies of 25% [4]. Highly efficient multi-junction solar cells reach conversion efficiencies of 44.4% under concentrated light [4].

In 1976 Carlson and Wrosnki introduced the first thin-film solar cell based on hydrogenated amorphous silicon (a-Si:H) [5]. Later hydrogenated microcrystalline silicon (μc-Si:H) was introduced as a new material for photovoltaic applications [6, 7]. Microcrystalline silicon is nowadays widely used as absorber layer of the bottom solar cell in the a-Si:H / μc-Si:H thin-film solar cell concept. This solar cell concept was pioneered by research groups in Neuchâtel, at Kaneka Corporation, and in Jülich [8, 9, 7]. The use of stacked solar cells with different optical bandgaps facilitates the efficient utilization of the solar spectrum [10, 11]. The particular advantages of thin-film solar cells compared to wafer based solar cells are: the possibility to produce solar modules on a large scale, the possibility to deposit the silicon films at low substrate temperatures,

the possibility to use cheap substrates like glass or plastic and aluminium foils, a drastic reduction in raw material consumption, and the potential for low cost production. The last point has been challenged in recent years due to massive price cuts of wafer based solar cells. These price cuts were not necessarily related to a reduction in production cost but to geopolitical decisions [12, 13]. However in a recent publication summarizing the major achievements in the field of thin-film silicon solar cells Shah et al. expect a commercial prosperity for the thin-film silicon solar technology in 2017 again [14]. Therefore research and development activities should continue on thin-film silicon solar cells and bridge the time frame until 2017. For industrial application research and development on improving the cost competitiveness is of particular interest. Nevertheless these studies are also of interest for the academic world e. g. investigations to which extend production costs can be reduced before being limited by physical properties of the applied materials.

Increasing the efficiency or reducing the manufacturing cost of thin-film solar cells are two approaches to increase the competitiveness of the thin-film silicon technology. Studies on how to reach world record solar cell efficiencies can be found in Hänni et al. [15] for μc-Si:H single junction solar cells and by Kim et al. and Guha et al. [16, 17] for multi-junction solar cells.

The motivation of the present work is to investigate the relation between growth rate, material quality, and device grade condition for intrinsic microcrystalline silicon. The investigations cover a broad range from material investigations on single layers to the application of μc-Si:H to thin-film single junction and tandem solar cells. Furthermore a calculation on the increase in system yield when implementing high growth rates for μc-Si:H is given. Specifically this work's intend is to answer the following questions:

- How to realize high deposition rates for μc-Si:H?
- Is there a link between device grade condition and deposition rate for μc-Si:H?
- How does an increase in deposition rate for μc-Si:H affect the photovoltaic-parameters of thin-film solar cells?
- Do the processes which yield high deposition rates for μc-Si:H affect interfaces when applied to thin-film solar cells?
- Are there benefits for an industrial application of processes leading to high growth rates of μc-Si:H?

Two approaches are effective to increase the deposition rate of μc-Si:H deposited by the plasma enhanced chemical vapor deposition ($PECVD$) technique. First, the application of high excitation frequencies in the VHF ($\nu_{ex} > 30\,MHz$) range [18, 19, 20] and, second, the use of the high pressure depletion regimes (HPD) [21, 22]. Curtins et al. showed an increase in deposition rate with increasing excitation frequency [18]. The

increase in excitation frequency is accompanied by a reduction of the energy of the bombarding ion due to a reduced peak-to-peak voltage [23, 24] and reduced plasma sheath width [25, 26]. The application of excitation frequencies in the VHF band was proven to be beneficial for mechanical stress [27], crystal grain size [19], charge carrier hall mobility [19], and to prevent powder production [28].
In the HPD regime deposition pressures in the range of $1\,hPa$ to $10\,hPa$ are typically applied. The increase in deposition pressure leads to an increased availability of silicon atoms in the discharge zone. The operation at depletion conditions secures the possibility for the formation of nano-crystals due to an increased hydrogen flux towards the surface of the growing film [21, 29]. An increase in particle density in the discharge leads to a reduction of the mean free path of each particle [30]. An increase in deposition pressure also induces a reduction of the plasma sheath width [25]. Both effects lead to a reduction in the energy of the bombarding ions. In the present work a combination of both processes was used for the deposition of intrinsic μc-Si:H. A detailed description on the influence of the deposition parameters on the discharge composition and the evolution of the growth rate can be found in Chapter 2.3. Apart from the $PECVD$ technique the hot wire chemical vapor deposition ($HWCVD$) technique has been used here to fabricate μc-Si:H thin films.
The present work is organized as follows:

- In Chapter 2 the fundamentals of amorphous and microcrystalline silicon as well as for thin-film single junction and multi-junction solar cells are presented. This chapter also comprises a detailed descriptions of various methods to increase the deposition rate for microcrystalline silicon.
- In Chapter 3 the experimental methods to produce and characterize silicon layers, layer stacks and solar cells are presented.
- In Chapter 4 the results of a study targeting high deposition rates for microcrystalline silicon are presented. The deposited layers were investigated with respect to their structural composition, electrical properties, and material quality.
- In Chapter 5 a study investigating the microstructure, the oxygen uptake after storage and the evolution of the Raman intensity ratio along the growth axis of microcrystalline silicon layers deposited at various growth rates is presented. Additionally, results of investigation performed by X-ray diffraction and transmission electron microscopy are presented.
- In Chapter 6 the effects of the integration of intrinsic μc-Si:H deposited at elevated deposition rates for the absorber layer of thin-film solar cells on the device performance are presented. Results obtained through monte carlo simulations on ion impact are also presented.

- In Chapter 7 the effects of an application of intrinsic microcrystalline silicon deposited at high deposition rates as absorber layer for the bottom solar cell on the device performance of a-Si:H/μc-Si:H tandem solar cells are presented.
- In Chapter 8 two methods to estimate cost benefits when implementing high deposition rates for the deposition of intrinsic microcrystalline silicon on an industrial scale are presented.
- In Chapter 9 the most important results are recapitulated and summarized.

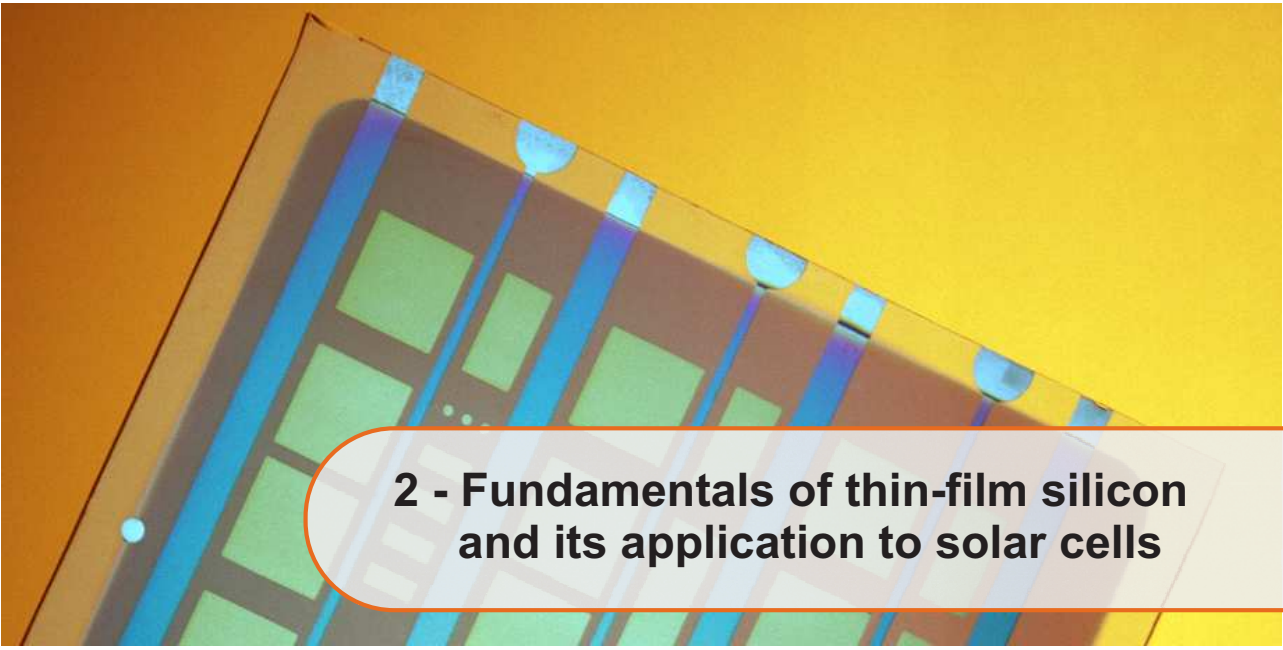

2 - Fundamentals of thin-film silicon and its application to solar cells

In this chapter the material properties of amorphous and microcrystalline silicon are introduced. Furthermore the application of these materials to thin-film single junction and multi-junction solar cells is discussed. Finally a detailed description of methods on how to increase growth rates for microcrystalline silicon is given.

2.1 Hydrogenated amorphous and microcrystalline silicon

Crystalline silicon is characterized by a well defined network of silicon atoms. The silicon atoms are covalently bonded to their neighboring atoms with constant bond length and constant bond angles. Due to the periodic structure the description of crystalline silicon can be reduced to one unit cell.

For amorphous silicon the bond length and bond angles vary by 10% [31]. Therefore the short range order of amorphous silicon is similar to crystalline silicon but a unit cell can not be defined since translation symmetry is not given. The lack of long range order combined with a similar short range of amorphous silicon with respect to crystalline silicon implicates significant consequences. First, due to the disorder the Bloch's Theorem is not a solution for the Schrödinger equation since it is restricted to a periodic potential distribution [32]. Therefore the conservation of momentum is not a precondition for optical transitions and amorphous silicon acts like a quasi direct semiconductor [33]. Second, the electronic structure of amorphous silicon is dominated by the short range order and thus similar to the one of crystalline silicon [31]. Weaire derived from the tight binding model sections where the density of states becomes zero, independent of the periodicity of the network [34]. In other words Weaire showed the presence of an energy gap in the density of states for amorphous materials.

For amorphous silicon the long range structural disorder leads to a broadened tail of states extending towards the mid gap position [33]. The density of states of the conduction band and the valence band expands via tail states towards the mid-gap position of the energy gap. The variation in bond length and bond angle is a cause for strained and broken bonds. A consequence of these strained and the so called dangling bonds are deep states within the energy gap. If not saturated with hydrogen, dangling bonds act as recombination centers for free carriers. Alloying amorphous silicon with hydrogen reduces the defect density by several orders of magnitude [33] and yields hydrogenated amorphous silicon (a-Si:H) which can be used for opto-electric applications. The structural disorder also affects the mobility of the electrons and the holes. As a consequence the extended and the localized states are separated by a mobility gap [33]. To simplify the further description the distinction between energy gap and mobility gap is not maintained.

Figure 2.1 shows the absorption coefficient for a-Si:H as a function of energy. As a reference the absorption coefficient of crystalline silicon is displayed in the same graph. Due to the direct semiconductor behavior a-Si:H shows a superior absorption coefficient for the energy range between 1.9 eV and 2.5 eV compared to crystalline silicon. For photon energies below $1.5\,eV$ the absorption coefficient is several orders of magnitude lower than for energies above $1.9\,eV$. The absorption of a-Si:H for the energy range below $1.5\,eV$ is dominated by deep defects and localized states within the bang gap.

Hydrogenated microcrystalline silicon (μc-Si:H) was first fabricated by chemical hydrogen plasma transport by Vepřek and Mareček in 1968 [35]. Its application to thin-film solar cells was pioneered by research groups in Neuchâtel, at Kaneka Corporation, and in Jülich [8, 9, 7]. Microcrystalline silicon is a phase mixture consisting of nano-crystalls, amorphous tissue, voids, and grain boundaries.

During the processing of μc-Si:H the material growth starts with an incubation layer mainly consisting of amorphous silicon or μc-Si:H with a low fraction of crystalline phase. Crystal columns start to grow in a conical form on the incubation layer orthogonal to the substrate surface [36]. While extending up to $5\,\mu m$ over the whole film thickness the diameter of the crystal columns is typically in the range from a few to several hundred of nanometers [37]. The diameter of the crystal columns is limited by the growth of crystal columns in the surrounding area of each column. Adjacent crystal columns accompany each other forming grain boundaries in between. Coalescence of neighboring crystal columns does not take place since the typical processing temperatures of approximately $200°C$ are too low. Each crystal column consists of numerous coherent domains with dimensions up to $30\,nm$. The orientation of these coherent domains is randomly distributed.

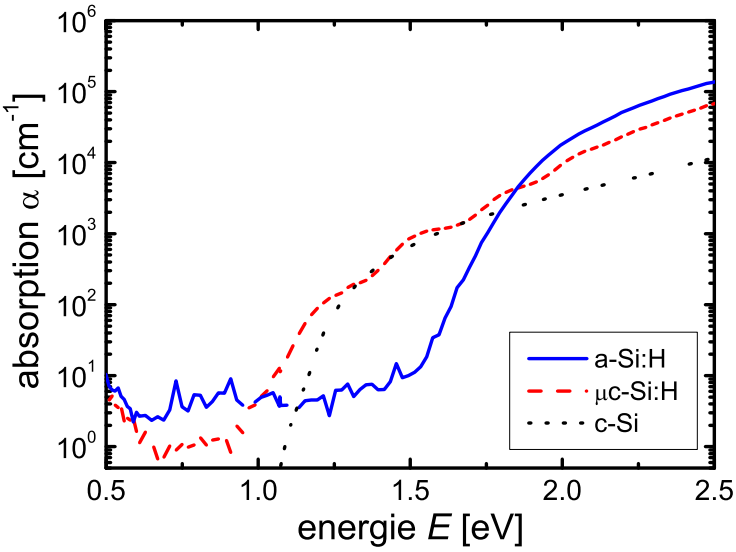

Figure 2.1: Absorption coefficient α for hydrogenated amorphous silicon (a-Si:H), hydrogenated microcrystalline silicon (μc-Si:H), and crystalline silicon (c-Si).

The ratio between the crystalline and the amorphous phase of μc-Si:H layers is characterized by the crystalline volume fraction I_C. The I_C highly depends on the processing conditions. Here the method of choice to deposit a-Si:H and μc-Si:H was the *PECVD* method (introduction given in Chapter 3.2). The main process gases used for the deposition of a-Si:H and μc-Si:H are silane and hydrogen. Details about the processing of layers and silicon thin-film solar cells can be found in Chapter 3.4. Apart from the processing parameters - excitation frequency, deposition pressure, deposition power, and electrode distance - which will be discussed in Chapter 2.3, one key deposition parameter is the silane concentration *SC*. The *SC* is defined by the ratio of the silane $Q[SiH_4]$ and the hydrogen $Q[H_2]$ mass flow into the deposition chamber:

$$SC = \frac{Q[SiH_4]}{Q[SiH_4] + Q[H_2]} \tag{2.1}$$

A variation of *SC* enables to cover the whole material range from microcrystalline to amorphous growth. For low values of silane concentration the material growths predominantly crystalline. With increasing *SC* the amorphous fraction of the material increases

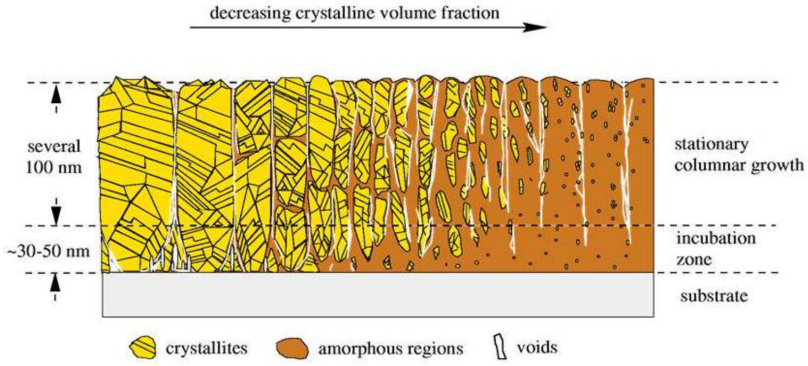

Figure 2.2: Schematic representation of the structural composition of microcrystalline silicon layers taken from [7]. A shift from highly crystalline to amorphous growth can be seen from left to right.

leading to a slight decrease of the I_C until the sharp transition from microcrystalline to amorphous growth is reached where I_C abruptly decreases. Early studies showed the phase mixture to be best for solar device performance occurs at the onset of the transition between microcrystalline and amorphous growth [7, 38]. During the further description this material will be referred to as optimal phase mixture (*OPM*) material. Previous studies show a reduced spin density for *OPM*-material compared to highly crystalline layers [39]. These results support the widely accepted assumption of a passivating effect of the crystal columns by the amorphous tissue [40]. For highly crystalline layers the passivation effect is lacking due to the low content of the amorphous phase.

Figure 2.2 shows a schematic illustration of the structural composition of μc-Si:H layers. A shift from highly crystalline to amorphous growth can be seen from left to right. This illustration is taken from Vetterl et al. [7]. It is based on material investigations by X-ray diffraction, transmission electron microscopy measurements, Raman spectroscopy, and infrared spectroscopy.

Following the description of the absorption coefficient for a-Si:H Figure 2.1 also shows the absorption coefficient for μc-Si:H considered to consist of *OPM*-material as a function of energy. As a reference the absorption coefficient for crystalline silicon is shown in the same Figure. For the energy range between $1.3\,eV$ and $1.7\,eV$ the absorption coefficient of μc-Si:H follows the absorption coefficient of crystalline silicon. In this energy range the absorption coefficient is approximately one order of magnitude higher then the one of a-Si:H. The increase of the absorption coefficient for photon energies beyond $1.7\,eV$ for μc-Si:H compared to crystalline silicon is attributed to the presence of amorphous phase in the μc-Si:H phase mixture [41, 42]. The rather low absorption coefficient for the energy range below $1.2\,eV$ is attributed to defect states within the

band gap.

The growth mechanics of μc-Si:H are still under debate. Three growth models are established in literature. They were summarized by Matsuda [22]. A common basis for all of the three growth models is a attributed key role to atomic hydrogen for the growth of μc-Si:H. The coverage of the growing surface with atomic hydrogen was shown to be mandatory for the formation of crystal nuclei [22]. Furthermore the surface reactivity increases with decreasing surface coverage due to the pronounced number of unsaturated bonds [43].

Figure 2.3 shows schematically the concepts for the three growth models starting with the preferential etching model (a), followed by the surface diffusion model (b), and finally the chemical annealing model (c). The drawings are taken from reference [22].

a) The preferential etching model describes the growth of μc-Si:H as a balance between deposition of silicon species and etching of unfavorable bonding configurations by atomic hydrogen [44, 45]. The word etching in this context is used as an umbrella term for all reactions taking place at the surface of the growing film. The model explains the formation of energetically stable bonding configurations by the preferential removal of weak silicon-silicon bonds. These weakly bonded silicon atoms are replaced by precursors forming strong silicon-silicon bonds [22].

b) The surface diffusion model describes the growth of μc-Si:H by an enhanced mobility of film precursors on the surface of the growing layer [43]. The film precursors are assumed to find and build energetically favorable bonding configurations. Thus a self organized and well ordered structure evolves. The origin of the enhanced mobility of film precursors is attributed to local heating caused by hydrogen-exchanging reactions [22].

c) The chemical annealing model was proposed to explain the formation of a continuous μc-Si:H films from the layer-by-layer deposition technique. During the layer-by-layer deposition technique the deposition of thin a-Si:H layers are alternated with hydrogen plasma treatments. The formation of a crystalline film is claimed to be caused by the penetration of hydrogen into the subsurface region. The hydrogen is assumed to cause a crystallisation of the amorphous phase by structural relaxation [46, 47].

One inevitable property of thin-film silicon is the Staebler-Wronski-Effect (SWE). The SWE describes an increase in gap states which causes a shift of the Fermi level towards the valence band. As a consequence a light induced decrease of the dark conductivity is observed [48]. According to the model proposed by Stutzmann et al. the increase in gap states is due to an increasing number of broken silicon-hydrogen bonds upon illumination [49]. The SWE leads to a reduction of the drift length of charge carriers so that current transport is increasingly affected with rising layer thickness. The SWE is a metastable effect, through heating of the material to temperatures around $160°C$ the influence of the SWE can almost be revoked. A decrease of the performance of solar cells consisting of a-Si:H is observed with increasing exposure time to light. Since the OPM-material consists of a substantial amount of amorphous phase, solar cells consisting of μc-Si:H are also affected by the SWE [50]. The SWE and the measurement setup to investigate the long-term performance of thin-film solar cells as a function of their exposure time to light is further discussed in Chapter 3.6.3.

2.2 Operating principle of silicon thin-film single junction and multi-junction solar cells

The operating principle of wafer-based solar cells can be found in numerous textbooks [51, 52]. In this section the specifics of thin-film silicon solar cells are presented. To extract an electrical current out of a solar cell the charge carriers should exhibit a driving force which pulls them away from their point of generation. This driving force can be established by an electric field or a gradient of the charge carrier density or a combination of both. One of the distinct differences between wafer-based and silicon thin-film solar cells is the origin of this driving force. In wafer-based solar cells the transport is dominated by the diffusion process of the charge carriers. For silicon thin-film solar cells the contribution of the diffusion process to the transport of charge carriers can be neglected due to the low mobility and the low lifetime of charge carriers in a-Si:H and μc-Si:H [53]. To enable charge transport in those materials it is necessary to establish an electric field which separates the charge carriers. Therefore silicon thin-film solar cells consist of two inversely doped layers which frame an intrinsic layer.

Figure 2.4 shows the schematic layer structure of a thin-film solar cell (a) and a simplified band diagram of the layer stack consisting of the two inversely doped layers and the intrinsic layer under short-circuit current conditions (b). Due to the opposed polarity of the doped layers an electric field expands over the intrinsic layer. Thus, the charge carriers which are generated in the intrinsic layer by the absorption of photons

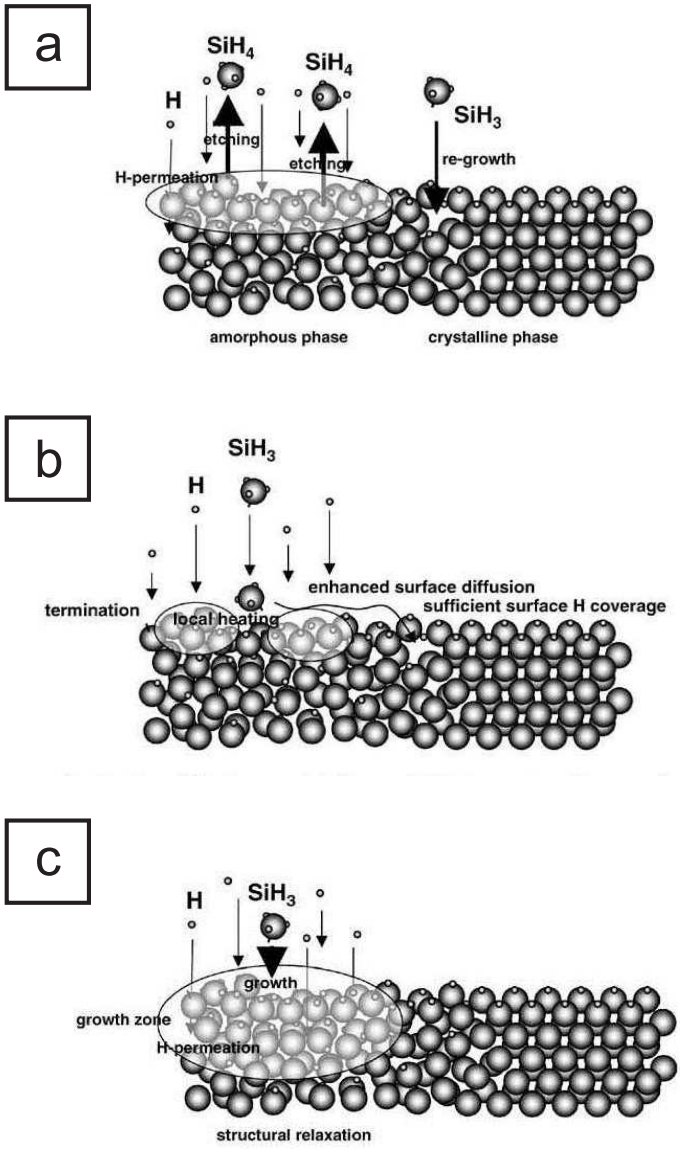

Figure 2.3: Schematic representation of growth models for microcrystalline silicon: (a) selective etching model, (b) surface diffusion model, and (c) chemical annealing model. The drawings are taken from [22].

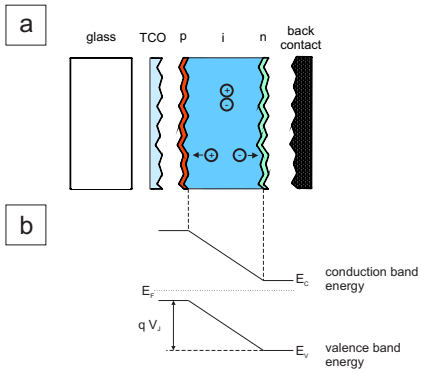

Figure 2.4: Schematic layer structure of a thin-film solar cell (a) and simplified band diagram of the layer stack consisting of the two inversely doped layers and the intrinsic layer under short-circuit current conditions (b).

are separated and can contribute to a photogenerated current. Typical thicknesses for absorber layers consisting of a-Si:H range between 200 nm and 450 nm. To ensure sufficient light absorption, layers consisting of μc-Si:H usually have thicknesses of more than 1 μm. The thicknesses for the doped layers is in the order of 20 nm to 40 nm. Doped layers are defect rich layers with low contribution to charge carrier generation [53]. To extract the charge carriers out of the solar cell the doped layers are contacted with highly conductive contacting layers. For the front contact transparent conductive oxides (TCO) are commonly applied. A layer of silver (Ag) or a layer stack consisting of Ag and TCO is usually used as a back contact. Details about the preparation of solar cells can be found in Chapter 3.4.

Photons impinging onto the surface of the solar cell are absorbed by the solar cell if their incident energy is exceeding the bandgap energy ($E > E_G$). Photons with energies below the bandgap energy are not absorbed ($E < E_G$) and transmit through the device. For an ideal solar cell without parasitic absorption the probability for a photon to be absorbed by the solar cell can be described by the following equation:

$$P\left(E = h\nu = \frac{hc}{\lambda}\right) = \begin{cases} 1 & , E > E_G \\ \\ 0 & , E < E_G \end{cases} \tag{2.2}$$

Absorbed photons generate electron/hole pairs which are separated by the electric field. Following the direction of the electric field holes are directed towards the p-type layer while electrons are directed towards the n-type layer. Electrons and holes contribute to

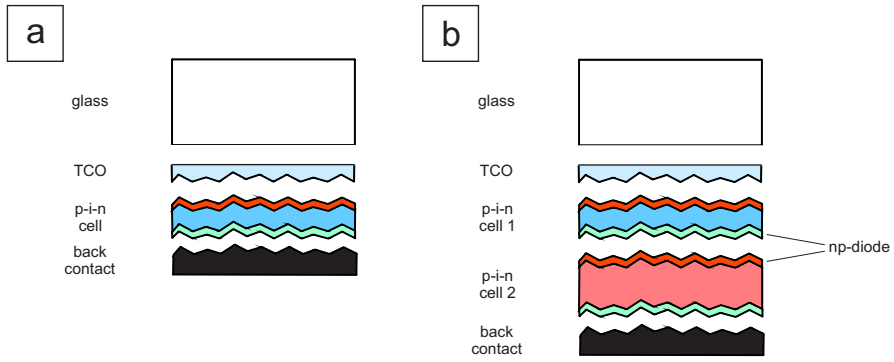

Figure 2.5: Schematics representation of the structure of silicon thin-film single junction (a) and multi-junction (b) solar cells.

a photogenerated current if they do not recombine prior to their extraction out of the solar cell. Constant charge separation builds up an electric field with opposed polarity compared to the electrical field build up by the doped layers. The potential difference generated by this electric field is called the photovoltage. By connecting the contacting layers of the device the photocurrent can be extracted out of the solar cell.

Figure 2.5 schematically illustrates the structure of silicon thin-film single junction (a) and multi-junction (b) solar cells. Due to the low mobility of holes in a-Si:H thin-film solar cells consisting of a-Si:H are illuminated through the p-type layer. According to the Lambert-Beer law the largest fraction of the charge carriers is generated close to the pi-interface. Compared to the electrons the less mobile holes have to travel the shorter distance. For μc-Si:H the mobility-lifetime product was shown to be significantly larger than for a-Si:H. Therefore for μc-Si:H single junction solar cells no preferential illumination direction exists they can either be illuminated through the p-type layer or the n-type layer [54]. When combining a-Si:H and μc-Si:H solar cells to tandem solar cells illumination through the p-type layer becomes mandatory due to the requirements for the a-Si:H top solar cell.

The use of stacked solar cells with different optical bandgaps facilitates the efficient utilization of the solar spectrum [10, 11]. On the one hand, compared to μc-Si:H single junction solar cells thermalisation losses are reduced due to the a-Si:H top solar cell which acts like a longpass filter. Furthermore, a higher open-circuit voltage is realized due to the fact that the charge carriers are extracted at higher energies. On the other hand, compared to a-Si:H single junction solar cells photons are absorbed in the μc-Si:H bottom solar cell and contribute to charge carrier generation which would otherwise

been transmitted through the solar cell (see equation 2.2). By the stacking of single junction solar cells to a multi-junction device a series connection of several devices is realized. Therefore two basic rules apply:

1. The total voltage of the device is equal to the sum of the voltages generated by each device:

$$V_{total} = V_1 + V_2 + ... + V_n \tag{2.3}$$

2. The total current generated by the device is limited by the device which generates the lowest current:

$$I_{total} = min\,(I_1, I_2, \ldots, I_n) \tag{2.4}$$

At the interface between two stacked solar cells a np-diode is formed originated from the n-type layer of the top solar cell and the p-type layer of the bottom solar cell (see Figure 2.5). Upon illumination this diode is operated in reverse direction. Electrons generated in the top solar cell and holes generated in the bottom solar cell are driven towards the np diode. By the use of strong doping this diode can act as a tunnel junction. Consequently electrons and holes recombine through this junction and maintain the current transport throughout the whole stacked device.

2.3 High growth rates for microcrystalline silicon

The layers and layer stacks investigated in this thesis were fabricated in a vacuum deposition system. The *PECVD* reactors are of parallel plate design (details can be found in Chapter 3.1). The *PECVD* method as a processing technique is presented in more detail in Chapter 3.2. In this chapter measures to increase the growth rate of μc-Si:H are introduced. This includes a description of the effects of key deposition parameters - excitation frequency ν_{ex}, deposition pressure p, deposition power P, and electrode distance d - on discharge variables. For simplicity in this chapter the term "plasma" and "glow discharge" are used as synonyms. A more precise definition of both terms is given in Chapter 3.2.

In a simplistic approach a glow discharge can be divided into three regions. The plasma bulk which is surrounded by two plasma sheaths. The growth precursors are generated in the plasma bulk and reach the surface of the growing film via drift and diffusion processes. A variation in deposition parameters which leads to a change in the properties of the plasma bulk affect the generation rate of the growth precursors [55]. Changes of the plasma sheath properties affect the energy of the bombarding ions and the flux

towards the growing film [55]. However, most variations of deposition parameters induce variations of the properties of the plasma bulk as well as the plasma sheaths.
The two methods to increase the growth rate of a silicon thin film processed by $PECVD$ are: first an increase of the generation rate of the growth precursors in the plasma bulk or/and second the increase of the flux of the growth precursors towards the growing film. For the processing of μc-Si:H a good surface coverage of the growth zone with atomic hydrogen must be assured [43, 56]. Furthermore the energy of the bombarding ions should be kept within reasonable limits since strong ion bombardment can induce lattice distortions and can lead to a reduced grain size of the crystall grains [43]. In case of a very high energy of the bombarding ions the growth of μc-Si:H can even be suppressed [29].
The most straightforward approach to increase the deposition rate of μc-Si:H is to increase the dissociation of the process gases through an increase of the deposition power. A secondary effect of an increase in deposition power is an increase of the energy of the bombarding ions which can in extreme cases damage the surface of the growing film. Measures to counteract the high energetic ion bombardment are an increase of the excitation frequency or an increase in deposition pressure. Both lead to a reduction of the plasma potential and hence to a reduction of the energy of the bombarding ions. Details about the implications of a variation of the key deposition parameters on the process conditions for thin silicon films are given in the following, starting with a description of the excitation frequency.

The role of the excitation frequency

In the early days of microelectronic industry the most widespread excitation frequency of plasmas was 13.56 MHz. In the MHz frequency range, the excitation frequency exceeds the ion plasma frequency. Under these conditions the ions do not follow the polarity of the electric field and can be considered as stationary. The use of this specific frequency was justified by legal and not physical reasons since this frequency was licensed by the United States Federal Communications Commission for industrial applications. The application of excitation frequencies beyond 13.56 MHz became popular for plasma etching applications in the mid 1980's [57, 58]. The first to apply elevated excitation frequencies to the processing of thin silicon films were Curtins et al. in 1987 [18, 59]. They showed an increase in the deposition rate with increasing excitation frequency until an optimal frequency is reached. Beyond this point of optimal frequency the deposition rate decreases again with increasing frequency. Although the exact shape of the characteristic deposition rate over excitation frequency is highly depending on the deposition system the general trend of an increased deposition rate with higher excitation is independent of the processing equipment [60]. The decrease in deposition rate beyond the point of

optimal frequency is attributed to a less efficient power in-coupling due to frequency dependent electrical losses (e.g. stray capacitances) [60]. The increase in growth rate with increasing excitation frequency is not clarified conclusively in literature. Some early theoretical studies attribute the increase in growth rate to changes of the electron energy distribution function ($EEDF$) [61, 62]. With increasing excitation frequency the shape of the $EEDF$ approximates a Maxwellian distribution [62], which causes the electron density to increase in the plasma bulk [62] and the average electron energy to decrease [61]. Oda et al. showed slight changes in the $EEDF$ of plasmas operated at 13.56 MHz and 144 MHz derived from plasma diagnostic measurements with optical emission spectroscopy and Langmuir probe [63]. Since, the growth precursors are generated by electron impact ionization an increased density of electrons in the plasma bulk leads to an enhanced dissociation of process gases. On the contrary Heintze et al. claim that the enhancement in gas dissociation is not significant enough to be accounted for an increase in growth rate for the frequency range between 13.56 MHz and 200 MHz. They showed an increase in ion flux towards the growing film accompanied by a decrease in ion energies and account these effects to be responsible for the increase in growth rate [64, 65]. Both models postulate a decreasing average energy per discharge particle with increasing frequency. This leads to a decrease in plasma potential V_p. The peak-to-peak voltage was shown to decrease with increasing excitation frequency [23, 24]. Köhler et al. derived a linear expression between the maximum energy of the bombarding ions E_{max},

$$E_{max} = \frac{e\,V_{pp}}{4} \tag{2.5}$$

and the peak-to-peak voltage V_{pp}, with e describing the elementary charge [66]. Thus, the maximum energy of the bombarding ions decreases with decreasing peak-to-peak voltage. Furthermore, the thickness of the plasma sheath decrease with increasing excitation frequency. In a very simplistic approach a glow discharge can be described by a bulk plasma and two sheaths regions. The complex impedance Z of this simplified model can be described by,

$$Z = R + j\,\frac{1}{\omega\,C_{tot}} = R + j\,\frac{1}{2\,\pi\,\nu_{ex}\,C_{tot}} \tag{2.6}$$

a series connection of the resistive bulk part R and the sum of the two capacitive plasma sheaths C_{tot}, with j describing the imaginary unit, and ν_{ex} describing the excitation frequency. With increasing excitation frequency the contribution of the imaginary part of equation 2.6 decreases. The decrease in sheath impedance results in an increase in ion fluxes and ion density. As a consequence the plasma potential is diminished

which induces a reduction in sheath thickness. This effect was proven experimentally by Beneking et al. [25] and supported by Schwarzenbach et al. [26]. Both effects, the reduced peak-to-peak voltage and the reduced plasma sheath thickness, result in a decrease of the energy of the bombarding ions with increasing excitation frequency.
The application of elevated excitation frequencies for the processing of thin silicon films showed promising results. Dutta et al. showed a decrease in intrinsic compressive stress for a-Si:H films from approximately $2 \times 10^8\, N/m^2$ to $1 \times 10^7\, N/m^2$ when increasing the excitation frequency from 13.56 MHz to 70 MHz [27]. Finger et al. showed for μc-Si:H a parallel increase in grain size, hall mobility, and deposition rate with increasing excitation frequency [19]. Evidence for less powder production at elevated excitation frequencies were given by Dorier et al. [28]. The topic of powder production in the environment of processes leading to high growth rates of μc-Si:H will be discussed at the end of this chapter. For industrial application of excitation frequencies in the VHF band special care should be taken when designing the electrode configuration and the power in-coupling to the discharge chamber. With increasing excitation frequency the wavelength of the plasma excitation can reach dimensions close to the reactor geometry which can cause nonuniform voltage distributions over the electrodes induced by standing wave effects [67]. To circumvent frequency related distortions of the electric field the application of multi-pole power feeding [68], the use of lens shaped electrodes [67], or the use of linear plasma sources [69] have been suggested.

The role of the discharge pressure

A second approach to increase the density of growth precursors in the discharge is the increase of the discharge pressure. An increase in the discharge pressure results in an increased particle density and an enhanced gas residence time in the discharge. To ensure first an adequate flux of atomic hydrogen towards the surface of the growing film and second a sufficient surface coverage by atomic hydrogen the discharge has to be operated at silane depletion conditions [29]. This processing regime was first introduced by Guo et al. in 1998 and is known in literature as high pressure depletion (HPD) regime [21]. At elevated discharge pressures the crystallinity of thin silicon films is reduced due to a decreased flux of atomic hydrogen towards the surface of the growing film. This reduction in flux of atomic hydrogen is caused by the annihilation reaction,

$$H + SiH_4 \rightarrow H_2 + SiH_3 \tag{2.7}$$

which describes the formation of molecular hydrogen H_2 and SiH_3 molecules by the annihilation of one hydrogen atom of a silane molecule SiH_4 by one atom of hydrogen

H [29]. In silane depletion conditions the annihilation reaction is suppressed and a sufficient flux of atomic hydrogen towards the surface of the growing film is assured. [21, 29]. At constant gas flow rates the depletion of silane in the discharge can be reached by increasing the discharge power [21].
With increasing pressure the density of particles in the discharge increases. As a consequence the mean free path of each particle decreases which leads to a reduction of the plasma potential [30]. Furthermore the plasma sheath thickness decreases with increasing pressure [25]. Both effects result in a reduced energy of the bombarding ions [21].
The combination of the high frequency approach together with the *HPD* regime with respect to the application to the processing of silicon layers, layer stacks, and silicon thin-film solar cells has been investigated by numerous research groups. For example:

- at the University of Utrecht [70, 71],
- at the University of Neuchâtel [72, 73],
- at the National Institute of Advanced Industrial Science and Technology of Japan [74, 75],
- and at the research center in Jülich [76, 77, 78, 79].

The role of the discharge power

Due to the presence of undecomposed silane particles, for low pressure discharges an increase in deposition power leads to an enhanced gas dissociation of process gases and consequently, since the density of growth precursors is increased, to an increase in the growth rate [23, 79]. At silane depletion conditions an increase in the discharge power does not lead to an increase in the deposition rate [78]. In fact a higher discharge power leads to a pronounced dissociation of molecular hydrogen leading to an increased density of atomic hydrogen in the discharge [21]. This changes the silane to hydrogen radical density in the discharge which determines the micro structure of the growing film [80]. In any case an increase in the discharge power leads to an increase in the plasma potential which in turn is responsible for an increase in the energy of the bombarding ions [23]. However, at elevated excitation frequencies and high discharge pressures an increase in the deposition power is possible within certain limits.

The role of the electrode distance

Studies showed a decrease in deposition rate with decreasing electrode distance [78, 79]. This effect is attributed to a decrease in discharge volume with decreasing electrode distance. According to Paschen's law the electrode distance can serve as a balancing parameter to maintain stable discharge conditions at elevated discharge pressures [81]. Although small deviations in electrode distance can lead to large variations in film

thickness. The homogeneity in film thickness was shown to improve at reduces electrode distances [82]. Another side effect of a reduced electrode distance is the less pronounced powder production [73, 83]. This effect is attributed to silane precursor reactions which are more likely to occur at large discharge volumes than at smaller ones. Avoiding excessive powder production during the processing of thin silicon films is a critical issue especially for industrial applications since it determines cleaning cycles and the yield of the processing equipment. The application of high excitation frequencies showed beneficial effects with respect to unwanted powder production. Studies showed a decrease in powder production with increasing excitation frequency [28, 84].

After a theoretical description of the implications of a variation of the key deposition parameters on the processing conditions of thin silicon films the results of a process and material development study are presented in Chapter 4. For this parameter study the HPD regime was applied for the deposition of the thin silicon films altogether with an excitation frequency in the VHF band. A variation of the silane concentration, the electrode distance, the deposition pressure, and the deposition power was investigated with respect to the growth rate, the structural composition, the electrical properties, and the material quality of the deposited layers.

3 - Experimental Methods

In this chapter the experimental techniques used to fabricate and characterize silicon layers, layer stacks and solar cells are described. First, the deposition system used to fabricate the samples is described. Second, the plasma enhanced chemical vapor deposition ($PECVD$) and the hot wire chemical vapor deposition ($HWCVD$) techniques are introduced. Then the characterization methods to investigate layer properties is presented. Finally, a description of the characterization techniques used to investigate the properties of thin-film silicon solar cells is given.

3.1 The deposition system

The silicon layers, layer stacks, and solar cells presented here were produced using a multichamber deposition system in clustertool configuration. Figure 3.1 shows the system with images of typical deposition processes next to the according chamber. A detailed description of the commissioning and maintenance procedures of the deposition system as well as a description of the development of its baseline processes can be found in [85].

The system consists of five process chambers ($PC1$ - $PC5$), two load locks ($MC1$, $MC2$), and one heating station (HS) which are connected to the transfer chamber (TC). Substrates with dimensions of $10x10cm^2$ can be loaded to the system via the load locks $MC1$ and $MC2$. The substrates are handled between the different chambers by a robot arm which is located in the transfer chamber. The heating station HS is used to pre-heat the substrates prior to the deposition.

Processing chambers $PC1$ to $PC3$ are equally designed $PECVD$-chambers. $PC1$ is used for the deposition of p-type material, $PC2$ for intrinsic, and $PC3$ for n-type material. In

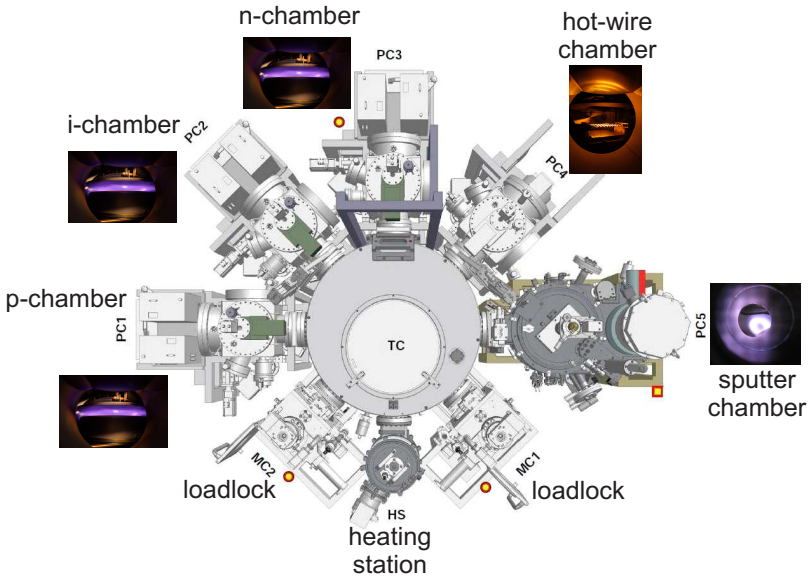

Figure 3.1: Technical drawing of the clustertool deposition system. The function of each chamber is labeled close to the appropriate chamber. For the processing chambers an image of the characteristic process for each chamber is displayed.

processing chamber $PC4$ silicon layers can be fabricated by $HWCVD$. Processing chamber $PC5$ is used for the fabrication of front- and back contact electrodes for thin-film solar cells by the sputtering technique.

Figure 3.2 schematically shows the configuration of the $PECVD$ chambers ($PC1$ to $PC3$) including the design of the pumping system.

Each processing chamber is equipped with a multistage pumping system consisting of a turbo pump, a roots pump, and a rotary vane pump. With this configuration it is possible to reach pressure values in the range of $10^{-8}\,hPa$,preventing the different processing steps from cross contamination. The bypass line circumventing the turbo pump shown in Figure 3.2 is used during the layer deposition to protect the turbo pump from the processing gases. With the use of the butterfly valve deposition pressures in the range of $0.1\,hPa$ to $10\,hPa$ can be adjusted.

The $PECVD$ reactors are of parallel plate design with capacitively coupled generators. The power supply to the fixed, circular electrode (diameter $d_p = 164\,mm$) is realized by a copper ribbon by the use of a feed through. These measures - copper ribbon, and fixed electrode - where taken into account to prevent extensive, parasitic electrical losses.

Figure 3.3 shows the configuration of the $PECVD$ chambers ($PC1$ to $PC3$) (a) compared to the configuration of the $HWCVD$ chamber ($PC4$) (b).

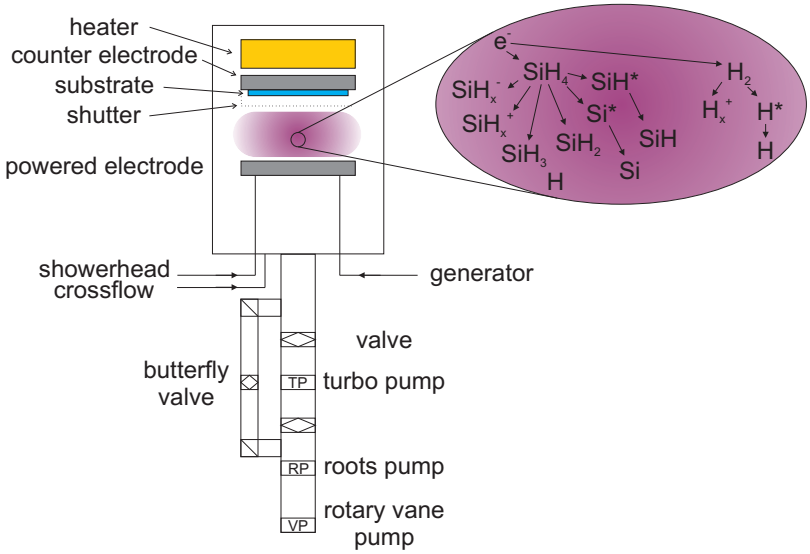

Figure 3.2: Configuration of the *PECVD* chambers including the pumping system.

The substrate is placed on the grounded electrode. A variation of the electrode distance between 5 *mm* and 25 *mm* is possible by varying the substrate electrode towards the powered electrode. The substrate heater is in direct contact with the substrate. The temperature values indicated in the present work refer to the heater values set by the operator. Details about the heating setup and the heat distribution in the reactor can be found in [86].

The gas supply for the reactor can be changed between crossflow (*CF*) and showerhead (*SH*) mode. If not stated otherwise the material presented here was processed using the *SH*-mode. More insights on the influence of the gas flow geometry and its effect on the performance of μc-Si:H solar cells can be found in [87].

Each *PECVD* chamber is equipped with two generators operating at 13.56 MHz and 81.36 MHz, respectively. To ensure an optimal adjustment of the discharge impedance each chamber is equipped with two matchboxes optimized for the according frequency range.

The *HWCVD* deposition chamber is designed similarly to the *PECVD* chambers. The geometrical dimensions are equal as well as the substrate-heater configuration. At the place of the powered electrode the wire holder is mounted. Three coiled tantalum wires with a diameter of 0.5 *mm* and a length of 150 *mm* are clamped between electrical joints. The gas supply is realized by three stainless steel tubes which are fixed at a distance of 20 *mm* below each wire. The horizontal distance between the wires is 40 *mm*. Each tube

has 13 holes at a constant distance to assure a homogeneous gas distribution along the wires. The temperature of the filaments is monitored with an impac ISQ 5 pyrometer measuring infrared radiation at 1.05 μm.

3.2 Plasma-enhanced chemical vapor deposition technique

This section gives a brief introduction on the *PECVD* method as one of the techniques used to process silicon layers, layer stacks, and solar cells. Comprehensive introductions to material processing by glow discharge processes can be found in literature [88, 89]. The term "plasma" refers to ionized gases, often called the fourth state of matter. A plasma consists of positively and negatively charged particles and neutral molecules. The degree of ionization can vary over several orders of magnitude from glow discharges (10^{-4}), over lightning strikes (10^{21}), to the solar core (10^{33}). The degree of typical glow discharges for the processing of silicon films is approximately 10^{-4} [88]. Thus a glow discharge can be described as a type of plasma with a low degree of ionization which mostly consists of neutral species.

When applying the *PECVD* method the discharge is driven by a frequency modulated electrical field where the gas dissociation takes place through electron impact ionization. The deposition by *PECVD* allows the use of substrate temperatures down to room temperature since the energy for the process gas dissociation and the crystall formation is provided by the electric field and not thermally. Hydrogen-silane glow discharges consist apart from the neutral species of silane radicals which act as growth precursors for the silicon layer. These growth precursors reach the surface of the growing film via drift- and diffusion processes. It is still under debate which silane radicals play the dominant role for the growth of a-Si:H and μc-Si:H growth. Some studies claim the SiH_3 radical to be the only one to be responsible for the formation of thin silicon films through the gas phase [90, 56]. Others question the evidence for the dominant role of the SiH_3 radical [91, 92] and object to restrict the discharge chemistry to a limited set of reactions [93].

Once the growth precursors reach the surface of the growing film various interaction can take place. Growth precursors can be reflected to the gas phase either directly or by the abstraction of hydrogen which covers the growing film. The growth precursors can also be adsorbed by the surface and start diffusing on the surface until an energetically favorable site is found where they form silicon-silicon bonds with surface silicon [56]. The established growth models for the formation of μc-Si:H are presented in Chapter 2.1.

Due to their low mass compared to ions electrons follow the polarity of the electric field. As a consequence the powered electrode gets charged negatively. Leaving behind the

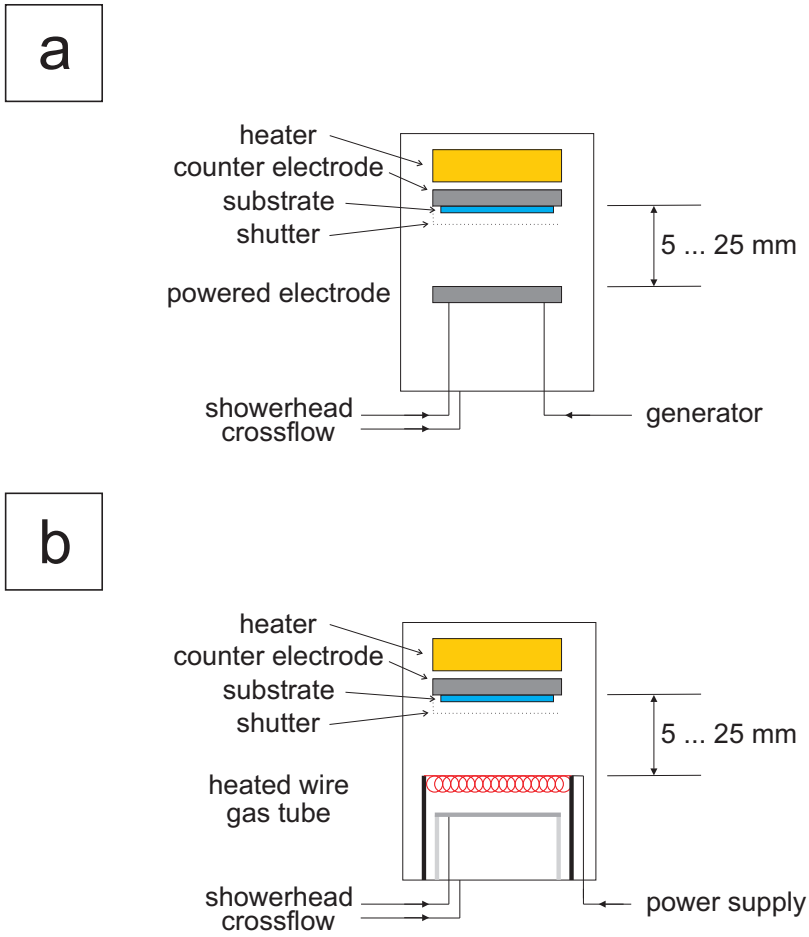

Figure 3.3: Configuration of the *PECVD* chambers (a) and configuration of the *HWCVD* chamber.

main discharge slightly positively charged. The grounded substrate electrode serves as a reference potential. The negative potential at the powered electrode is called the self bias voltage. The potential drop between the electrodes and the main discharge leads to ion bombardment of the growing film.

3.3 Hot wire deposition technique

The *HWCVD* deposition technique is investigated for the application to the fabrication of thin-film solar cells due to the absence of damage induced by ion bombardment (see Chapters 2.3 and 3.2). Similar as the *PECVD* technique the *HWCVD* technique allows the deposition of thin silicon films at low substrate temperatures since the energy for the process gas dissociation is provided by heated metal wires. The *HWCVD* method is also known in literature as $cat-CVD$ method because the processing gases are decomposed by a catalytic reaction at a heated metal wire. After a first exploration in the 1970's [94] the method was re-discovered by Matsumura et al. for the processing of a-Si:H films [95]. Later the same group showed the feasibility to deposit polycrystalline silicon also by *HWCVD* [96]. Rath et al. [97] and Klein et al. [98] investigated the application of intrinsic protocrystalline and microcrystalline silicon absorber layers deposited by *HWCVD* to thin-film solar cells. Mai et al. included intrinsic silicon buffer layers processed by *HWCVD* into thin-film solar cells and showed beneficial effects on the performance of μc-Si:H single junction solar cells [99]. Recently *HWCVD* was investigated for the processing of n-type and p-type silicon carbon alloys for the application as window layers in thin-film solar cells [100, 101].
The deposition of thin silicon films by *HWCVD* can be divided into three separate steps:

1. The dissociation of process gases at a heated metal wire. A variation of the wire temperature enables to govern the ratio of generated silane radicals between SiH, SiH_2, and SiH_3 [102].
2. Transport to the substrate and gas phase reactions. Depending on the mean free path the silane radicals encounter gas phase reactions before overcoming the wire to substrate distance. The mean free path can be reduced by increasing the deposition pressure. Gas phase reactions lead to further formation of SiH_2 and SiH_3 radicals [103]. At low deposition pressure the absence of gas phase reactions lead to the deposition of silicon films with poor material quality [94, 102].
3. Growth of the silicon film. The flux of the growth precursors towards the surface of the growing film can be governed by adjusting the deposition pressure. Once the growth precursor reach the substrate similar growth mechanisms take place as for layers processed by *PECVD* [104, 102].

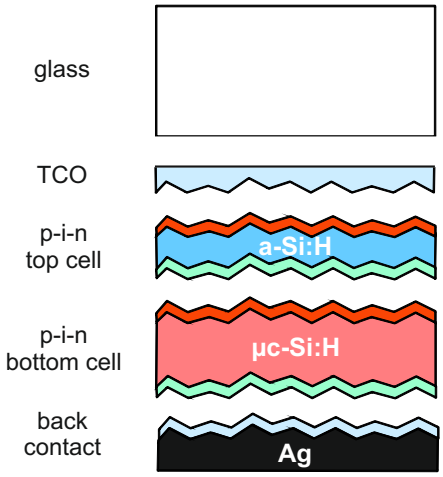

Figure 3.4: Schematic of a silicon thin-film tandem solar cell in superstrate configuration and p-i-n/p-i-n deposition sequence.

In the present work the *HWCVD* technique was used to deposit buffer layers for the application to single junction μc-Si:H solar cells, as discussed in Chapter 6. A detailed introduction to the *HWCVD* technique can be found in the work of Klein [105].

3.4 Material and solar cell preparation

Figure 3.4 shows a schematic illustration of the composition of an a-Si:H/μc-Si:H tandem solar cell. Solar cells were fabricated in superstrate configuration with p-i-n deposition sequence in case of single junction solar cells and p-i-n-p-i-n deposition sequence in case of a-Si:H/μc-Si:H tandem solar cells. For single junction solar cells an in-house developed aluminum doped zinkoxid ($ZnO:Al$) was used as front contact. The surface of the magnetron sputtered $ZnO:Al$ was randomly textured by a wet chemical etching step (40 second in 0.5 % diluted hydrochloric acid) to increase the light-trapping properties in the solar cells [106]. After the etching step the thickness of the $ZnO:Al$ was reduced to roughly 600 nm from originally 800 nm. For tandem solar cells a commercially available Asahi VU-type glass coated with tin dioxide (SnO_2) was used for the front contact electrode.

To avoid cross contamination p-, i-, and n-layers were deposited in different process chambers (see Chapter 3.1). As doping gases trimethylboron (TMB - 2% TMB diluted in Helium) and phosphine (PH_3 - 5% PH_3 diluted in silane) were used for p-type and n-type doping, respectively.

To remove moisture from the substrate surface a heating procedure of 1 hour was applied

as pre-processing step. Table 3.1 summarizes the layer sequence for μc-Si:H single junction and a-Si:H/μc-Si:H tandem solar cells. Furthermore the excitation frequency for each layer is given.

The application of an amorphous n-layer in the bottom solar cell prevents from current collection. Current collection from an enlarged area may falsify the sun simulator measurements (see Chapter 3.6.1) were a defined area is assumed. An alternative approach to avoid current collection is to apply a laser patterning step which yields well defined solar cell areas. The solar cell preparation is terminated by the application of the back contact. In case of μc-Si:H single junction solar cells this back electrode consists of thermally evaporated silver (Ag). A layer stack consisting of $ZnO:Al/Ag/ZnO:Al$ served as back contact in case of tandem solar cells. Compared to a pure Ag back contact such a back contact yields an increased reflectivity and thus enhances the light absorption in the absorbing layers.

For thickness, Raman, and conductivity measurements the silicon layers were deposited on 1 mm thick Corning Eagle 2000 glass. Double sided polished Czochralski (CZ) grown wafers served as substrates for infrared measurements.

	μc-Si:H	a-Si:H/μc-Si:H
	$[MHz]$	$[MHz]$
a-Si:H <p>		13.56
a-Si:H <i>		13.56
μc-Si:H <n>		81.36
μc-Si:H <p>	81.36	81.36
μc-Si:H <i>	81.36	81.36
a-Si:H <n>	13.56	13.56

Table 3.1: Layer sequence and excitation frequency for each layer for μc-Si:H single junction and a-Si:H/μc-Si:H tandem solar cells.

3.5 Material characterization

3.5.1 Electrical conductivity

To measure the electrical conductivity σ of the fabricated material the films were deposited on glass substrates. Two thermally evaporated silver pads in co-planar configuration served as electrodes. The silver contacts with a width l of 5 mm at a distance s of 0.5 mm were used. With the known film thickness d_{th} the conductivity can be calculated

by measuring the current I at a variable voltage V ($\pm 100\,V$) by the following equation:

$$R = \frac{1}{\sigma}\frac{s}{d_{th}\,l}$$
$$\Rightarrow \sigma = \frac{I}{V}\frac{s}{d_{th}\,l} \tag{3.1}$$

To avoid influences of surface coverage by water vapor the measurement was performed under vacuum ($\approx 10^{-5}\,mbar$) after an annealing step. The conductivity was measured at room temperature after annealing the samples for $30\,min$ at $440\,K$. The photo conductivity σ_{ph} was measured by illuminating the sample with a halogen lamp. The intensity of the light source was calibrated with a photo diode against $AM\,1.5$ standard illumination. The photosensitivity as a measure of material quality was calculated by the ratio of photo conductivity σ_{ph} to dark conductivity σ_d.

3.5.2 Thickness measurements

Thickness measurements of deposited layers were performed with a mechanical step profiler Veeco Dektak 6M. The deposition rate R_D was estimated by dividing the layer thickness by the according deposition time. The deposited films were removed from the glass substrate either by laser ablation or by an adhesive tape. These methods yield well defined steps.

3.5.3 Raman spectroscopy

The Raman effect was discovered in 1928 by the Indian physicist C. V. Raman [107, 108]. With Raman spectroscopy vibrational properties of liquids, gases, and solids can be investigated. A detailed discussion of light scattering properties in solids can be found in literature [109, 110]. The feasible application of Raman spectroscopy for the investigation of μc-Si:H was shown by Richter [111].
Raman spectroscopy enables the possibility to calculate the Raman intensity ratio I_c^{RS}, which is a semi-quantitative measure for the crystalline volume fraction of μc-Si:H. The material is probed with a focused laser beam. The incident photons with an energy $\hbar\,\omega_i$ are scattered inelastically by emitting ($+\hbar\,\omega_k$, Stokes process) or annihilating ($-\hbar\,\omega_k$, anti-Stokes process) phonons. The energy of the scattered phonons $\hbar\,\omega_s$ is given by the following equation, where $\hbar$ describes the reduced Planck constant and ω the angular

frequencies of photons and phonons:

$$\hbar\,\omega_s = \begin{cases} \hbar\,\omega_i + \hbar\,\omega_k & \text{, Stokes process} \\ \\ \hbar\,\omega_i - \hbar\,\omega_k & \text{, anti-Stokes process} \end{cases} \tag{3.2}$$

Depending on the material under investigation the frequency shift occurs at different wavenumbers. Figure 3.5 shows a typical Raman spectrum for a μc-Si:H layer deposited on glass. The peak at $520\,cm^{-1}$ is attributed to the crystalline phase of the mixed phase material. It corresponds to the transverse optical (TO) phonon mode in c-Si. For a-Si:H the TO phonon mode broadens due to the lack of long range order giving rise to a broad contribution to the Raman spectrum at $480\,cm^{-1}$. A third contribution to the Raman spectrum at $500\,cm^{-1}$ is attributed to stacking faults along the growth direction [112]. The I_c^{RS} is calculated by the method described in reference [113], this method is visualized in Figure 3.5. A scaled amorphous reference spectrum (blue curve in Figure 3.5) is subtracted from the measured microcrystalline spectrum (open circles in Figure 3.5). The I_c^{RS} is calculated by the ratio of the integrated intensities attributed to c-Si I_{cc} and the sum of the integrated intensities attributed to c-Si I_{cc} and the a-Si:H phase I_a:

$$I_c^{RS} = \frac{I_{cc}}{I_a + I_{cc}} \tag{3.3}$$

The information depth of the Raman spectroscopy is given by the Lambert-Beer law and depends on the absorption coefficient of the investigated material, which in turn depends on the wavelength of the exciting laser. Therefore, it is possible to collect information of the I_c^{RS} for different depth of the investigated material when using lasers of different wavelengths. This is one method to get a rough idea about the evolution of the I_c^{RS} along the growth direction. An alternative and more precise approach to investigate the I_c^{RS} along the growth direction is to perform thickness depending Raman measurements. Therefore, thickness and Raman measurements are performed along the same scan-line over an etching crater. Two setups were available to perform Raman spectroscopy measurements. The first one is a commercial available Raman Renishaw inVia microscope using an argon laser with a wavelength of $532\,nm$. This setup was used as the standard setup to investigate the I_c^{RS} from the film and from the glass side of the samples. For more elaborate investigations, like the described thickness depending measurements, a second Raman setup was used which is described in detail in [114]. This setup is equipped with an argon and a krypton laser with excitation wavelengths of $488\,nm$ and $647\,nm$, respectively. The argon laser was used for the thickness depending Raman measurements.

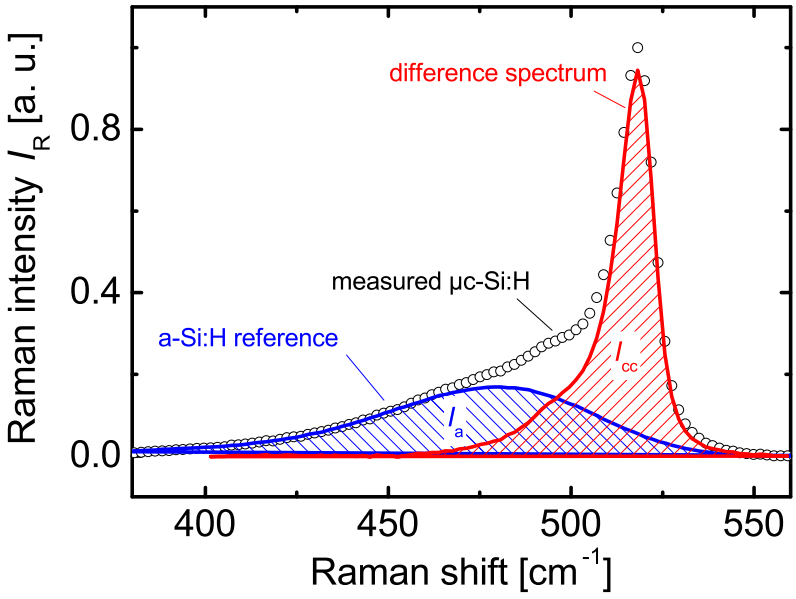

Figure 3.5: Typical Raman spectrum of a μc-Si:H layer deposited on glass. Furthermore the evaluation technique to calculate the Raman intensity ratio out of the Raman spectrum is visualized. From the measured spectrum a calibrated and scaled amorphous reference is subtracted. The Raman intensity ratio is calculated by equation 3.3.

3.5.4 Infrared spectroscopy

Infrared spectroscopy (*IR*) is a widely used method to investigate the hydrogen content (C_H), the oxygen content (C_O), and the bonding configuration of thin films for a variety of material types. Key advantages of *IR* spectroscopy are its non-destructive nature and fast probing times per sample ($< 30\,s$). The material under investigation was deposited on double side polished *CZ*-wafer pieces of quadratic shape with an edge length of $15\,mm$. For each sample series the wafer pieces where taken from the same cleaved wafer where one piece was retained as reference sample. The spectra where collected with a Nicolet 5700 Fourier Transform-*IR* spectrometer in the range from $400\,cm^{-1}$ to $4000\,cm^{-1}$. For each sample the spectra where averaged over 32 scans to assure reliable statistics.

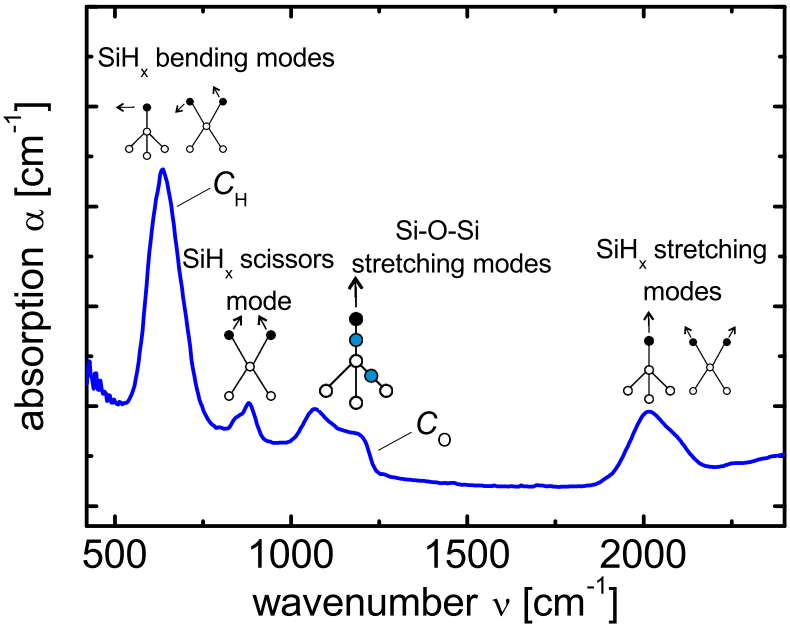

Figure 3.6: Infrared absorption spectra for μc-Si:H layer deposited on double sided polished Choralski grown wafer pieces. The mode descriptions are labeled close to the appropriate absorption bands.

Figure 3.6 shows a *IR* typical spectrum for μc-Si:H. The sample shows a strong presence of oxygen as can be seen by the evolution of an absorption band between 980 cm^{-1} and 1200 cm^{-1} which is characteristic for $Si-O-Si$ stretching and bending modes. In addition the sample shows a strong absorption band around 640 cm^{-1} which is attributed to the $Si-H_{1,2}$ wagging, rocking and bending modes. The absorption band around 890 cm^{-1} is attributed to the $Si-H_2$ scissors mode. The absorption bands around 2000 cm^{-1} and 2100 cm^{-1} are attributed to the $Si-H$ and $Si-H_2$ stretching modes [115, 116]. Table 3.2 summarizes the occurring absorption bands with their associated mode descriptions.

The hydrogen content of the deposited layers was evaluated with the method proposed by Beyer and Abo Ghazala [117]. The hydrogen content is a crucial parameter when investigating silicon thin-films composed of mixed phase material since the electronic, optical, and microstructural properties change with varying hydrogen content [118]. In this work the amount of bonded hydrogen atoms was calculated by the integrated in-

peak position cm^{-1}	mode description
620 - 640	$Si-H$, $Si-H_2$ wagging, rocking, bending modes
890 - 900	$Si-H_2$ scissors mode
980 - 1200	$Si-O-Si$ stretching and bending modes
2000	$Si-H$ stretching modes in compact material
2100	$Si-H_2$ or $Si-H$ stretching mode on internal surfaces or in voids
2140	$Si-H_3$ stretching mode

Table 3.2: Summary of the peak position of absorption bands typical for μc-Si:H and the corresponding mode description according to [115, 116].

frared absorption of the wagging mode multiplied with the A_{640} proportionality constant:

$$N_H = A_{640} \int_{\nu} \frac{\alpha(\nu)}{\nu} d\nu \tag{3.4}$$

Several values for A_{640} are discussed in literature as well as an iterative method to calculate A_{640} as a function of the amount of bonded hydrogen [119, 120, 117]. Since it is not the scope of this work to investigate different values for A_{640} a value of $2 \times 10^{19}\, cm^{-2}$ was used for the calculation [117]. The hydrogen content C_H^* of the silicon film was calculated by

$$C_H^* = \frac{N_H}{N_{Si} + N_H} \tag{3.5}$$

where $N_{Si} = 5 \times 10^{22}\, cm^{-3}$ represents the silicon density of the material. For thin layers with a layer thickness below $1\, \mu m$ the infrared absorption might be overestimated due to multiple reflections at the air/film interface leading to erroneous values for the hydrogen content. Therefore the hydrogen content C_H^* has to be corrected by the following equation [121], where d represents the film thickness:

$$C_H = \begin{cases} \frac{C_H^*}{1{,}72 - 0{,}7\, d\,(\mu m)^{-1}} & , d_{th} < 1\ \mu m \\ \\ C_H^* & , d_{th} \geq 1\ \mu m \end{cases} \tag{3.6}$$

For thin silicon films the oxygen content can be detected by the *IR* spectroscopy when its concentration exceeds $0.5\, at\,\%$ [116]. The oxygen content was investigated with an analogues procedure, as for the hydrogen content, taking the absorption bands between

$980\,cm^{-1}$ and $1200\,cm^{-1}$. The amount of bonded oxygen atoms can be calculated by the integrated intensities of these absorption bands and the proportionality constant A_O:

$$N_O = A_O \int_{\nu} \frac{\alpha(\nu)}{\nu} d\nu \tag{3.7}$$

In this work a value of $7.8 \times 10^{18}\,cm^{-2}$ was used for A_O [116]. The oxygen content was calculated by:

$$C_O = \frac{N_O}{N_{Si} + N_O} \tag{3.8}$$

3.5.5 Investigating the defect density in thin-film materials

To investigate the defect density of the fabricated material electron spin resonance (*ESR*) measurements have been applied. *ESR* enables the possibility to investigate paramagnetic defect states below the fermi level [122]. During the *ESR*-measurement the samples are exposed to a magnetic field of varied intensity. For the resonance case the first derivative of the absorption signal becomes zero. This zero-crossing point of the *ESR*-signal is defined as the g-value, which changes depending on the type of defect and the nature of its environment. By integrating the *ESR*-signal the defect density N_S of the investigated material can be calculated. The *ESR* technique as a tool to investigate defects in amorphous and microcrystalline silicon is described in reference [123]. Detailed descriptions of defects in microcrystalline silicon studied by *ESR* and their implications on carrier transport can be found in [124, 125, 126].

ESR measurements were performed with a Bruker ELEXSYS E500 continuous wave X-band ($9.2\,GHz$) spectrometer. A calibrated sputtered silicon sample with 2×10^{15} spins was used as a reference sample [127]. To improve the signal to noise ratio and to avoid impairment due to the detection limit of the spectrometer the *ESR* measurements were performed on powder samples. Therefore the depositions were performed on aluminum foil which served as a temporary substrate. After the deposition the aluminum foil was etched away by 12.5 % diluted hydrochloric acid. The powder was then rinsed, dried, and sealed in quartz tubes under helium atmosphere. Details about the sample preparation technique as well as an investigation whether the preparation technique influences the investigated material properties can be found in reference [128].

3.5.6 X-ray diffraction

X-ray diffraction (*XRD*) measurements enable to investigate the structural properties of thin silicon films. With the wavelength of X-ray radiation being in the *pm* to *nm* range

feature sizes down to 3 *nm* can be detected. A comprehensive introduction to the basic principles of *XRD* can be found in Spieß et al. [129].
Here μc-Si:H single layers deposited on glass have been measured by a Bruker D8 Advance diffractometer. A detailed description of the measurement setup as well as the evaluation procedures can be found in reference [130].
The interaction between X-ray radiation and the electrons in a crystallographic structure lead to diffraction patterns. These patterns are characteristic for the probed material and thus allow conclusions about its structural properties. Two setup configurations were used to investigate the samples by *XRD*:

- **Bragg-Brentano (*BB*) geometry:** When using *BB* geometry the radiation source and the detector are moved symmetrically on a semi-sphere around the sample. Therefore the incident beam is guided towards the sample with an angle of θ with respect to the sample surface. The diffracted radiation is measured with the same angle θ. It is important to note that the scattering vector, which is spanned by the wave vectors of the incident and the diffracted radiation, is perpendicular to the substrate surface. Therefore only lattice planes parallel to the substrate can be detected when the *BB* geometry is applied. Care has to be taken when evaluating *XRD* spectra of thin-film silicon since measurements with *BB* configuration probe the whole layer which may also include contributions from the substrate.
- **Grazing incidence (*GI*) configuration:** The grazing incidence configuration is an asymmetrical geometry where the incident beam is guided with a fixed angle ($< 1°$) γ towards the substrate. The detector moves again around the sample on a semi-sphere. When measuring with *GI* geometry the penetration depth of the incident beam varies with the angle γ. The *GI* measurement routine is surface sensitive. Depending on the thickness and the absorption coefficient of the sample it is possible to collect diffraction patterns without distortions from the substrate by the appropriate choice of γ.

In the present work *XRD* measurements were applied to investigate the crystal size δ of the coherent domains, the integrated intensities of the diffraction peaks attributed to the (111), (220), and (311) lattice planes of cubic silicon, and the crystalline volume fraction I_c^{XRD} of the films.
For the evaluation of the crystalline volume fraction the diffraction peaks at $28.44°$, $47.3°$, and $56.12°$ corresponding to the reflections of the (111), (220), and (311) lattice planes were fitted by Pseudo-Voigt profiles. The crystalline volume fraction was then calculated by the ratio of the integrated intensities attributed to crystalline silicon and the sum of the intensities attributed to amorphous and crystalline silicon. Through the Scherer formula the grain size of the coherent domains was calculated from the width of

the fitted peaks. The evaluation procedures are described in detail in reference [130].

3.5.7 Transmission electron spectroscopy

The application of transmission electron spectroscopy (TEM) allows to investigate the structure of materials on an atomic scale. The fundamentals of TEM can be found in numerous textbooks e.g. in Rosenauer [131]. The application of TEM to investigate the microstructure of μc-Si:H was described in the work of Houben [132].
During the TEM investigation a highly energetic beam of electrons is guided towards the sample. The interaction of the electron beam with the sample leads to scattered, diffracted, and directly transmitted electrons. An aperture placed behind the sample allows to select electrons which contribute to the imaging. The low mass of the electrons prevents structural damage during the measurement. The application of energies of several hundreds of keV causes the de Broglie wavelength of the electrons to be within the pm range [131]. Thus a resolution in the sub nm range can be achieved.
For bright field (BF) images only the directly transmitted electrons are considered. Therefore regions which do not scatter or diffract the electron beam appear bright. Regions which deviate the electron beam appear dark. For dark field (DF) images only scattered or diffracted electrons are considered.
In contrast to BF images in DF images regions which do not deviate the electron beam appear dark. Regions which deviate the electron beam lead to bright regions in the TEM image.
For μc-Si:H e. g. in BF images the crystal grains appear dark while the grain boundaries appear bright. For DF images it is the other way around. It is important to note that the visualisation of a crystal in a TEM image depends on its orientation with respect to the incident beam. Therefore only crystals which fulfill the Bragg condition can be visualized by TEM.
In the present work the TEM investigations have been performed at the Ernst Ruska-Centre for Microscopy and Spectroscopy with Electrons of the Forschungszentrum Jülich GmbH. Descriptions of the preparation procedures, measurement routines, as well as the measurement equipment can be found in the recent work of Heidt [133].

3.5.8 Secondary ion mass spectrometry

Secondary ion mass spectrometry ($SIMS$) is a destructive method to analyze the chemical composition of solids and liquids. The fundamentals of $SIMS$ can be found in many textbooks [134, 135].
In the present work μc-Si:H layers deposited on double side polished CZ-wafer were analyzed by a quadrupole Atomika 4000 instrument. Primary Cs^+ ions with an energy

of 6 keV were used to sputter the sample surface at near-normal incidence. The total scan width was 250 μm with the ion beam exhibiting a full width at half maximum of 30 μm and a beam current of 40 nA. The investigations were performed at a residual gas pressure of less than 2×10^{-10} hPa. Measurements at ultra high vacuum conditions prevent distortions from moisture or adsorption of ambient gases on the sample surface. Furthermore collisions of secondary ions with ambient gases are avoided [134].
When the primary ions impact onto the sample surface ionized particles, so called secondary ions, are emitted and subsequently analyzed by a mass spectrometer. *SIMS* investigation enable to measure changes in the chemical composition as a function of the erosion time. Thus, at known erosion rate it is possible to compile a depth profile of specific species. *SIMS* depth profiling was applied to study the concentration of monoatomic oxygen (O^-), monoatomic carbon (C^-) and diatomic carbon (C_2^-) in the silicon layers.
Further information on the local distribution of the oxygen in the material can be obtained by examining the monoatomic and diatomic carbon ion species in the *SIMS* data. Assuming a similar distribution of oxygen and carbon in the material [136]. The evaluation procedure was first presented at the workshop "Particle - surface interactions: from surface analysis to materials processing" in June 2013 in Luxembourg [137] and is derived in detail in appendix A.

3.6 Solar cell characterization

3.6.1 Solar cell current-voltage characteristic

The current-voltage characteristic of thin-film solar cells were measured under standard conditions with a class A Wacom-WXS-140S-Super sun simulator. The temperature of the solar cells was controlled to 25 $^\circ C$. The measurements were performed under $AM\,1.5$ light spectrum with a constant illumination intensity of $1000\,W/m^2$. The intensity and the homogeneity of the measurement setup was calibrated before each measurement. Details about this setup can be found in [138].
On the standard $10x10cm^2$ sized sample, 36 solar cells with varying surface areas (maximum 1 cm^2) and shape were realized. In this thesis the parameters of the best solar cell out of 18 quadratic $1x1cm^2$ sized solar cells is presented as the result for one $10x10cm^2$ substrate.
Figure 3.7 shows a current-voltage characteristic of a typical μc-Si:H single junction solar cell. The following photovoltaic-parameter can be extracted from such a current-voltage curve:

Short-circuit current density J_{sc}:

The short-circuit current density is defined as the ratio of the current I_{sc} generated

under short-circuit conditions and the area of the solar cell.

$$J_{sc} = \frac{I_{sc}}{A} \tag{3.9}$$

Open circuit voltage V_{oc}:

The open circuit voltage describes the voltage generated under open circuit conditions ($I = 0$).

Efficiency η:

The conversion efficiency of a solar cell is defined as the ratio of the maximum power generated by the device (product of V_{MPP} and I_{MPP}) and the incident power.

$$\eta = \frac{P_{max}}{P_{in}} = \frac{V_{MPP}\, I_{MPP}}{P_{in}} \tag{3.10}$$

Fill Factor FF:

The fill factor is defined as the ratio of the maximum power generated by the device (product of V_{MPP} and I_{MPP}) and the product of J_{sc} and V_{oc}. The fill factor can be regarded as a measure for the material quality of the absorber layer.

$$FF = \frac{P_{MPP}}{I_{sc}\, V_{oc}} = \frac{V_{MPP}\, I_{MPP}}{I_{sc}\, V_{oc}} \tag{3.11}$$

When measuring p-i-n single junction solar cells optical filters can be used to derive information about different depth of the solar cell. Depending on the nature of the filter different regions in the solar cell are probed. When measuring with a blue-filter ($BG7$-filter, bandpass centered around 480 nm) charge carriers are assumed to be generated mostly at the pi-interface. When measuring with a red-filter ($OG590$-filter, low-pass filter with a cut-off wavelength of 590 nm) the photovoltaic-parameter are attributed to the bulk material of the solar cell since charge carriers are generated mainly in the intrinsic absorber layer. The short circuit current densities collected with the blue- and the red-filter are defined as $J_{sc,\,blue}$ and $J_{sc,\,red}$, respectively.

3.6.2 Quantum efficiency measurements

The external quantum efficiency (EQE) of solar cells give detailed information about the solar cells spectral response. The EQE is defined as the ratio of extracted electrons and the number of impinging photons onto the surface of the solar cell. In other words the EQE describes the probability that a photon hitting the surface of the solar cell generates an electron hole pair which contributes to the photocurrent density J_{ph}. The EQE is

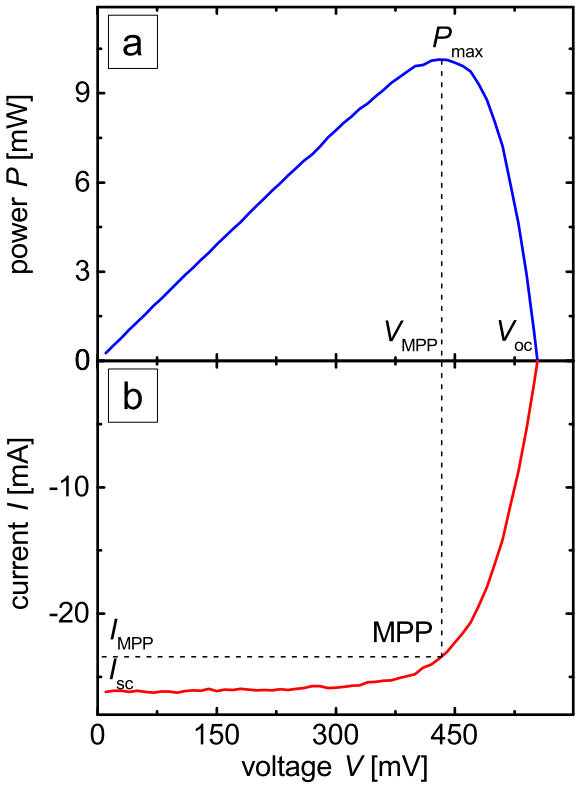

Figure 3.7: Figure (a) shows the output power of a typical μc-Si:H thin-film solar cell as a function of the voltage. Figure (b) shows the corresponding current as a function of voltage. Characteristic photovoltaic-parameters (I_{sc}, V_{oc}, I_{MPP}, V_{MPP},) are indicated in both diagrams.

defined by equation 3.12, where $\Phi(\lambda)$ describes the wavelength depending photon flux.

$$EQE = \frac{J_{ph}(\lambda)/e}{\Phi(\lambda)} \tag{3.12}$$

Integrating the EQE over the wavelength and multiplying with the $AM\,1.5$ photon flux spectrum yields the current density J_{QE} of the device in the wavelength range.

$$J_{QE} = e \int EQE\,\Phi(\lambda)\,d\lambda \tag{3.13}$$

When measuring the EQE of thin-film tandem solar cells the EQE of each subsequent solar cell has to be measured independently. To extract charge carriers out of the device the solar cell which is not measured has to operate in forward conditions due to the series connection of the two sub cells. Therefore this solar cell is saturated by a bias illumination.

Two setups were used to measure the solar cells EQE. With the first setup the samples are illuminated by an $AM\,1.5$ like light source. Spectral filters are used to adjust the wavelength. The spectral resolution for this setup is around $20\,nm$. The second setup which is described in detail in [139] uses the differential spectral response (DSR) technique. The DSR technique is described in detail in [140]. The wavelength can be adjusted by a grating between $300\,nm$ and $1200\,nm$. The highest spectral resolution for this setup is $1\,nm$.

3.6.3 Light degradation

Solar cells with absorbing layers made of intrinsic a-Si:H are affected by the Staebler-Wronski effect (SWE). This effect describes the reduction of dark conductivity in a-Si:H upon illumination [48, 49].

Selected solar cells have been measured after light degradation to investigate the influence of light induced meta-stability on the JV-parameter.

The solar cells were illuminated with an $AM\,1.5$ illumination at $50°C$ in open circuit conditions. The photovoltaic-parameters (see Chapter 3.6.1) of the solar cells were measured after $8\,hours$, $32\,hours$, $145\,hours$, $316\,hours$, $626\,hours$ and $1000\,hours$ of illumination. The external quantum efficiency (see Chapter 3.6.2) was measured before and after the full cycle of $1000\,h$ hours of light induced degradation. In accordance with results obtained at the National Renewable Energy Laboratory (NREL) in Golden Colorado the solar cells photovoltaic-parameter measured after $1000\,h$ are regarded as stabilized [141]. With the stabilized conversion efficiency η_{stb} a degradation ratio can be calculated according to equation 3.14, where η_{ini} describes the initial value of the

solar cells efficiency.

$$\frac{\Delta\eta}{\eta_{ini}} = \frac{\eta_{ini} - \eta_{stb}}{\eta_{ini}} \tag{3.14}$$

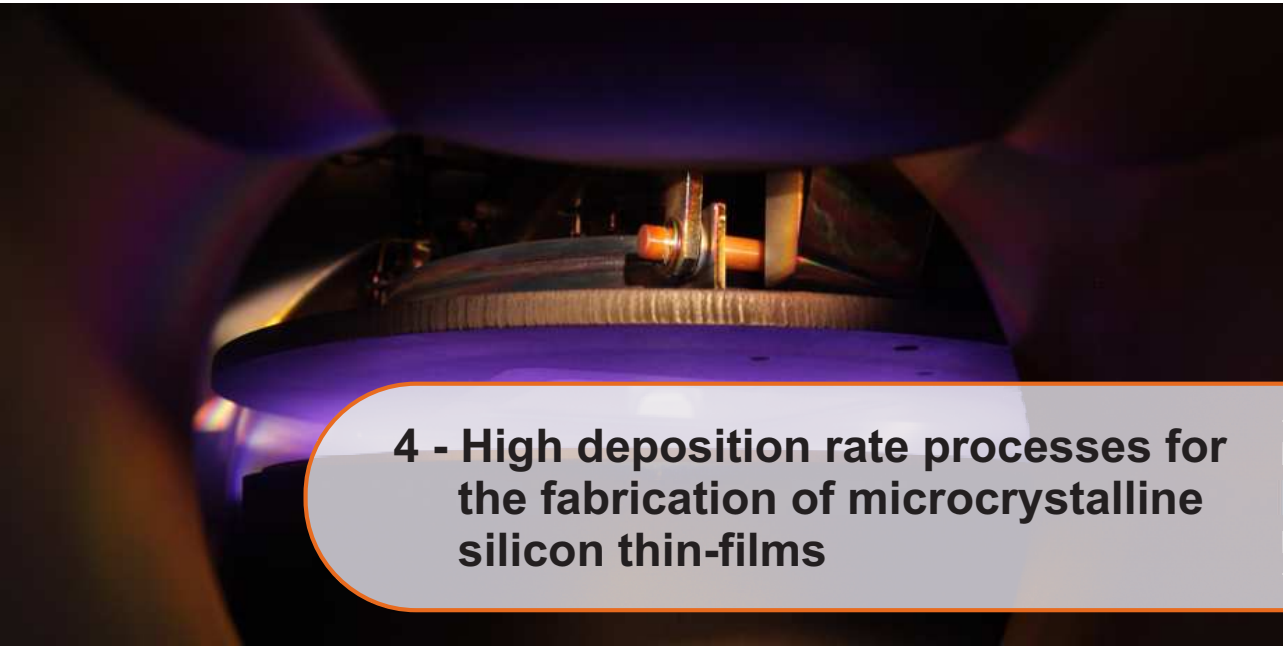

4 - High deposition rate processes for the fabrication of microcrystalline silicon thin-films

In this chapter the results of a process and material development with the aim to increase the deposition rate of μc-Si:H are presented and discussed in detail. The deposited layers were investigated with respect to their structural composition, electrical properties, and material quality. Furthermore attention was drawn to the degree of silane gas utilization of the glow discharge processes.

4.1 Introduction

The high pressure depletion regime together with excitation frequencies in the VHF range (see Chapter 2.3) was applied in order to improve the deposition rate of device grade μc-Si:H. With respect to previous studies performed at the research center in Jülich newly installed deposition facilities (see Chapter 3.1) allowed to vary the electrode distance, the deposition pressure, and the deposition power over an extended range [78, 79]. The goal of the presented process and material development is to increase the deposition rate for the optimal phase mixture material.

As key deposition parameters the electrode distance d, the deposition pressure p, the deposition power P, and the silane concentration were identified. The SC was calculated according to equation 2.1. Three deposition series, labeled series A to C, were performed. The investigated deposition parameters are summarized in Table 4.1.

In series A the electrode distance was varied between 5 mm, 7 mm, and 10 mm while the deposition pressure was kept at 5 hPa and the deposition power at 100 W. In series B the deposition pressure was varied between 3 hPa, 5 hPa, and 8 Pa while the electrode distance was kept at 10 mm and the deposition power at 100 W. In series C the deposition power was varied between 50 W, 100 W, 200 W, 400 W, 600 W at an electrode distance

of 10 *mm* and a deposition pressure of 5 *hPa*. For each investigated parameter set a variation of the *SC* was carried out to cover the whole range from highly crystalline to predominantly amorphous growth. The variation in *SC* was performed by a variation of the silane flow while the hydrogen flow remained constant at 200 *sccm*. According to the silane concentration the deposition time was adjusted to obtain silicon layers with a thickness of $\approx 300\,nm$.

For thickness, Raman, and conductivity measurements the silicon layers were deposited on glass. For *ESR* measurements the silicon films were deposited on aluminum substrates (see Chapter 3.5.5).

For the deposition processes leading to *OPM*-material of series A, B, and C the degree of silane gas utilization U_{sg} was investigated. The U_{sg} describes the ratio between silicon atoms entering the processing chamber and silicon atoms contributing to film growth. It is calculated as follows:

$$U_{sg} = \frac{A_e\, R_D\, N_{Si}}{P[SiH_4]} \tag{4.1}$$

Wherein A_e is the total deposited area, which corresponds approximately to the area of the two electrode plates, R_D is the deposition rate, $P[SiH_4]$ is the silane particle flow into the chamber and N_{Si} is the particle density of the growing film, which is assumed to be the density of crystalline silicon [79]. In case of the theoretical maximum value of 100% for the degree of silane gas utilization half of the silicon atoms entering the chamber contribute to film growth considering same growth rates on both electrodes (powered and grounded) and neglecting deposition on chamber walls. This implicates that no silicon atoms are lost through pumping or powder formation.

Deposition processes in the *HPD* regime are prone for powder formation due to large gas residence time in the discharge zone. Thus targeting processes with a high degree of silane gas utilization can reduce the effort of chamber cleaning. Furthermore the absence or reduction of powder during the processing of silicon films has beneficial effects on the material quality. Strahm et al. showed the *SC* in the discharge zone to be the key deposition parameter for the formation of μc-Si:H [80]. The *SC* in the discharge zone depends on the *SC* entering the deposition chamber and the degree of silane gas utilization. The supply of silane to the discharge zone limits the deposition rate. Furthermore sufficient surface coverage of the growing film by atomic hydrogen has to be ensured for the formation of μc-Si:H (see Chapter 2.1).

series	$Q[H_2]$ $[sccm]$	P $[W]$	d $[mm]$	p $[hPa]$
series A	200	100	5; 7; 10	5
series B	200	100	10	3; 5; 8
series C	200	50; 100; 200; 400; 600	10	5

Table 4.1: Summary of investigated deposition parameters. The deposition parameters are abbreviated as follows: hydrogen flow $Q[H_2]$, deposition power P, electrode distance d, deposition pressure p. Samples deposited at 400 W of series C were investigated by electron spin resonance measurements.

4.2 Material properties and deposition rate

4.2.1 Electrode distance

Figure 4.1a shows the deposition rate for layers prepared at different electrode distances (series A Table 4.1) as a function of *SC*. The layers were prepared at electrode distances of $5\,mm$, $7\,mm$, and $10\,mm$, at a deposition pressure of $5\,hPa$, and a deposition power of $100\,W$. An increase of the deposition rate is observed with increasing *SC*. For fixed values of *SC* there is a trend of an increasing deposition rate with increasing electrode distance for *SC* values below 4%. The Raman intensity ratio for films prepared at different electrode distances is shown in Figure 4.1b. Increasing the *SC* leads to a reduction of the Raman intensity ratio from highly crystalline μc-Si:H to a-Si:H for each investigated electrode distance. The transition from μc-Si:H to a-Si:H growth shifts towards higher values of *SC* with increasing electrode distance. The small window where the phase shift occurs is commonly called the transition region between crystalline and amorphous growth. Thus, with increasing electrode distance the region of optimal crystallinity [142] for solar cells ($40\% < I_c^{RS} < 60\%$) shifts towards higher values of *SC*. This shift of the transition leads to an increase of the deposition rate for *OPM*-material from $0.2\,nm/s$ for $5\,mm$ electrode distance to $1.1\,nm/s$ for $10\,mm$ electrode distance.

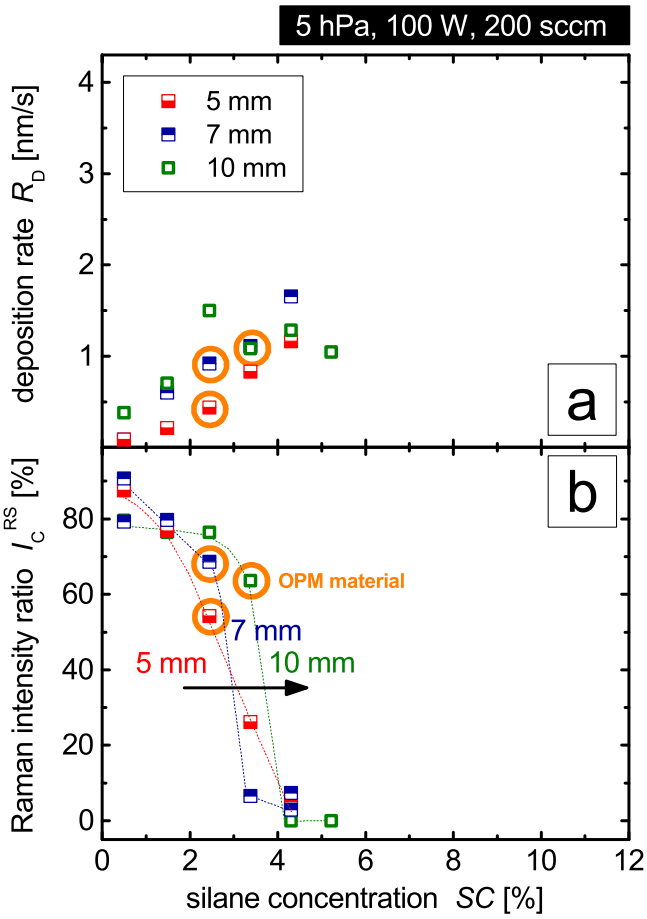

Figure 4.1: Deposition rate R_D (a) and Raman intensity ratio I_c^{RS} (b) as a function of the silane concentration SC calculated using equation 2.1, for the series with varied electrode distance (series A Table 4.1). The samples considered to consist of OPM-material are highlighted by an orange circle.

4.2.2 Deposition pressure

In Figure 4.2a the deposition rate as a function of *SC* for films prepared at different deposition pressures (series B in Table 4.1) is presented. Silicon layers were deposited with a deposition power of $100\,W$, and an electrode distance of $10\,mm$. The *SC* was varied from 0.5% to 7% for deposition pressures of $3\,hPa$, $5\,hPa$, and $8\,hPa$. The deposition rate increases with increasing *SC* as it was also seen in series A , the series with varied electrode distance. No increase of the deposition rate with increasing deposition pressure was observed at a distinct value of *SC*.
Figure 4.2b shows the Raman intensity ratio as function of *SC* for various pressures. The increase of *SC* leads to the reduction of Raman intensity ratio from above 80% to 0%. The sharp transition region between μc-Si:H and a-Si:H is found at nearly the same SC (4%) for deposition pressures of $3\,hPa$ and $5\,hPa$. A further increase of the deposition pressure to $8\,hPa$ leads to a shift of the transition region to *SC* of about 2%. This shift of the transition region to lower *SC* leads to a decreased deposition rate of *OPM* material at higher pressures.

4.2.3 Deposition power

Figure 4.3a shows the deposition rate for layers prepared at different deposition powers (series C Table 4.1) as a function of silane concentration. The material was prepared at deposition powers between $50\,W$ and $600\,W$ at a deposition pressure of $5\,hPa$ and an electrode distance of $10\,mm$. Within considerable scatter an increase of the deposition rate with an increase of *SC* in the range of 0.5% to 11.5% is observed. There is no trend for an increase of the deposition rate with increasing deposition power at a given value of *SC*.
The Raman intensity ratio for films prepared at various deposition powers and various silane concentrations is shown in Figure 4.3b. The increase of *SC* leads to the reduction of Raman intensity ratio from highly crystalline μc-Si:H to a-Si:H for each investigated deposition power. The transition between μc-Si:H and a-Si:H shifts towards higher *SC* and becomes broader with the increase of the deposition power. Thus, the region of the optimal Raman intensity ratio for solar cells (between 40% and 60%) shifts to higher *SC* with increasing deposition power. The shift of the transition region from highly crystalline μc-Si:H to a-Si:H leads to a strong increase in growth rate for OPM material from $0.7\,nm/s$ at $50\,W$ to $2.8\,nm/s$ at $600\,W$.

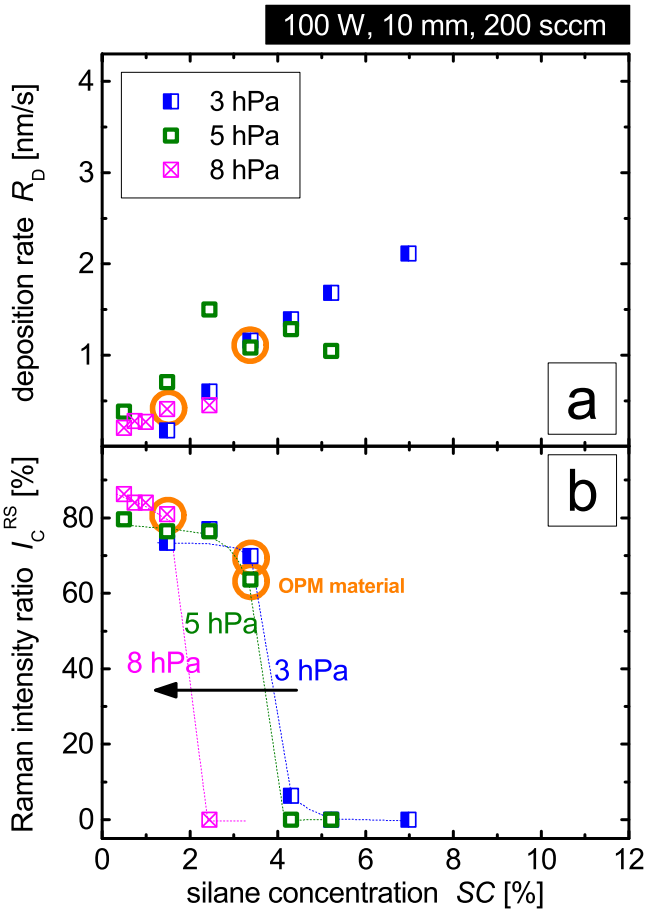

Figure 4.2: Deposition rate R_D (a) and Raman intensity ratio I_c^{RS} (b) as a function of the silane concentration SC calculated using equation 2.1, for the series with varied deposition pressure (series B Table 4.1). The samples considered to consist of OPM-material are highlighted by an orange circle.

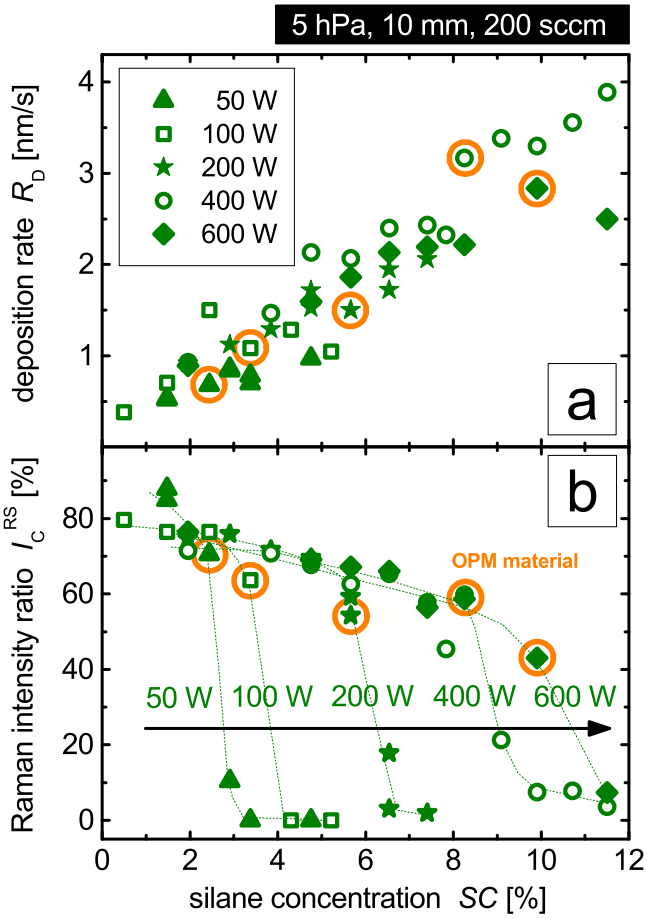

Figure 4.3: Deposition rate R_D (a) and Raman intensity ratio I_c^{RS} (b) as a function of the silane concentration SC calculated using equation 2.1, for the series with varied deposition power (series C Table 4.1). The samples considered to consist of OPM-material are highlighted by an orange circle.

4.3 Electrical transport

4.3.1 Electrode distance

Figure 4.4 shows the photosensitivity (a), the photo conductivity (b), and the dark conductivity (c) as a function of the silane concentration for the series with varied electrode distance (series A in Table 4.1). When describing the general trends of the photosensitivity, the dark, and the photo conductivity, Figure 4.4c shows a decrease in dark conductivity with increasing *SC*. The photo conductivity first increases for *SC* values below approximately 2.4% and than decreases. The decrease in photo conductivity is not as pronounced as the decrease in dark conductivity with increasing *SC*. Consequently the photosensitivity increases several orders of magnitude with increasing *SC* according to the change in dark conductivity.

4.3.2 Deposition pressure

Figure 4.5 shows the photosensitivity (a), the photo conductivity (b), and the dark conductivity (c) as a function of the silane concentration for the series with varied deposition pressure (series B in Table 4.1). Within considerable scatter the photo and the dark conductivity decrease with increasing *SC* independent of the deposition pressure. The samples deposited at a deposition pressure of 5 hPa have already been described in the preceding section as the samples deposited at an electrode distance of 10 mm. The photo conductivity of the samples deposited at a deposition pressure of 3 hPa decrease approximately two orders of magnitude with an increase in *SC* from 2.4% to 7%. The dark conductivity for those samples decreases at the same time over seven orders of magnitude. For the samples deposited at a deposition pressure of 8 hPa the results from photo conductivity measurements range within one order of magnitude. For the dark conductivity a decrease of five orders of magnitude is observed with an increase in *SC* from 0.5% to 2.5%. Since the decrease in dark conductivity is observed to be less pronounced than the decrease in photo conductivity the photosensitivity increases with increasing *SC* for the samples of all three investigated deposition pressures.

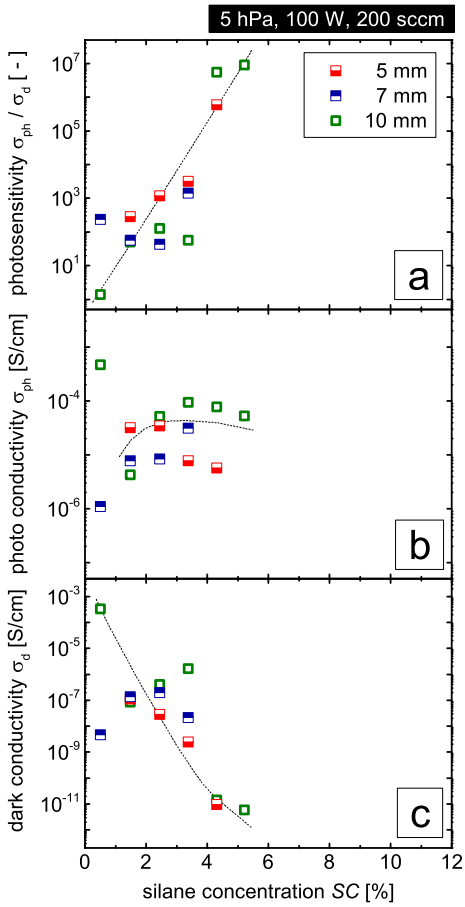

Figure 4.4: Photosensitivity (a), photo conductivity σ_{ph} (b), and dark conductivity σ_d as a function of the silane concentration SC calculated using equation 2.1, for the series with varied electrode distance (series A). The photosensitivity is calculated by the ratio of photo to dark conductivity.

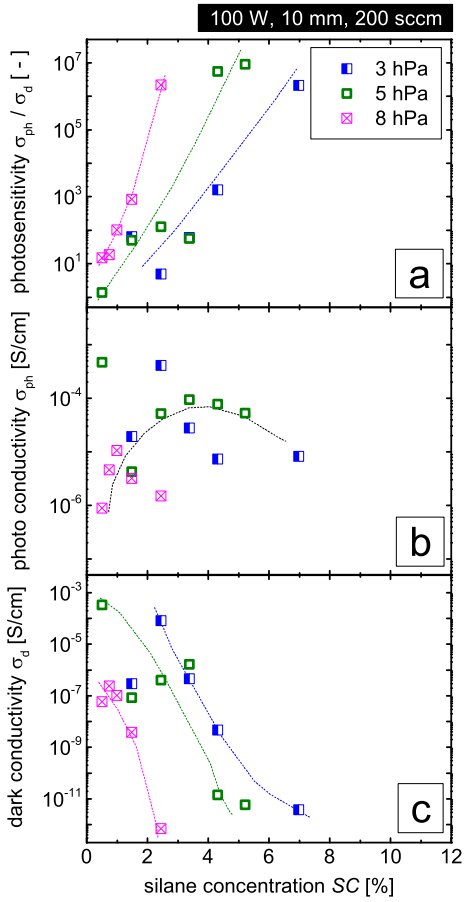

Figure 4.5: Photosensitivity (a), photo conductivity σ_{ph} (b), and dark conductivity σ_d as a function of the silane concentration *SC* calculated using equation 2.1, for the series with varied deposition pressure (series B). The photosensitivity is calculated by the ratio of photo to dark conductivity.

4.3.3 Deposition power

Figure 4.6 shows the photosensitivity (a), the photo conductivity (b), and the dark conductivity (c) as a function of the silane concentration for the series with varied deposition power (series C in Table 4.1). Although a detailed description of the photo conductivity for each deposition power is not possible due to the significant scatter of the experimental data. There is an overall trend for photo conductivity which is observed to decrease with increasing *SC*. A decrease in dark conductivity with increasing *SC* is observed for each deposition power. Although the decrease in dark conductivity is observed for each investigated deposition power the range in dark conductivity reduces with increasing deposition power. Similar to series A and B an increase in photosensitivity is observed for series C with increasing *SC*. This increase is mainly driven by an increase in dark conductivity with increasing *SC*. For the photosensitivity it is possible to distinguish three trends. First an increase in photosensitivity for the samples deposited at deposition powers of $50\,W$ and $100\,W$ is seen between 0.5% and 5.2%. Second an increase in photosensitivity with increasing *SC* for the samples deposited at deposition powers between $200\,W$ and $400\,W$ is observed between *SC* values of 2.0% and 10.7%. Finally for the samples deposited at a deposition power of $600\,W$ the increase in photosensitivity with increasing *SC* is observed between 7.4% and 11.5% of *SC*.
In this section the results from conductivity measurements were shown over the whole range of the *SC*. Thus, samples with a phase mixture ranging from highly crystalline to predominantly amorphous are visualized in Figures 4.4, 4.5, 4.6. This graphical representation makes it challenging to deduce information concerning the optimal phase mixture of the silicon layers. Therefore, results from conductivity measurements are linked to results from Raman measurements for the material considered to consist of *OPM*-material in the following section.

4.4 Defect density and material quality

For the *OPM* material samples taken from series A, B, and C the photosensitivity was measured. In Figure 4.7 the photosensitivity of these samples is plotted as function of the Raman intensity ratio. This plot was proposed by Vetterl et al. [38] as tool to determine the optimal material for solar cell applications. Three areas are defined. Material of area I and area II is of minor interest for the fabrication of intrinsic μc-Si:H used as absorber layer in thin-film solar cells due to low crystalline volume fraction or low photosensitivity, respectively. Area III is defined as target area for the fabrication of absorber layer material for high quality solar cells [38]. The deposition rates are shown as labels for each data point. With the investigated deposition conditions it is possible to deposit μc-Si:H layers attributed to area III over a wide variation of deposition rates.

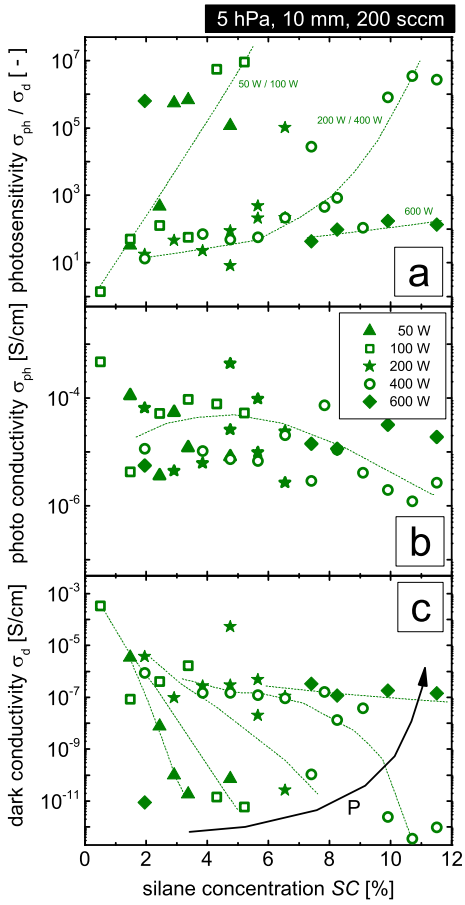

Figure 4.6: Photosensitivity (a), photo conductivity σ_{ph} (b), and dark conductivity σ_d as a function of the silane concentration *SC* calculated using equation 2.1, for the series with varied deposition power (series C). The photosensitivity is calculated by the ratio of photo to dark conductivity.

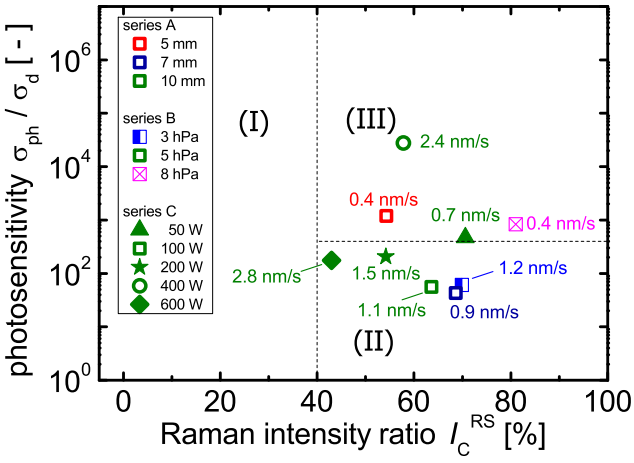

Figure 4.7: Photosensitivity σ_{ph}/σ_d of the optimal phase mixture materials of the series with varied electrode distance, deposition pressure, and deposition power (series A, B, and C) as a function of the Raman intensity ratio I_c^{RS}. The deposition rate is shown for each point. The categorization in area I to III is taken from reference [38]. This categorization was proposed as tool for the development of μc-Si:H thin-film solar cells. Implementing material of area I as the absorber layer leads to a-Si:H solar cells. When implementing material of area II the μc-Si:H solar cells exhibit a low value of open-circuit voltage. The material of are III is identified as optimal material for the processing of high quality μc-Si:H solar cells.

Furthermore, no clear trend between photosensitivity and deposition rate is observed.

Figure 4.8 shows results from *ESR* measurements performed on selected samples of the series with varied deposition power (series C). Two sets of data are presented. First, reference data for samples deposited at conventional low deposition rates taken from reference [126] and, second, the data for the high deposition rate samples of series C in Table 4.1 deposited at a deposition power of $400\,W$.

Figure 4.8a shows the g-value as a function of the Raman intensity ratio. For low values of Raman intensity ratio the g-value is observed to be 2.0049 for samples of series C which is close to the reference sample with a g-value of 2.0050. For the reference series the g-value decreases with increasing Raman intensity ratio down to a value of 2.0046 for a Raman intensity ratio of 84%. For the samples of series C deposited at elevated deposition rates the trend in g-value is not as pronounced as for the reference series. However, overall the samples of series C show similar values compared to the reference

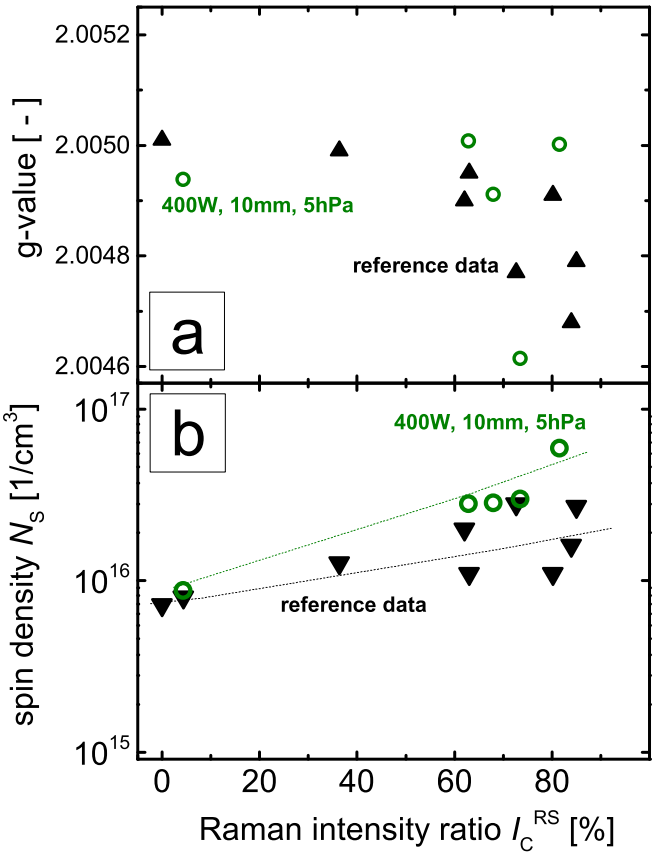

Figure 4.8: The g-value (a) and spin density N_s (b) as a function of the Raman intensity ratio I_c^{RS} for standard low deposition rate reference material (triangles) and samples deposited at high deposition rates (series C) determined by *ESR*.

samples.

Figure 4.8b shows the spin density N_S of the dangling bond resonance in μc-Si:H versus the Raman intensity ratio I_C^{RS}. In the whole Raman intensity ratio range from 0% to 80% the spin density of the high deposition rate material has about the same level as in the reference series. In the Raman intensity ratio range between 40% - 70% all layers which were processed at high deposition rates have N_S of about $2 \times 10^{16} cm^{-3}$ to $3 \times 10^{16} cm^{-3}$ which is similar to the reference material. From this measurement, the same quality of material deposited at low and high deposition rate can be assumed.

4.5 Degree of silane gas depletion

Figure 4.9 shows the deposition rate for the *OPM* material as function of the *SC* for series A, B, and C wherein the electrode distance (a), the deposition pressure (b), and the deposition power (c) were varied. Guiding lines for the degree of silane gas utilization are visualized by grey solid lines.

Figure 4.9a shows an increase in the deposition rate for *OPM* material with increasing electrode distance. The transition zone for the *OPM*-material shifts towards higher values of *SC* with increasing electrode distance. By increasing the electrode distance from 5 *mm* to 7 *mm* the degree of silane utilization doubles from 40% to 80%.

Figure 4.9b shows a shift of the transition zone for the *OPM*-material towards lower values of silane concentration with increasing deposition pressure. This shift of the transition zone is accompanied by a decrease of the deposition rate with increasing deposition pressure. The U_{sg} for the sample deposited at 3 *hPa* is close to 80%. For the samples deposited at 5 *hPa* and 8 *hPa* the U_{sg} decreases to 60% with increasing deposition pressure.

Figure 4.9c shows a clear trend of increasing deposition rate with increasing *VHF* discharge power. *OPM*-material is realized at higher values of silane concentration with increasing deposition power. The increase in deposition rate with deposition power follows the 60%-line of degree of silane gas utilization. Thus, no change in U_{sg} occurs by a variation in deposition power.

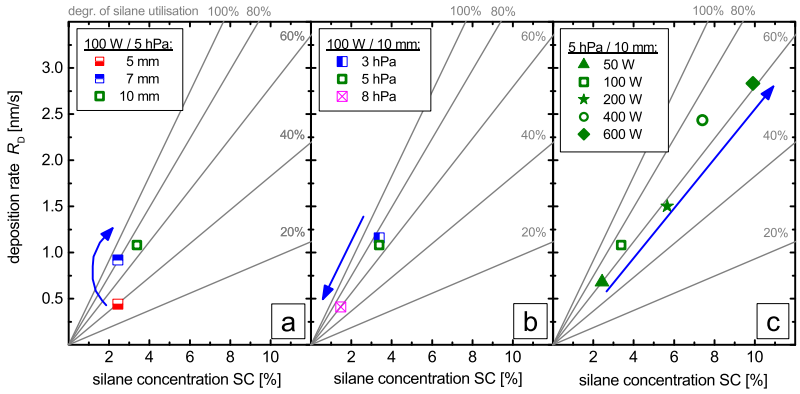

Figure 4.9: Deposition rate R_D of the optimal phase mixture materials of the series with varied electrode distance (a, series A), deposition pressure (b, series B), and deposition power (c, series C) as a function of the silane concentration *SC*. The *SC* is calculated using equation 2.1. The degree of silane gas utilization is calculated according to equation 4.1 and is visualized in each figure in grey solid lines.

4.6 Discussion

Structural composition and deposition rates

The aim of the process and material development was to develop deposition processes which yield *OPM*-material, suitable for the application to thin-film solar cells at elevated deposition rates. As the parameter which yields the strongest variation in deposition rate for the *OPM*-material the deposition power was identified (see Figure 4.3). With increasing deposition pressure the transition from μc-Si:H to a-Si:H growth shifts towards higher values of *SC*. Thus the process window for the *OPM*-material shifts towards higher values of *SC*. Since the deposition rate is limited by the availability of silicon atoms in the glow discharge a shift of the transition zone towards higher values of *SC* enables to achieve higher values of deposition rate with increasing deposition power. If sufficient portion of silane molecules are available in the process gas mixture, an increase of the deposition power leads to an enhanced dissociation and therefore faster film deposition [73].

However, the further increase of discharge power leads finally to silane depletion when most of the silane molecules are decomposed. A further increase in deposition power

does not lead to an increase of the deposition rate. It can be seen in Figure 4.3 that the increase in the deposition power from $50\,W$ to $600\,W$ does not lead to an increase of the deposition rate at a specific value of *SC*. This is an indication for silane depletion already at a deposition power of $50\,W$. In other words nearly every silane molecule in the glow discharge is decomposed at $50\,W$ and further power increase does not lead to additional Si radical production. However, an increase in deposition power leads to an enhanced decomposition of the hydrogen source gas (see Chapter 2.3). The enhanced decomposition of the hydrogen source gas leads to a reduction of the silane-to-hydrogen ratio. This has already been proposed in earlier works [78, 29, 80]. Although the detailed effect of atomic hydrogen during the growth of μc-Si:H is still under debate, all growth models for μc-Si:H attribute atomic hydrogen a dominant role [45, 46, 143] (see Chapter 2.1). This is supported by the observation that an increase of the hydrogen dilution promotes the growth of microcrystalline silicon and that in particular the hydrogen-to-silane radical density is a driving force for crystalline growth in the discussed deposition processes [80]. A higher hydrogen-to-silane radical density at higher discharge power leads to a shift of the growth transition towards higher values of *SC*. Consequently, also the *OPM* material will grow at higher *SC* values under conditions of higher discharge powers. The shift of *OPM* conditions to higher *SC* facilitates finally the increase in the deposition rate up to $2.8\,nm/s$ for *OPM* material achieved in this study. The shift of the *OPM* conditions with increasing discharge power is in good agreement with findings of earlier works [77, 78].

Furthermore the influence of the deposition pressure and the electrode distance as key deposition parameters to achieve high deposition rates for *OPM*-material was investigated. Increasing the deposition pressure reduces the mean free path of charged plasma species, which causes a reduction of the energy of the bombarding ions and is expected to be favorable for low defect density material deposition. An increase of the deposition pressure from $3\,hPa$ to $8\,hPa$ is observed to cause a shift of the transition from μc-Si:H to a-Si:H growth towards lower values of *SC*. This is in good agreement with previous studies [79] and can be attributed to the enhanced presence of silane molecules in the discharge caused by the increased deposition pressure. It is expected that the ratio between hydrogen and silane radical in the glow discharge is reduced and less crystalline material is obtained, with an increase in the deposition pressure. Thus, the shift of the *OPM* regime to lower *SC* takes place with an increase in deposition pressure.
Changing the electrode distance induces a change in the discharge volume. Furthermore the ratio between discharge volume and background volume is varied by a change in electrode distance. The background volume describes the whole chamber volume

apart from the volume between the two planar electrodes. When applying the *HPD* regime silane, radicals in the discharge zone are depleted after the ignition of the glow discharge. As a consequence the chamber's background volume is predominantly filled with hydrogen [144]. This effect is further pronounced by the application of showerhead gas supply since the process gases are directly fed into the discharge zone. As already mentioned the *SC* as it is defined by the mass flows of the involved process gases (see equation 2.1) does not necessarily follow a one to one relation with the *SC* present in the glow discharge. However, the latter one is determining the phase mixture of the growing film [80].

The shift of the transition zone from μc-Si:H growth to a-Si:H growth towards higher values of *SC* with increasing electrode distance is in conflict to results reported earlier [78, 79]. These studies also showed an increase in deposition rate with increasing electrode distance. Both effects were attributed to an increased number of silane particles in the discharge zone due to the increased discharge volume. Here an increase in deposition rate with increasing electrode distance is also seen. However, an increased number of silane particles due to the increased discharge volume is in conflict to the shift of the transition zone. An increased number of silane particles should lead to a shift of the transition zone towards lower values of *SC*. The origin of this discrepancy is presently not known. One hypothesis is that the reactions taking place in the glow discharge are to complex to be described by a simple increase in discharge volume neglecting possible secondary effects. E. g. different pumping rates for silane and hydrogen may alter the discharge chemistry up on an increase in electrode distance.

The increase in deposition rate with increasing electrode distance support the observations obtained from the investigations on the degree of silane gas utilization. The increase in deposition rate may be related to an increased degree of silane utilization for the samples deposited at an electrode distance of $7\,mm$ and $10\,mm$ with respect to $5\,mm$. For the samples deposited at an electrode distance of $7\,mm$ and $10\,mm$ the degree of silane gas utilization is calculated to be approximately 80% while for the narrow gap of $5\,mm$ it was calculated to be around 40%.

Due to the shift of the transition zone with increasing electrode distance and the linear increase in deposition rate with increasing *SC* the deposition rate for the *OPM* material increases with increasing electrode distance. By a variation from $5\,mm$ to $10\,mm$ the deposition rate is increased from $0.4\,nm/s$ to $1.1\,nm/s$.

Electrical transport

In general the results from electrical transport measurements performed by conductivity measurements show the typical picture for mixed phase materials consisting of variable

amounts of a-Si:H and μc-Si:H. Dark conductivity values in the range of $10^{-6}\,S/cm$ to $10^{-12}\,S/cm$ as well as photo conductivity values in the range of $10^{-4}\,S/cm$ to $10^{-5}\,S/cm$ have been reported since μc-Si:H became interesting for photovoltaic applications [7]. Also the strong decrease in dark conductivity with increasing *SC* as well as the moderate decrease in photo conductivity which leads to an increase in photosensitivity with increasing *SC* was reported [7]. The typical measurement uncertainty attributed to conductivity measurements can lead to significant scatter of the experimental data.
Due to the scatter it is not possible to relate a variation in electrode distance to a change in dark or photo conductivity values for series A. However, photosensitivity values above 10^2 for *SC* values of 1.5% (5 *mm*) and 2.4% (10 *mm*) indicate the presence of solar grade μc-Si:H at the transition region between μc-Si:H and a-Si:H growth [38].
For series B the slope of the decrease in dark conductivity flattens with decreasing deposition pressure. Hence, for the samples deposited at a deposition pressure of 8 *hPa* typical conductivities of $10^{-12}\,S/cm$ attributed to a-Si:H are reached at low values of *SC* compared to the samples deposited at 5 *hPa* and 3 *hPa*. These results support observation obtained through Raman measurements. A shift of the transition zone from μc-Si:H to a-Si:H growth towards higher values of *SC* was observed with decreasing deposition pressure. Photosensitivity values above 10^2 for deposition pressures of 5 *hPa* and 8 *hPa* for *SC* values of 3.4% and 1.5% indicate the presence of high quality μc-Si:H layers at the transition zone between μc-Si:H and a-Si:H growth.
For series C the slope of the decrease in dark conductivity flattens with increasing deposition power. This effect supports the observation gained through Raman measurements. The Raman measurements show a shift of the transition zone from μc-Si:H to a-Si:H growth towards higher values of *SC* with increasing deposition power. Due to the significant scatter it is not reasonable to relate variations in the photo conductivity to a variation in the deposition power. Photosensitivity values beyond 10^2 for the samples deposited at deposition powers of 200 *W*, 400 *W*, and 600 *W* for *SC* values of 5.7%, 8.3%, and 9.9% indicate the presence of high quality μc-Si:H layers close to the transition zone from μc-Si:H to a-Si:H growth.
According to the results gained through conductivity measurements it is reasonable to conclude that for each investigated deposition parameter it is possible to deposit solar grade μc-Si:H.

Material quality

For series A, B, and C a photosensitivity in the range of 10^2 to 10^4 is observed (see Figure 4.7). But no strict link between the photosensitivity and the deposition rate is identified. When considering the photosensitivity as a measure for the material quality the experimental data suggests that high quality material can be fabricated at

high deposition rates. Thus, with the present criteria established in literature [38] it is reasonable to conclude that device grade material can be deposited up to deposition rates up to $2.8\,nm/s$ as shown with Figure 4.7.

Another indication for good material quality *ESR* measurements show a spin density of $\approx 3 \times 10^{16}\,cm^{-3}$ for materials with a Raman intensity ratio ranging between 40% and 70% deposited at high deposition rate as has been shown exemplary for selected samples. The spin density of the reference samples extend over the same range compared to the samples deposited at elevated deposition rates. Thus, an increase in defect density with increasing deposition rate is not observed for investigated deposition regime.

The g-value shows a typical characteristic for thin silicon films deposited at various values of Raman intensity ratio. The decrease in g-value with increasing Raman intensity ratio was reported earlier and its shift with Raman intensity ratio is not explained conclusively in literature [145, 146]. For the samples with the lowest value of I_c^{RS} the value attributed in literature to pure a-Si:H films of 2.0055 is not reached. In previous studies this effect was speculated to be related to a variation in the medium range order between the material under investigation and pure a-Si:H films [146]. The overall good agreement of the g-value for the reference samples and the samples deposited at elevated deposition rates suggest that the nature of the defects as well as their energy does not change by a variation of the deposition rate.

The results gained through *ESR* measurements support the feasibility to produce device grade μc-Si:H deposited at high deposition rates.

Degree of silane gas depletion

Strahm et al. showed the feasibility to describe the formation of μc-Si:H by the silane input concentration to the discharge zone and the degree of silane gas utilization. The degree of silane gas utilization comprises the process parameters deposition power, deposition pressure, silane concentration, excitation frequency, and electrode distance. Thus, the degree of silane gas utilization contains quantities describing the dissociation of the process gases (deposition power, excitation frequency) and those which describe the gas residence time in the discharge zone (deposition pressure, total gas flow, electrode distance) [80]. Bugnon et al. proposed to increase the silane input concentration while simultaneously increasing the degree of silane gas utilization to keep the silane concentration in the discharge zone constant in order to achieve high deposition rates for μc-Si:H [147]. Furthermore, a decrease in defect density with increasing degree of silane gas utilization was reported [147].

The strongest increase in deposition rate from $0.7\,nm/s$ to $2.8\,nm/s$ for OPM material is seen for an increase in deposition power from $50\,W$ to $600\,W$ (series C). During the strong variation in deposition power the degree of silane gas utilization stays almost

constant around 60%, which is an indication that the conditions for silane depletion is reached. Already at a discharge power of 50 W most of the silane source gas is decomposed.

Increasing the deposition pressure leads to an increase in gas residence time. At the same time the energy of the impinging ions on the growing surface is reduced due to a decreased mean free path of the discharge particles. The decrease in silane gas depletion with increasing deposition pressure is related to pronounced gas phase reactions with increasing gas residence time [80]. A decrease in deposition rate with increasing deposition pressure is related to the shift of the transition zone towards lower values of *SC* with increasing deposition pressure. For low values of *SC* the deposition rate is limited by the low availability of silicon atoms.

The increase in degree of silane gas utilization with increasing electrode distance has already been reported [79]. This observation can also be related to pronounced gas phase reactions at high electrode distances. Increasing the electrode distance increases the discharge volume and thus the probability of gas phase reactions. As discussed earlier the shift of the transition zone from μc-Si:H to a-Si:H growth towards higher values of silane concentration with increasing electrode distance is in contrast to results reported earlier [78, 79].

4.7 Conclusion

Table 4.2 summarizes the experimental data obtained through thickness, Raman, conductivity, and *ESR* measurements to characterize the material quality of μc-Si:H layers considered to consist of *OPM*-material deposited at elevated growth rates for series A, B, and C.

A broad range of deposition parameters was covered in the process and material development aiming at an increase of the deposition rate for intrinsic microcrystalline silicon. The possibility to cover such a broad range of deposition parameters has been enabled by the installation of new deposition facilities (see Chapter 3.1). Increasing the discharge power in the VHF band at high deposition pressures enabled to achieve deposition rates up to 2.8 nm/s for optimal phase mixture material. According to Schropp et al. [148] and Vetterl et al. [38] the photosensitivity can be used as a relevant measure for the quality of the absorber layer. In the mentioned references it was claimed that photosensitivity values above 100 or 400 together with values above 40% for the Raman intensity ratio are favorable for high quality solar grade material. As can be seen from Table 4.2 for the majority of the deposited samples photosensitivity values beyond 100 with spin density values in the order of $10^{16}\,cm^{-1}$ are achieved. It is shown that it is possible to deposit μc-Si:H at elevated growth rates which meets the established criteria in literature

	R_D $[nm/s]$	I_c^{RS} $[\%]$	$\sigma_d/\sigma_{ph} > 10^2$ $[-]$	U_{sg} $[\%]$	N_s $[cm^{-3}]$	g-value $[-]$	area*
series A							
5 *mm*	0.4	54	$\surd$	40			III
7 *mm*	0.9	69	$\times$	80			II
10 *mm*	1.1	64	$\times$	80			II
series B							
3 *hPa*	1.2	70	$\times$	80			II
5 *hPa*	1.1	64	$\times$	80			II
8 *hPa*	0.4	81	$\surd$	60			III
series C							
50 *W*	0.7	71	$\surd$	80			III
100 *W*	1.1	64	$\times$	80			II
200 *W*	1.5	54	$\surd$	80			II
400 *W*	2.4	58	$\surd$	80	2×10^{15}	2.005	III
600 *W*	2.8	43	$\surd$	80			II

$\star$ according Figure 4.7

Table 4.2: Summarized measurement results for layers considered to consist of *OPM*-material series A, B, and C obtained by thickness, Raman, conductivity, and *ESR* measurements. These results are used to characterize the material quality of the μc-Si:H layers deposited at elevated deposition rates. The measurement results describe the deposition rate R_D, the Raman intensity ratio I_c^{RS}, the dark σ_d and photo conductivity σ_{ph}, the degree of silane gas depletion U_{sg}, the spin density N_s, and the g-value. The area references to the classification according to Figure 4.7 which is based on criteria described in [38].

for state of the art solar cells. Additionally, no link between the material quality of the μc-Si:H layers deposited close to the transition zone between μc-Si:H and a-Si:H growth and the deposition rate has been observed. These results suggest the feasibility to fabricate high quality μc-Si:H absorber layers at high deposition rates with high values of silane gas utilization. At high values of silane gas depletion most silane atoms entering the deposition chamber contribute to film growth. Increasing the *SC* under those conditions enables to increase the deposition rate due to the increasing supply of silicon atoms. Overall the results obtained here are in good agreement with results already present in the literature [149, 79]. Only the shift of the transition zone from μc-Si:H to a-Si:H growth towards higher values of *SC* with increasing electrode distance is in contrast to previous studies [78, 79].

The high quality makes the high rate material interesting for the application as absorber layer in thin-film solar cells. Implementing these materials as an absorber layer in thin-film solar cells is a way to further investigate their applicability to opto-electronic devices. This approach is presented and discussed in detail in Chapter 6.

Further investigations on microstructure, oxygen uptake and porosity of μc-Si:H are presented in Chapter 5 to get a deeper insight in the material properties.

5 - Investigation of porosity, atmospheric gas diffusion, and microstructure in microcrystalline silicon fabricated at high growth rates

In the present chapter results of a detailed investigation of μc-Si:H layers with promising material properties for solar cell application identified by the process and material development (see Chapter 4) are presented and discussed. The μc-Si:H layers were investigated with respect to their microstructure, oxygen uptake after storage and evolution of the Raman intensity ratio along the growth axis. Additional investigations by X-ray diffraction measurements and Transmission Electron Microscopy imaging complete the picture.

5.1 Introduction

For the study presented in Chapter 4 the strongest variation in deposition rate for the *OPM*-material was observed for series C, the series of varied deposition power. It was shown that the deposition power as one key deposition parameter is suitable to adjust the deposition rate over a broad range. Furthermore, it was shown that the deposition rate for *OPM*-material scales with the deposition power. In order to perform *IR*, *TEM*, and *SIMS* measurements the layers had to be deposited on *Si* wafer substrates.

It is generally found that processes which yield high growth rates lead to deteriorated electronic properties of μc-Si:H by introducing defects, porosity and high hydrogen content [150, 74]. Besides being of inferior quality already in the as-deposited state, material with pronounced porosity is subject to meta- and in-stability effects caused by in-diffusion, adsorption and chemical bonding of atmospheric gases [40]. These effects have been already studied in detail both on μc-Si:H material and on solar cells with corresponding absorber layers [40, 151, 152, 153, 154, 150, 74]. In the study presented

in this chapter the effect of enhanced deposition rates on the μc-Si:H material structure and the post-deposition oxidation was investigated.

Samples were deposited on glass and *Si* wafer substrates. The growth rate of the μc-Si:H was varied between $0.7\,nm/s$ to $2.3\,nm/s$ by varying the deposition power P from $100\,W$ to $600\,W$ and the silane concentration SC from 2.4% to 7%. The definition of the SC is given in Chapter 2.1 by equation 2.1. For all samples the hydrogen flow was kept constant at $200\,sccm$. Other deposition parameter e. g. deposition pressure, electrode distance, and substrate temperature remained unchanged. The μc-Si:H deposition time was adjusted according to the growth rate to achieve a layer thickness of $700\,nm$. The deposition conditions are summarized in Table 5.1.

The silicon post-oxidation after storage at ambient air was investigated by infrared spectroscopy and by secondary ion mass spectrometry on selected samples. The material structural composition was determined by Raman spectroscopy and by X-ray diffraction measurements. Raman depth profiles allowed to investigate the evolution of the Raman intensity ratio along the growth axis.

Two sets of samples with high Raman intensity ratio (set 1: $I_c^{RS} = 75\%$ - 84%) and medium Raman intensity ratio (set 2: $I_c^{RS} = 43\% - 74\%$) were prepared. Microcrystalline silicon material with a medium crystallinity is considered to be optimal for the application as absorber layers in thin-film solar cells [7]. Hence, sample set 2 represents such optimal material. Furthermore, a sample deposited at a low deposition rate ($0.2\,nm/s$) under low power ($20\,W$) and low pressure ($1\,hPa$) conditions served as a reference. The deposition parameters and the range in deposition rate and Raman intensity ratio covered by each sample set are summarized in Table 5.1.

The infrared spectra were taken for different time periods after the deposition. The first measurement within $30\,min$ after the deposition will be referred to as the as-deposited state. Measurements after 10 days, 30 days, 90 days, and 180 days of storage in ambient atmosphere allowed investigating the oxygen uptake as a function of time. After 180 days of storage the samples were etched for $15\,s$ in hydrofluoric acid (HF). Afterwards IR spectra were recorded again within $30\,min$ after the etching procedure. The difference between the oxygen content before and after the etching step is calculated and will be referred to as ΔC_O.

	P $[W]$	SC $[\%]$	R_D $[nm/s]$	I_c^{RS} $[\%]$
sample set 1	$100-600$	$2.4-3.8$	$0.7-1.4$	$75-83$
sample set 2	$100-600$	$3.9-7.0$	$1.1-2.3$	$43-74$
reference sample	20	5.2	0.2	69

Table 5.1: Deposition parameters and measurement results for sample set 1 and sample set 2. During the preparation of the layers the deposition power P and the silane concentration SC was varied, while the deposition pressure p and the electrode distance d remained unchanged at $5\,hPa$ and $10\,mm$, respectively. The range in deposition rate R_D is indicated as well as the range of the Raman intensity ratio I_c^{RS}.

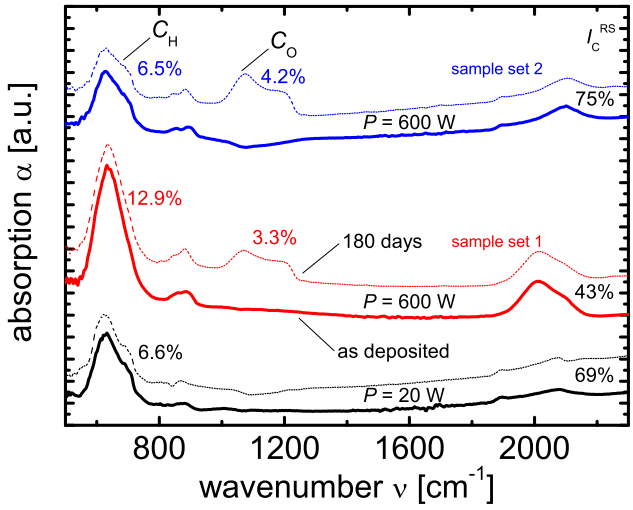

Figure 5.1: Infrared spectra for three selected samples in the as deposited state and after 180 days of storage at ambient. The deposition power P, the Raman intensity ratio I_c^{RS}, the calculated hydrogen content C_H, and the calculated oxygen content C_O are indicated close to the according spectra. The sample deposited at a deposition power of $20\,W$ serves as a reference. Two samples deposited at a deposition power of $600\,W$ are shown in the figure each from a different set of samples. Two sets of samples with high (set 1: $I_c^{RS} = 75\% - 84\%$) and medium (set 2: $I_c^{RS} = 43\% - 74\%$) Raman intensity ratio have been investigated.

5.2 Investigation of structure and porosity of μc-Si:H by IR

Figure 5.1 shows infrared spectra of three selected samples in the as-deposited state and after 180 days of storage at ambient. The presence of oxygen can be seen by the evolution of an absorption band between $980\,cm^{-1}$ and $1200\,cm^{-1}$ which is characteristic for $Si-O-Si$ stretching and bending modes. The oxygen content C_O was calculated by adapting the method to calculate C_H [116], but using the absorption bands between $980\,cm^{-1}$ and $1200\,cm^{-1}$ (see Chapter 3.5.4).

The sample deposited at a deposition power of $20\,W$ and a SC of 5.2% is taken as a reference sample representing device quality material with a Raman intensity ratio of 69%. The two other samples were deposited at $600\,W$ and a SC of 7.0% and 4.8% which resulted in a Raman intensity ratio of 43% and 75%, respectively. The reference sample shows no oxygen uptake within 180 days of storage at ambient. Both samples deposited at $600\,W$ show a strong increase of the oxygen absorption modes. An oxygen content of

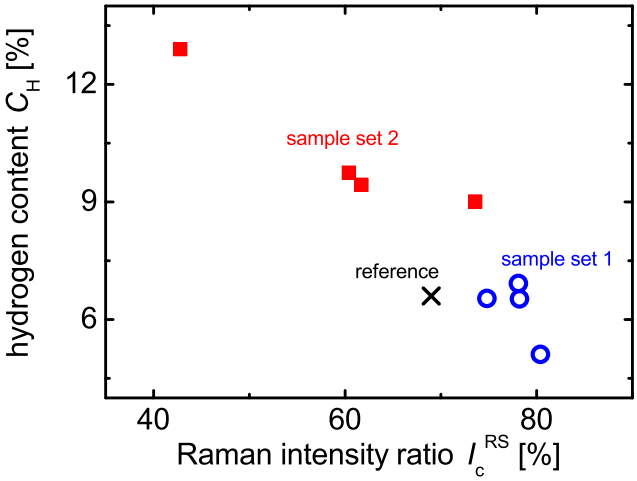

Figure 5.2: Calculated hydrogen content C_H for the two sets of samples with high (set 1: $I_c^{RS} = 75\% - 84\%$) and medium (set 2: $I_c^{RS} = 43\% - 74\%$) Raman intensity ratio are shown as a function of the Raman intensity ratio I_c^{RS}. For the C_H no change with exposure time to ambient was observed.

3.3% and 4.2% was calculated after 180 days for the samples with I_c^{RS} of 43% and 75% respectively. For the reference sample the hydrogen content was calculated to 6.6%. The hydrogen content was evaluated to 12.9% and 6.5% for the samples with I_c^{RS} of 43% and 75% respectively.

Figure 5.2 shows the evaluated hydrogen content as a function of the Raman intensity ratio. The C_H decreases from 12.9% for the samples of set 2 with an I_c^{RS} of 43% down to 5.1% for the sample with an I_c^{RS} of 80%. For layers of sample set 1 where the Raman intensity ratio varies between 75% and 83% the hydrogen content is observed to be between 5.1% and 6.9%. For the reference sample deposited at a deposition power of $20\,W$ the hydrogen content was calculated to 6.6%. For the C_H no change with exposure time to ambient was observed.

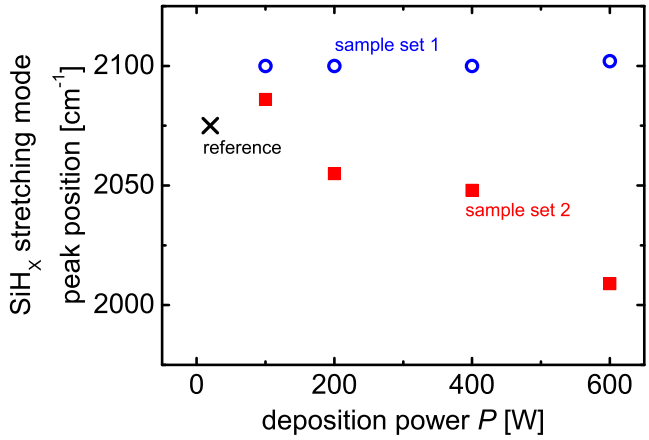

Figure 5.3: Position of the SiH_X stretching mode as a function of the deposition power P for sample set 1 and sample set 2 (see Table 5.1). As a reference the SiH_X stretching mode for a sample deposited at low deposition rates is also displayed in the diagram.

Figure 5.3 shows the position of the SiH_X stretching mode for the as deposited state as a function of the deposition power. For the samples with high Raman intensity ratio, set 1, the peak position of the SiH_X stretching mode stays around $2100\,cm^{-1}$ independent of the deposition power. For the samples of medium Raman intensity ratio, set 2, the peak position decreases continuously with increasing deposition power. For a deposition power of $100\,W$ the peak position is detected at $2086\,cm^{-1}$, while at a deposition power of $600\,W$ a shift of the peak position towards $2009\,cm^{-1}$ is observed. This is a hint for a change in microstructure with increasing deposition power for the samples of set 2. For the reference sample deposited at a deposition power of $20\,W$ the position of the SiH_X stretching mode is observed to be at $2075\,cm^{-1}$.

Figure 5.4 shows the calculated oxygen content as a function of exposure time to ambient air after preparation of sample set 1 and sample set 2. Significant oxygen uptake was only found for samples deposited at $200\,W$ and beyond. The oxygen content is increases with increasing exposure time for samples deposited at a deposition power of $200\,W$ or beyond for samples of both sample sets. For the layers of sample set 1 (in blue) with high Raman intensity ratio the oxygen content increases with decreasing deposition power and increasing I_c^{RS}. For the samples of set 2 (in red), with medium Raman intensity ratio, the oxygen uptake increases with increasing deposition power and decreasing I_c^{RS}. Overall the post-deposition oxidation for sample set 1 is more

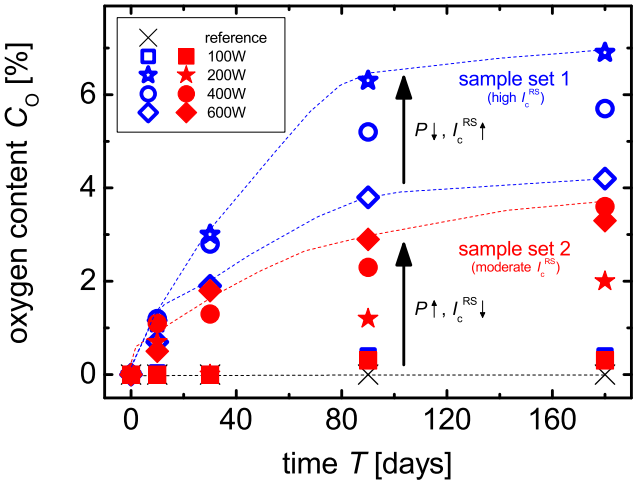

Figure 5.4: Oxygen content of μc-Si:H layers as a function of storage time at ambient. The layers were deposited at various deposition powers. Two sets of samples with high (set 1: $I_c^{RS} = 75\% - 84\%$) and medium (set 2: $I_c^{RS} = 43\% - 74\%$) Raman intensity ratio are shown in the figure.

pronounced than for the samples of set 2.

Figure 5.5 shows the difference between the oxygen content ΔC_O evaluated before and after an etching step of 15 s in HF solution as a function of I_c^{RS}. The HF etching was performed to investigate if the oxygen content can be linked to the oxidation of cracks or surfaces with contact to the ambient air. Totally inner surfaces can not be reached by the HF acid. For layers of sample set 1 a considerable change of the oxygen content can be measured due to the etching procedure. For layers of sample set 2 no significant change of the oxygen content due to the etching step is observed.

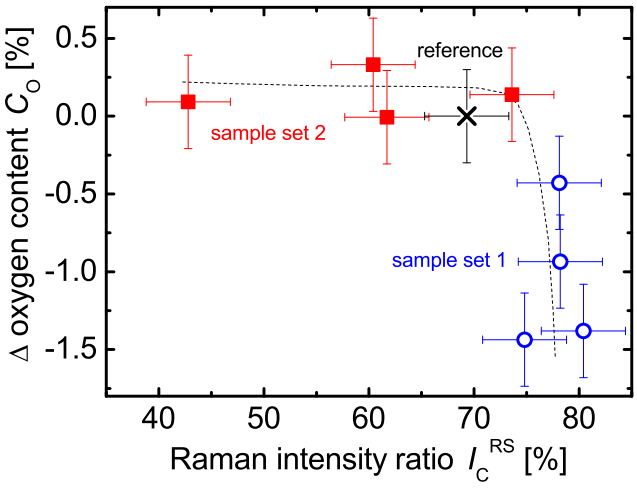

Figure 5.5: Difference in oxygen content before and after a etching step in hydrofluoric acid as a function of the Raman intensity ratio for sample set 1 and sample set 2 (see Table 5.1).

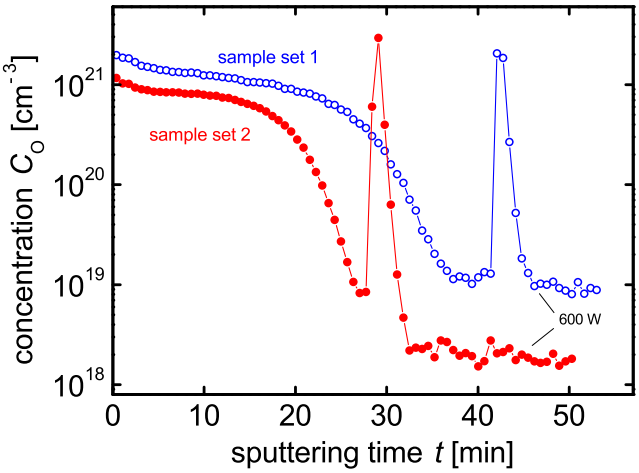

Figure 5.6: *SIMS* profile of two selected samples both deposited at a deposition power of 600 W each from a different set of samples (set 1 and set 2, see Table 5.1).

5.3 Investigating diffusion path of oxygen for μc-Si:H by SIMS

Figure 5.6 shows the oxygen concentration profiles investigated by *SIMS* as a function of the sputtering time for two samples deposited at 600 W from both sample sets. The samples were deposited on *Si* wafer. A high level of oxygen concentration extending from the film surface (sputtering time $t = 0\,min$) far into the film (sputtering time $20\,min < t < 30\,min$) is found for both samples before the oxygen concentration decreases by two orders of magnitude towards the film/wafer interface. The film/wafer interface is characterized by the high oxygen peak from the native oxide of the *Si* wafer in both samples. The oxygen concentration at the surface is $2.0 \times 10^{21}\,cm^{-3}$ and $1.2 \times 10^{21}\,cm^{-3}$ for sample 1 and 2, respectively.

The slope of the oxygen concentration as a function of the sputtering time implies a fast process of oxygen uptake [155, 156]. Thus, it is reasonable to conclude that the oxygen uptake occurs along the grain boundaries or void surfaces as opposed to diffusion through the bulk material.

5.4 Investigating the evolution of the Raman intensity ratio along the growth axis by Raman depth profiling

Figure 5.7 shows the Raman depth profiles for samples of set 1 (a) and set 2 (b). A Raman depth profile of a sample deposited at a deposition power of 20 W serves as a reference in both diagrams. The reference sample shows a gradual increase in Raman intensity ratio with increasing layer thickness. As a reference point a layer thickness of 0 nm corresponds to the substrate surface. Beyond a thickness of 300 nm the Raman intensity ratio saturates at approximately 70%.

For the samples of high Raman intensity ratio (Figure 5.7a), set 1, the increase in Raman intensity ratio with increasing layer thickness shows a significant different shape than for the reference sample. Compared to the reference sample the samples of set 1 show a steeper increase in Raman intensity ratio for low values of layer thickness. Furthermore, the Raman intensity ratio saturates for lower values of layer thickness. The lowest value of I_c^{RS} of 54% (at substrate/film interface) is observed for the sample deposited at a deposition power of 200 W. The point of saturation is reached for the highly crystalline samples at around 100 nm independent of the deposition power. The Raman intensity ratio of samples of set 1 saturates between values of 84% for a deposition power of 200 W and 75% for a deposition power of 600 W.

For the samples with medium Raman intensity ratio (Figure 5.7b), set 2, a similar trend as for the samples of set 1 is observed. The slope of the Raman intensity ratio as a function of the layer thickness is steeper for low values of layer thickness. Thus, the Raman intensity ratio saturates already at lower values of layer thickness compared to the reference samples. The lowest value of I_c^{RS} of 36% (at substrate/film interface) is observed for the sample prepared at a deposition power of 600 W. The Raman intensity ratio for the samples of set 2 saturates with increasing thickness at a layer thickness between 100 nm and 130 nm. For a deposition power of 100 W a value of saturated Raman intensity ratio of 84% is observed. With increasing deposition power this value decreases down to 60% for a deposition power of 600 W. This shift of the Raman intensity ratio towards lower values with increasing deposition power for OPM-material has already been observed in the process and material development study presented in Chapter 4. Interestingly, an increase in deposition power from 400 W to 600 W leads to a rather strong decrease of the Raman intensity ratio of more than 10% in absolute scale. Whereas an increase in deposition power from 100 W to 200 W or from 200 W to 400 W leads to a decrease in Raman intensity ratio of 5% and 7%, respectively.

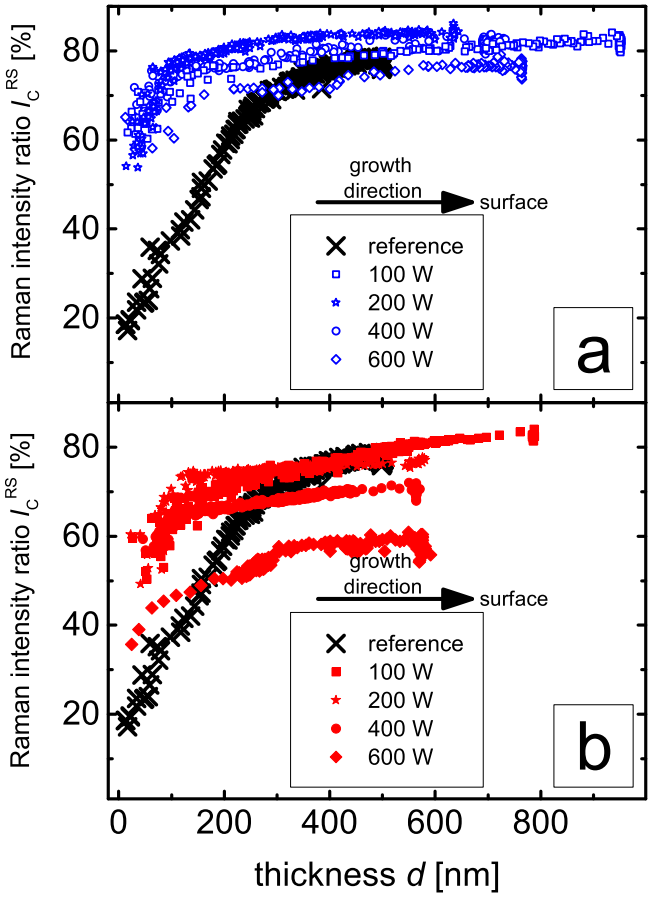

Figure 5.7: Raman depth profile for samples of set 1 (a) and set 2 (b). A Raman depth profile obtained for a reference sample deposited at a deposition power of 20 W has been added in both diagrams.

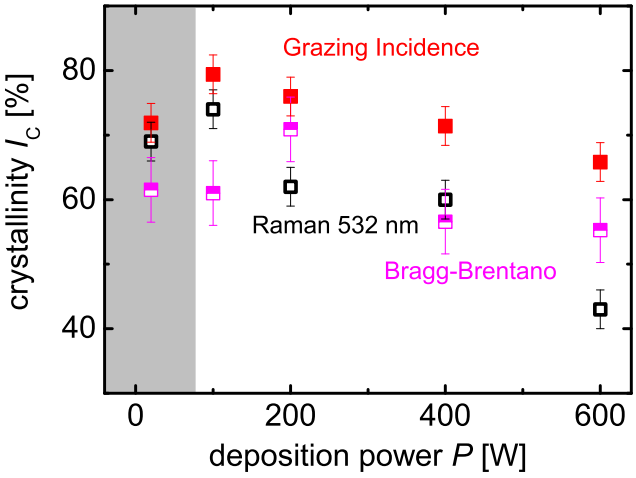

Figure 5.8: Crystallinity I_c determined by *XRD* as a function of the deposition power P for samples of set 2. The crystalline volume fraction has been determined by grazing incidence as well as Bragg-Brentano geometry (see Chapter 3.5.6). Additionally the I_c^{RS} determined by Raman spectroscopy with an excitation wavelength of $532\,nm$ is displayed in the graph. The values of the reference sample deposited at a deposition power of $20\,W$ are highlighted by a grey background.

5.5 Structural investigation by XRD and Raman spectroscopy

Figure 5.8 shows the crystallinity I_c as a function of the deposition power for the samples of medium crystallinity, set 2. Values are derived by three different measurement methods: Raman measurements with an excitation wavelength of $532\,nm$, and *XRD* measurements using *BB* as well as *GI* geometry. The experimental data obtained for the reference sample deposited at a deposition power of $20\,W$ is highlighted by a grey background.

For the deposition powers of $100\,W$ and beyond a decrease in crystallinity is observed with increasing deposition power for the values by through *XRD* measurements in *GI* geometry and for the values obtained through Raman measurements. For the values obtained through *XRD* measurements in *BB* geometry only a slight decrease in crystallinity with increasing deposition power is observed. This effect is not of significant nature due to the high measurement uncertainty of the *XRD* measurement routine in *BB* geometry due to contributions from the glass substrate. Independent of the deposition power the values obtained by *XRD* measurements with *GI* geometry show the highest

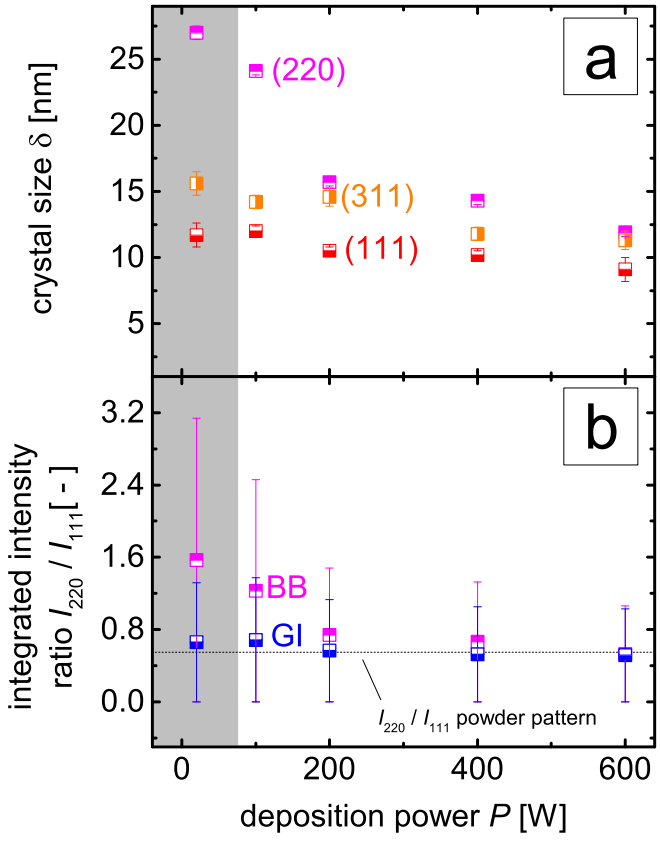

Figure 5.9: Crystal size δ of the coherent domains as a function of the deposition power P (a). Ratio of integrated intensities I_{220}/I_{110}, measured in *GI* as well as in *BB* geometry, as a function of the deposition power P (b). The crystal size was deduced from the diffraction peak associated to the (220) lattice planes, measured in *BB* geometry. I_{220}/I_{110} describes the ratio of the integrated intensities of the diffraction peaks attributed to the (220) and (111) lattice planes. The reference sample data are highlighted by a grey background. In (b) the integrated intensity I_{220}/I_{110} of a silicon powder pattern is shown as a guiding line.

value of crystallinity.

Figure 5.9a shows the crystal size δ of the coherent domains as a function of the deposition power. The crystal size was determined from the diffraction peaks attributed to the (311), (220), and the (111) lattice planes (see Chapter 3.5.6). The value for the reference sample deposited at a deposition power of $20\,W$ is highlighted by a grey background.

The crystal size decreases with increasing deposition power independent of the diffraction peak used to determine the crystal size. The highest values for the crystal size are observed for the values deduced from the diffraction peak associated to the (220) lattice planes. For the reference sample a crystal size of $27\,nm$ is observed. With increasing deposition power the crystal size decreases down to a value of $12\,nm$ for a deposition power of $600\,W$. For the crystal size deduced from the diffraction peak associated to the (311) lattice planes a decrease from $16\,nm$ to $11\,nm$ is observed. The lowest values for crystal size are observed for the values deduced from the diffraction peak associated to the (111) lattice planes. There a decrease in crystal grain size from $12\,nm$ to $9\,nm$ is observed with increasing deposition power.

Figure 5.9b shows the ratio of the integrated intensities for the diffraction peaks attributed to the (220) and the (111) lattice planes measured in *GI* as well as in *BB* geometry as a function of the deposition power. The values measured for the reference sample are highlighted by a grey background. As a guideline the intensity ratio of the reflections of a sample with random orientation (silicon powder pattern $\{111\} : \{220\} = 1 : 0.55$) is displayed in the same figure [157]. In the early works on μc-Si:H performed at the research center in Jülich the crystal growth of μc-Si:H is described as a random process [132, 158]. Meaning that crystals are formed in every possible orientation without the presence of a preferential orientation. When comparing the integrated intensities deduced from the *XRD* diffraction patterns a complete random growth process should yield values close to the powder pattern. In literature a preferential growth along the $[110]$ axis is deduced when comparing the ratio of the integrated intensities attributed to the (220) and (111) lattice planes to a silicon powder pattern. It is important to note that when measuring in *BB* configuration only an orientation normal to the substrate surface can be detected due to the measurement geometry (see Chapter 3.5.6). For measurements performed in *GI* geometry the scattering vector changes constantly, in direction and in absolute value, therefore it is not possible to test a preferential orientation in a specific direction with the *GI* geometry. However, if the integrated intensities measured in *GI* geometry show significant deviations from the powder patter it is an indication for a preferential orientation.

The integrated intensity ratio I_{220}/I_{111} for the measurements performed in *BB* geometry

decrease with increasing deposition power (see Figure 5.9). A decrease from 1.57 for a deposition power of $20\,W$ down to 0.53 for a deposition power of $600\,W$ is observed. At a deposition power of $600\,W$ the integrated intensity ratio corresponds to the value obtained for the powder pattern. The values of the integrated intensity ratio measured in *GI* do not differ significantly from the values obtained for the powder pattern for deposition powers of $200\,W$ and beyond. The highest value of 0.7 for the measurement performed in *GI* geometry is observed for a deposition power of $100\,W$. This means only a slight preferential orientation is seen along the [110] axis for low values of deposition power.

Figure 5.10a shows the position of the TO phonon mode deduced from Raman spectra (see Chapter 3.5.3) as a function of the deposition power. Figure 5.10b shows the full width half maximum ($FWHM$) of the Gaussian distribution fitted to this peak as a function of the deposition power. In both diagrams the according values obtained from a reference sample deposited at a deposition power of $20\,W$ are displayed.

A laser with an excitation wavelength of $488\,nm$ was used. Evaluating the position of the TO phonon mode and the $FHWM$ allows to investigate the presence of compressive or tensile stress in the material (under certain boundary conditions) [159].

For the reference sample the position of the TO phonon mode is at $519.8\,cm^{-1}$. The peak position decreases with increasing deposition power for μc-Si:H layers with a high Raman intensity ratio, set 1. A decrease of approximately $1\,cm^{-1}$ to a value of $518.2\,cm^{-1}$ for a deposition power of $600\,W$ is observed. For μc-Si:H layers of medium Raman intensity ratio, set 2, the TO phonon mode of the sample deposited at a deposition power of $100\,W$ is at $518.8\,cm^{-1}$. With increasing deposition power the position of the TO phonon mode shifts towards a value of $517.7\,cm^{-1}$ for a deposition power of $600\,W$. Considering certain boundary conditions a shift of the TO phonon mode can be attributed to a variation in mechanical stress of the μc-Si:H films.

The $FWHM$ of the Gaussian distribution fitted to the c-Si peak, shown in Figure 5.10b, for the reference sample is at $9.4\,cm^{-1}$. For both sets of samples an increase in $FWHM$ with increasing deposition power is observed within significant scatter. This is a hint for a decrease in crystal size with increasing deposition power. This result supports the findings obtained through *XRD* measurements, where for samples of set 2 a decrease in crystal size with increasing deposition power has also been observed (see Figure 5.9).

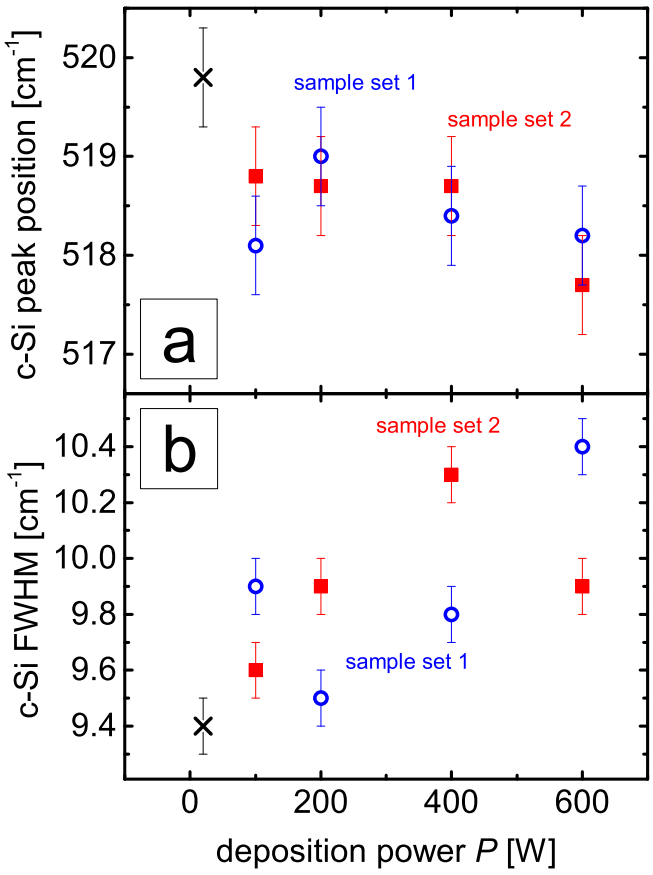

Figure 5.10: Position of the TO phonon mode of the Raman spectra (a) and full width half maximum $FWHM$ of the Gaussian distribution fitted to this peak (b) as a function of the deposition power for samples of set 1 and set 2. Corresponding values obtained from a μc-Si:H layer prepared at a deposition power of $20\,W$ are displayed in both diagrams as reference values.

5.6 TEM investigations of μc-Si:H layers at various deposition rates and Raman intensity ratios

Figure 5.11 shows the bright field TEM images of selected μc-Si:H layers deposited on glass. Figure 5.11a shows the image of the reference sample deposited at a deposition power of $20\,W$ with a deposition rate of $0.2\,nm/s$. Figures 5.11b and c show the bright field images of samples related to sample set 2 fabricated at a deposition power of $100\,W$ and $400\,W$, respectively. Finally, Figure 5.11d shows the bright field image of the sample of sample set 1 deposited at a deposition power of $400\,W$.

The quantitative evaluation of TEM images has to be done with great caution, since the images show only those crystal columns which fulfill the Bragg condition. Furthermore, a wrong impression might arise induced by different thicknesses of the lamella investigated for each sample. The same thickness of each lamella can not be guaranteed. However, being fully aware of the boundary conditions of the TEM technique the bright field images are described qualitatively here. The qualitative description of the TEM images can complement the experimental data presented so far.

Going from Figures 5.11a to c a gradual decrease of the incubation layer is observed. For the reference sample (a) an incubation layer with a thickness of more than $120\,nm$ is observed. At a deposition power of $100\,W$ (b) the incubation layer is approximately $80\,nm$ thick. For the layer deposited at a deposition power of $400\,W$ (c) it is not possible to identify the presence of an incubation layer.

For the reference sample a conical growth of the crystal columns can be observed. These columns coalesce with neighboring columns after approximately $120\,nm$. Beyond this point of coalescence the crystal columns continue to grow normal to the substrate surface. The width of the crystal columns is in the range of $120\,nm$. Going from Figures 5.11a to c it can be seen that the width of the crystal columns decrease with increasing deposition power from approximately $90\,nm$ for a deposition power of $20\,W$, over $60\,nm$ for a deposition power of $100\,W$, to finally $40\,nm$ for a deposition power of $400\,W$. Looking at Figures 5.11b to d it can be seen that due to the reduced incubation layer thickness the conical growth at the substrate/film interface is suppressed, the coalescence of the crystal columns occurs closer to the substrate compared to the reference sample. Leading to a parallel growth of the crystal columns. Comparing Figure 5.11c to d both deposited at a deposition power of $400\,W$ a reduced width of the crystall columns and an increase in crack density is observed for the sample visualized in Figure 5.11d. Cracks and voids in μc-Si:H are observed as white lines between the crystal columns in TEM bright field images.

As a summary of the TEM investigations it is reasonable to note a decrease in column width with increasing deposition power. Furthermore, the thickness of the incubation

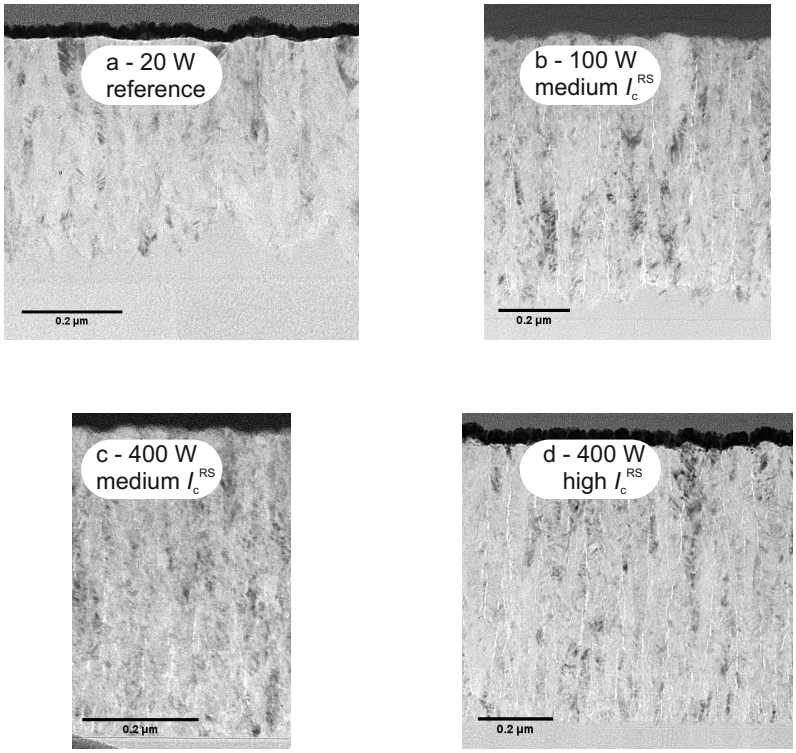

Figure 5.11: Bright field *TEM* images of selected silicon layers on glass: for a reference sample deposited at a deposition power of $20\,W$ (a), two samples of sample set 2 deposited at deposition powers of $100\,W$ and $400\,W$ (b, c), and one sample of sample set 1 deposited at a deposition power of $400\,W$ (d). Two sets of samples with high (set 1: $I_c^{RS} = 75\% - 84\%$) and medium (set 2: $I_c^{RS} = 43\% - 74\%$) Raman intensity ratio have been investigated.

layer decreases with increasing deposition power. Finally, an increase in crack density is observed for highly crystalline material compared to the *OPM*-material.

5.7 Discussion

In the process and material development, presented in Chapter 4, the possibility to apply processes which yield high deposition rates for the fabrication of μc-Si:H absorber layers was investigated. According to electron spin resonance, conductivity and Raman measurements the feasibility to produce "device grade" material over a broad range of deposition rates was shown. In this context, the definition of "device grade" material, is based on empirical data which summarizes structural and electronic properties of μc-Si:H material which, when applied as absorber layer in solar cells, yields high solar conversion efficiencies [38]. It is important to consider that the process conditions to obtain high growth rates with high discharge power could adversely affect the solar cell performance via e.g. generating defective interfaces. An additional study investigating possible damage of interfaces induced by the deposition processes yielding high deposition rates is presented in Chapter 6.

The key process parameters to govern the growth rate of μc-Si:H over a large range in the present study are the deposition power and the silane concentration. When varying the deposition power it is necessary to adapt the *SC* to grow *OPM* μc-Si:H with medium Raman intensity ratio (see Chapter 4). Apparently, this adjustment of power and *SC* alters the material structure composition and hence e. g. the substrate/film interface, the formation of the incubation layer and the ability of oxygen uptake. The reference material deposited at deposition rates of $0.2\,nm/s$ is resistant to post-deposition oxygen uptake. This is one of the preconditions for stable, high performance μc-Si:H solar cells.

Effects of deposition power and deposition rate on hydrogen content, oxygen uptake, and material porosity

The decrease in hydrogen content with increasing Raman intensity ratio for samples of set 2 is attributed to the decrease in volume content of the hydrogen rich amorphous phase. This effect is well documented in literature [160]. The low values obtained for samples of set 1 around a hydrogen content of 6% are attributed to the high values ($> 75\%$) of Raman intensity ratio for these layers. A hydrogen content of 6.6% observed for the reference sample at a Raman intensity ratio of 69% is a typical value for device grade μc-Si:H deposited at low deposition rates.

A variation of the shape of the peaks attributed to the SiH_X stretching modes is attributed

to a variation of the hydrogen bonding [115, 161]. For samples of set 1 the SiH_X stretching modes were exclusively observed at a wavenumber of $2100\,cm^{-1}$. The appearance of stretching modes around $2100\,cm^{-1}$ is an indication for hydrogen bonded on internal surfaces [115]. Internal surfaces can originate e. g. from grain boundaries, crystal grains, and void rich silicon films. The shift of the position of the SiH_X stretching mode with increasing deposition power observed for samples of set 2 indicate a more compact film structure with increasing deposition power. Two effects may cause this shift. On the one hand, a decrease in crystallinity giving rise to a pronounced amorphous volume content with increasing deposition power altering the hydrogen bonding. On the other hand, an enhanced ion bombardment with increasing deposition power can lead to a compact layer [30].

Strong oxygen uptake by samples of set 1 is attributed to the overall higher Raman intensity ratio, which is typically accompanied by an increased porosity of the layers. Therefore, the material is susceptible to in-diffusion of atmospheric oxygen. This assumption is supported by *IR* measurements where the SiH_X stretching vibrations of samples of set 1 are observed to be exclusively at a wavenumber of $2100\,cm^{-1}$ which is an indication for a porous film structure. For samples of set 1 the amount of oxygen incorporated after deposition scales with the Raman intensity ratio. This is in line with the assumed increase in porosity at higher crystallinity. The reduction in oxygen content for samples of set 1 upon the HF etching step is attributed to an enhanced porosity of layers of samples set 1 compared to samples of set 2 which were deposited close to the transition range between μc-Si:H and a-Si:H growth, which is in agreement with earlier findings [162]. A change in oxygen content induced by the HF etching step indicates that the oxygen uptake takes place through open surfaces reachable by the ambient atmosphere. A diffusion of the oxygen through the bulk material seems unlikely. Considering the structural composition of μc-Si:H it is reasonable to assume the oxygen uptake to occur along the grain boundaries which is in line with the findings from *SIMS* measurements which will be discussed later.

For sample set 2 the oxygen uptake also increases with increasing deposition power but also increases with decreasing Raman intensity ratio. Again it is important to consider the relationships between discharge power and silane concentration which have to be adjusted simultaneously in order to obtain material of, in this case, medium Raman intensity ratio for the sample set 2. With an increase in deposition power the transition zone from μc-Si:H to a-Si:H growth is shifted. As a consequence the Raman intensity ratio for the *OPM*-material decreases with increasing deposition power (see Chapter 4). When a decrease of the nano-crystalls size is assumed with decreasing Raman intensity ratio a phase mixture consisting of a considerable amount of a-Si:H with embedded

nano-crystalls results. The increase in oxygen content with decreasing Raman intensity ratio can then be attributed to an overall increase of inner surfaces due to an increase in surface to volume ratio with decreasing Raman intensity ratio.
For samples of set 2 no change of the oxygen content could be detected upon an HF etching step. This indicates a dense material composition with respect to HF penetration for the layers considered to be optimal for device application on the one hand. On the other hand, some of the layers of sample set 2 also take up a considerable amount of oxygen. A possible explanation for this counter intuitive effect will be presented in the next section.

Effect of a variation in Raman intensity ratio on the oxygen diffusion path

Conclusions on the porosity can also be drawn from the *SIMS* profiles and investigations with TEM imaging as will be discussed later. The shape of the *SIMS* profile for both samples indicates the oxygen uptake to occur via a rapid in-diffusion along an open void or grain boundary structure [155]. While this supports the findings from the infrared investigations on both sample sets, it is in conflict with the results after HF etching on sample set 2 where the invariance of oxygen content before and after etching would suggest a compact structure. The reason for this discrepancy is not known at present. Further information on the local distribution of the oxygen in the material can be obtained by examining the monoatomic (O^-) and diatomic (O_2^-) ion species in the *SIMS* data of each sample [137]. From these studies it is concluded that the bonded oxygen is not distributed homogeneously throughout the film orthogonally to the growth direction. This fits into a picture where oxygen diffuses along a porous void or grain boundary structure and is mainly located on these inner surfaces rather than inside the bulk material. A possible explanation for the discrepancy with the HF etching step is that for the sample of set 2 the Raman intensity ratio is lower than for the sample of set 1. Thus, the nano-crystalls are embedded in a matrix with a pronounced presence of a-Si:H tissue possibly accessible for oxygen but not for HF.

Effects of the deposition power and deposition rate on crystal volume content, preferential orientation, and crystal grain size

The higher crystal volume content determined from the measurements performed with *GI* geometry is attributed to a smaller probing depth compared to the measurements performed with *BB* geometry and to the Raman measurement performed with an excitation wavelength of $532\,nm$ (Figure 5.8). When measuring with *GI* geometry the volume close to the surface is probed predominantly, which shows pronounced crystallinity as can be seen from the Raman depth profiles (Figure 5.7b). Measuring with *BB* geometry

in turn probes the whole layer including possible contributions from the underlying glass substrate. Hence, the crystalline volume content is a complicated average over the whole layer thickness. The Raman depth profiles showed for samples of set 2 an increase in Raman intensity ratio with increasing layer thickness (Figure 5.7b). Therefore the values for the crystalline volume content is observed to be lower when determined with *BB* geometry. As already denoted the *XRD* diffractograms recorded in *BB* geometry have to be corrected for possible substrate contributions. This correction procedure may be source for an additional error which reflects in an increased measurement uncertainty.
Independent from the applied measurement procedure the crystallinity of layers of set 2 decreases with increasing deposition power. This confirms the measurements presented in Chapter 4 (see Figure 4.3b).
The existence of a crystallographic texture has been matter of great debate and is still not resolved conclusively. Some studies claim a preferential growth along the $[110]$ direction to be mandatory for the fabrication of high quality solar cells especially to achieve high values of short-circuit current density [163, 164]. Other studies claimed to show a pronounced preferential orientation when approaching the phase transition between μc-Si:H and a-Si:H growth by increasing the silane concentration [165]. In contrast Sugano et al. showed a pronounced value of the integrated intensities attributed to the (220) and (111) lattice planes for low values of silane concentration [166]. Recently several studies performed at the research center in Jülich have shown that no preferential orientation is necessary for the fabrication of high quality thin-film solar cells [167, 130, 168].
Considering the samples of set 2 no significant indication for a preferential orientation is found for the measurements performed in *GI* geometry. Compared to the mentioned literature values only a slight preferential orientation is seen along the $[110]$ growth axis for low values of deposition power for the measurements performed in *BB* geometry. The highest value of 1.6 is observed for a deposition power of $20\,W$ where mild deposition conditions lead to high quality device grade material. The values of the integrated intensity I_{220}/I_{110} approach the values of the powder pattern for deposition powers beyond $200\,W$. The decrease of the integrated intensity I_{220}/I_{110} with increasing deposition power might be attributed to an impairment of the surface of the growing film with increasing deposition rate. Possible sources for an impairment of the growth zone are: damage due to ion bombardment, structural inhomogeneities, or altered nucleation conditions. Houben already observed values exceeding the powder standard by a factor of 2 [132]. The value of 1.6 here exceeds the value reported earlier. However, it is far from the reported values in literature where a preferential orientation is claimed to be mandatory for good solar cell device performance. Matsui et al. reported values around

2.6 and Sugano et al. even values up to 3.8 [164, 166].
The crystal size of the coherent domains decreases with increasing deposition power. This effect is attributed to a decrease in crystallinity with increasing deposition power. A decrease in crystal size can also be related to an impairment of the growth zone. Possible sources for this disturbance have already been mentioned here and will be discussed in detail in Chapter 6.
The decrease in crystal grain size is in line with the increase in random orientation with increasing deposition power deduced from the *XRD* measurements in *BB* geometry (Figure 5.9). Smaller crystall grains can be expected to increase the crystallographic disorder.

Structure profiles along the growth axis for various deposition powers

The structural properties along the growth axis have been investigated by means of Raman depth measurements (Figure 5.7). For the reference sample an incubation layer of approximately 300 *nm* is observed. The presence of an incubation layer has been observed since μc-Si:H became a promising material for photovoltaic applications and is well documented in literature [7]. However the thickness of 300 *nm* is surprisingly high. It can be related to the growth of μc-Si:H on glass substrates. The formation of μc-Si:H was shown to be sensitive to the substrate surface [169, 170] and is more delicate on glass compared to e. g. c-Si wafer substrates [132].
For the samples deposited in the *HPD* regime the incubation layer is thinner. This is related to an enhanced presence of atomic hydrogen. When working at *HPD* conditions the silane source gas entering the deposition chamber is depleted. Hence, the excess of hydrogen in the discharge zone promotes crystalline growth. For sample set 1 and 2 the incubation layer thickness is similar which is attributed to the overall very similar processing conditions. For set 1 the *SC* was varied from 2.4% to 3.8% which is the origin of the overall higher Raman intensity ratio values compared to the values obtained for the samples of set 1. Compared to set 1 for set 2 the *SC* was varied over a larger range of 3.1%. Thus, the Raman intensity ratio decreases over a larger range for set 2 with increasing deposition power. Interestingly, it is not possible to deposit highly crystalline layers at high values of *SC* despite the fact of working at *HPD* conditions with a degree of silane gas utilization of approximately 80% (see Chapter 4 Figure 4.9).
Matsuda showed that by increasing the discharge power the amount of hydrogen ions which are accelerated towards the substrate increases [43]. If a specific threshold value is exceeded the formation of μc-Si:H nuclei is suppressed and can in extreme cases induce an amorphization of the crystalline phase. Furthermore, lattice distortions and a reduction in grain size induced by heavy ion bombardment were reported [43]. These effects might be responsible for the strong decrease in Raman intensity ratio with an

increase in deposition power from $400\,W$ to $600\,W$ for sample set 2.
The results obtained through the Raman depth profiling method supports the observations obtained by the TEM investigations (Figure 5.11). There also a decrease in incubation layer thickness was observed with increasing deposition power. In early studies the presence of an a-Si:H incubation layer was shown to impair with the charge carrier transport [36, 146]. Here thin incubation layers for the OPM-material deposited at high deposition rates were observed. Therefore a disturbance of the charge carrier transport due to an a-Si:H incubation layer is not expected. A detailed discussion of the implications of the structural properties at the pi-interface on the device performance of thin-film solar cells is presented in Chapter 6.

Evolution of mechanical stress for varied deposition power and deposition rate

Evaluating a series of Raman spectra with respect to a frequency shift of the TO phonon mode is challenging since several effects may interfere. Effects which can lead to a frequency shift of the TO phonon mode are: 1. Laser induced crystallization, 2. local heating of the crystal lattice, 3. a variation in crystal grain size, and 4. the presence of compressive or tensile stress [171]. Effects 1 and 2 can be excluded for the measurement setup used here. The measurement routine was equally applied to all samples. None showed an indication for Laser induced crystallization. The choice of short acquisition times ensured the absence of local heating of the crystal lattice.
A shift of the TO phonon mode due to a decreasing crystal size is only observed for a grain size below $15\,nm$. The frequency shift is gradual for a grain size of more than $12\,nm$ and is significant for a grain size below $12\,nm$[172, 173]. Therefore the shift of the TO phonon mode observed here can exclusively attributed to mechanical stress for deposition powers below $400\,W$, since, for those samples a grain size of more than $15\,nm$ is observed (see Figure 5.9). The interpretation of the measured values for deposition powers of $400\,W$ and beyond have to be taken with care. A decrease in grain size of $3\,nm$ can lead to a shift of the TO phonon mode of $1\,cm^{-1}$. For the deposition power of $600\,W$ a grain size of $12\,nm$ is observed. Therefore the shift of the TO phonon mode may be amplified by an additional shift due to a reduced grain size. For samples of set 1 the variation in grain size is not expected to be as pronounced as for the samples of set 2 due to the overall higher Raman intensity ratio. Therefore a shift of the TO phonon mode due to a significant variation in grain size is not expected for the samples of set 1.
The in-plane mechanical stress σ_s in MPa can be deduced from Raman spectra through,

$$\sigma_s = -250\,\Delta\nu \tag{5.1}$$

where $\Delta\nu = \nu_s - \nu_0$ describes the frequency shift with respect to crystalline silicon [174]. The wavenumber of the TO phonon mode of the c-Si reference is described by ν_0, whereas the wavenumber of the TO phonon mode for the investigated sample is given by ν_s. Paillard et al. relate positive values to the presence of tensile stress and negative values to the presence of compressive stress [174]. For the samples investigated here a frequency shift of the TO phonon mode towards lower values was observed with increasing deposition power. Which indicates, according to equation 5.1, the presence of tensile stress.

A possible reason for the tensile stress can be the evolution of gases captured in microvoids due to the high deposition rates [175]. The mechanical stress increases with increasing deposition power which for sample set 2 scales with the deposition rate.

The presence of tensile stress in μc-Si:H can destabilize the lattice structure and lead to weak or strained silicon bonds. Previous studies show a link between mechanical stress and layer properties. Iida et al. showed a reduction in electron and hole mobility with increasing mechanical stress [176]. They suggest a disturbance of carrier transport due to acceptor like interface states on the surface of the growing film [176]. Further studies showed a link between mechanical stress, carrier mobility, and defect density [177, 104]. The occupation of defect states weakens the electric field when a p-i-n junction is formed [178]. This can reflect in a reduction of the open circuit voltage when implementing material deposited at elevated deposition rates as an absorber layer in thin-film solar cells. However, the experimental data presented here are to some extend in conflict with the results presented in Chapter 4 where no increase in defect density was determined by ESR (see Figure 4.8), assuming that the acceptor like states are detectable by ESR.

A broadening of the $FWHM$ of the Gaussian distribution fitted to the TO phonon mode is commonly attributed to a decrease in grain size [179, 180]. This observation endorses the results obtained through XRD measurements, where also a decrease in crystal grain size was observed with increasing deposition power (see Figure 5.9).

Structure investigations performed by TEM imaging

Despite the uncertainty in the quantitative evaluation the TEM images (see Figure 5.11) help to complete the picture. The decrease in incubation layer thickness with increasing deposition power support the measurement results obtained through Raman depth profiles. Furthermore, an increased porosity with increasing deposition power is observed for the samples which consist of the optimal phase mixture material. The porosity, deduced from crack density in the μc-Si:H layer, is further increased with increasing Raman intensity ratio when comparing both samples (set 1 and 2) deposited at a deposition power of $400\,W$. These findings are in line with the results obtained by IR spectroscopy

where an increased tendency for oxygen uptake is observed with increasing deposition power and with increasing Raman intensity ratio for constant deposition powers. The pronounced evolution of cracks in the μc-Si:H material with increasing deposition rate can induce a decrease in open circuit voltage when implementing materials deposited at elevated growth rates as the absorber layer in thin-film solar cells [181, 182].
The *XRD* measurements show a decrease in crystal grain size with increasing deposition power. The decrease in grain size may possibly attributed to a geometrical restriction by the width of the crystal columns. These are observed to decrease with increasing deposition power (Figures 5.11a to c).

5.8 Conclusion

The study presented in this chapter set out with the aim to comprehensively show the implications of elevated deposition rates for μc-Si:H. For layers of high (1) and medium (2) crystallinity the μc-Si:H films were investigated with respect to their microstructure, oxygen uptake after storage including possible diffusion path, crystallinity measurements along the growth axis, investigations on the mechanical stress, and on the size variations of crystal columns and crystal grains. The material of medium Raman intensity ratio was considered suitable for solar cell application based on an empirical figure-of-merit evaluation in Chapter 4. The changes in the oxygen content, monitored by *IR* spectroscopy over a period of up to 180 days after deposition, depend on the deposition rate and Raman intensity ratio of the μc-Si:H layers.
The results of *SIMS* measurements and reduction in the oxygen content after a *HF* etching step suggest that the oxygen uptake is likely to occur via diffusion along open void or grain boundary structure. Although a denser structure can be concluded for the *OPM*-material with medium Raman intensity ratio, this material still suffered from a considerable amount of oxygen uptake which is supposed to affect the performance of opto-electronic devices. Further variations in film microstructure observed here are an increased density of cracks as well as an increase in tensile stress with increasing deposition rate. The latter one is known to induce acceptor like defect states and lead to a reduction in charge carrier mobility [176]. Both effects can lead to a reduction in open circuit voltage when implementing μc-Si:H layers fabricated at high growth rates as an absorber layer in thin-film solar cells [178, 181, 182]. The influence of the increase in deposition rate for the intrinsic absorber layer on the device physics of μc-Si:H thin-film single junction solar cells is presented in the following chapter.
Further variations in microstructure are a decreased grain size and a decrease of the integrated intensity ratio I_{220}/I_{110} deduced from *XRD* measurements in *BB* geometry with increasing deposition rate. Although the necessity of a specific value for the inte-

grated intensity ratio is not expected for the development of high quality thin-film solar cells [168] the results presented here show that the microstructure of the μc-Si:H layers is affected by a variation deposition rate.

The major finding of the study presented in this chapter is that the presently applied criteria to rate material as device grade shown in Chapter 4 are not sufficient and need extension of parameters describing the microstructure of the material.

Finally, it is of course not straightforward to relate the susceptibility of oxygen uptake or variation in the material microstructure to a decrease in device performance since solar cells are often characterized shortly after their deposition within a time frame where e. g. oxygen uptake does not occur or is not detectable. One has to keep in mind that already concentration of oxygen below the detection limit of infrared spectroscopy in the range of $< 10^{19}\,cm^{-3}$ can be detrimental for device performance.

Hence, studies are needed to distinguish conclusively if the changes in the microstructure of the film or effects related to the processing of thin-film solar cells, like damage of interface layers, with increasing deposition rate are responsible for the final device performance. With the findings of the study presented in this chapter one can conclude that even for the material classified as "device grade" based on the established definitions in literature, changes in microstructure occur which most probably affects the device performance and enhance the tendency of these layers to take up oxygen.

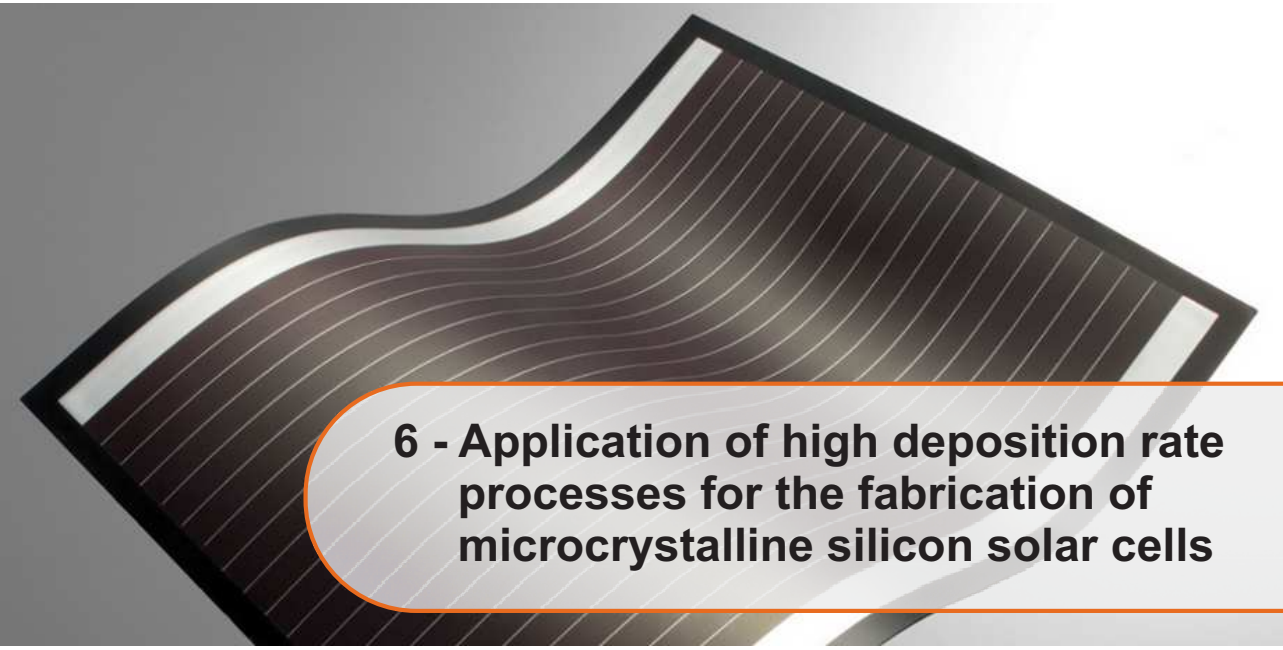

6 - Application of high deposition rate processes for the fabrication of microcrystalline silicon solar cells

In this chapter the results of a study investigating the effects of integrating intrinsic μc-Si:H deposited at high deposition rates as absorber layer in single junction solar cells on the device performance are presented. The thin-film solar cells were investigated with respect to their photovoltaic parameters. Finally, results obtained through monte carlo simulations on the impact of ions are presented.

6.1 Introduction

In the present chapter the effects of an increase in deposition rate on the performance of μc-Si:H thin-film single junction solar cells is presented. The aim of this study is to investigate μc-Si:H in thin-film solar cells. The results obtained during the studies presented in chapter 4 and chapter 5 served as a basis for the subsequent research.
For the device fabrication commercially available Corning Eagle 2000 glass served as substrate. As front contact $ZnO:Al$ was applied by magnetron sputtering. The silicon layers were deposited by *PECVD* in p-i-n sequence with the clustertool deposition system (see chapter 3.1). The fabrication of the thin-film solar cells was terminated by the application of a layer of Ag. The process parameters for the $ZnO:Al$, for the μc-Si:H p-type layer, and for the a-Si:H n-type layer remained unchanged throughout all series. The deposition rate for the intrinsic absorber layer was modified by a variation in deposition power, silane concentration, and deposition pressure. The deposition time for the intrinsic absorber layer was adapted according to the deposition rate in order to achieve the same thickness of the absorber layer for all devices of 1 μm.
Various sample series have been investigated. For the deposition of the intrinsic absorber layer pressure regimes at 3 hPa and at 5 hPa were used. The process parameters for

name	*SC* [%]	*P* [*W*]	*d* [*mm*]	*p* [*hPa*]	buffer layer thickness [*nm*]	buffer processing technique	symbol
sample A	5.2	20	11	1	0	–	
sample B	5.2	20	11	1	120	*HWCVD*	
series C	2.0 - 8.3	50-600	10	5	0	–	
series D	2.0 - 8.3	50-600	10	5	120	*HWCVD*	
series E	2.0-5.2	50-200	10	5	120	*PECVD*	
series F	2.9-3.8	50-200	10	3	0	–	
series G	2.9-3.8	50-200	10	3	120	*HWCVD*	
series H	5.2	50	10	5	0 - 750	*PECVD*	
series I	2.9	50	10	3	0 - 200	*PECVD*	

Table 6.1: Summary of investigated deposition parameters. The deposition parameters are abbreviated as follows: silane concentration *SC*, deposition power *P*, electrode distance *d*, deposition pressure *p*. The buffer layer thickness for each sample series is given as well as the fabrication technique for the buffer layer.

the intrinsic absorber layer leading to *OPM*-material summarized in table 6.1 for each sample series.

Furthermore the application of buffer layers between p-type and intrinsic layer either fabricated by *HWCVD* or *PECVD* has been analyzed. The implementation of a buffer layer enables to investigate to which extend the device performance is governed by the quality of the intrinsic absorber layer or if an impairment of the pi-interface affects the device performance. Possible sources for an impairment of the pi-interface induced by elevated growth rates are structural inhomogeneities, altered nucleation conditions, or damage induced by ion bombardment. The buffer layer will be referred to as i_1-layer. Consequently, the second intrinsic absorber layer will be referred to as i_2-layer. Figure 6.1 shows a schematic sketch of the investigated solar cell design, in (a) without and in (b) with buffer layer.

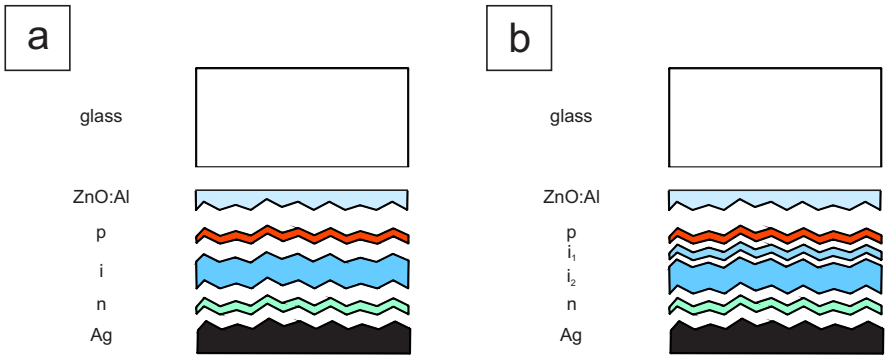

Figure 6.1: Sketch of the investigated solar cell design without (a) and with the application of a buffer layer (b). In (b) the buffer layer is described as i_1-layer, the intrinsic absorber layer as i_2-layer.

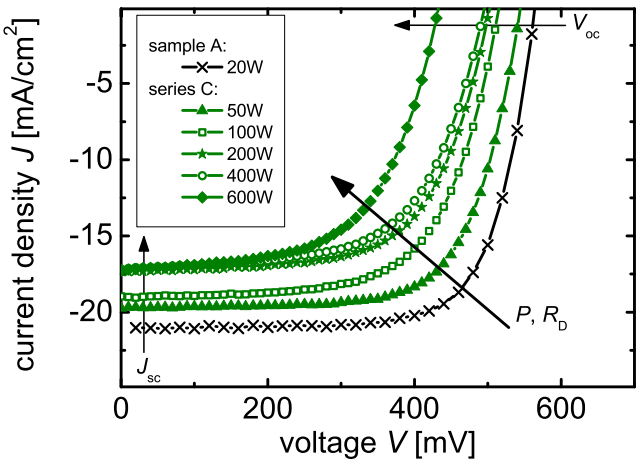

Figure 6.2: Current-voltage characteristic for single junction solar cells. The deposition rate of the intrinsic absorber layer was increased by a variation of the deposition power and the silane concentration (series C). The increase of the deposition rate is indicated by an arrow. As a reference the current-voltage characteristic of a high quality solar cell deposited at low deposition rates (deposition power of $20\,W$) is shown (sample A).

6.2 Increasing the deposition rate of the intrinsic absorber layer of μc-Si:H thin-film single junction solar cells

Figure 6.2 shows the current-voltage characteristic for the single junction solar cells where the deposition power for the intrinsic absorber layer was varied between $50\,W$ and $600\,W$ (series C). The current-voltage characteristic of a high quality solar cell with the intrinsic absorber layer fabricated at a deposition power of $20\,W$ is shown as a reference (sample A). The deposition rate for the absorber layer increases from $0.2\,nm/s$ for the reference sample to $2.7\,nm/s$ for the sample where the deposition power was set to $600\,W$. With increasing deposition rate the open-circuit voltage decreases gradually from $564\,mV$ to $443\,mV$. The short-circuit current density decreases at the same time from $21\,mA/cm^2$ to $17.3\,mA/cm^2$.

Figure 6.3 shows the photovoltaic parameters of the same sample series (sample A and series C) as shown in figure 6.2 as a function of the deposition power of the intrinsic absorber layer. The conversion efficiency decreases from 8.6% for a deposition power of $20\,W$ to 4.5% for a deposition power of $600\,W$. The strongest decrease is observed for an increase in deposition power from $20\,W$ to $200\,W$. With increasing deposition

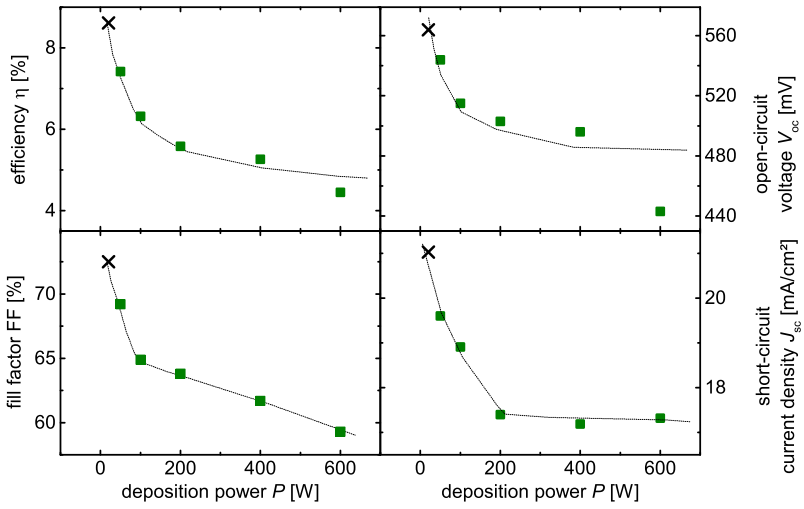

Figure 6.3: Photovoltaic parameters (efficiency η, fill factor FF, open-circuit voltage V_{oc}, and short-circuit current density J_{sc}) as a function of the deposition power used to deposit the intrinsic absorber layer.

power from $20\,W$ to $600\,W$ the open-circuit voltage decreases from $564\,mV$ to $443\,mV$. The fill factor decreases from 72.5% to 59% while increasing the deposition power from $20\,W$ to $600\,W$. The short-circuit current density decreases from $21.0\,mA/cm^2$ for a deposition power of $20\,W$ to $17.3\,mA/cm^2$ for a deposition power of $600\,W$. The strongest decrease is again observed for deposition powers up to $200\,W$. In summary, all photovoltaic parameters decrease with increasing deposition power. Since the deposition rate increases linearly with increasing deposition power for the OPM-material (see chapter 4) one can also say that all photovoltaic parameters decrease with increasing deposition rate.

Figure 6.4 shows the TEM images of two μc-Si:H solar cells. Figure 6.4a and c show the TEM images obtained for a solar cell with an intrinsic absorber layer deposited at $20\,W$. Figure 6.4 b and d show TEM images of a solar cell where the intrinsic absorber layer was deposited at $200\,W$. Figure 6.4a and b show images obtained at lower magnification, while figure 6.4c and d show images obtained at high magnification.

In figure 6.4a and b one can distinguish between the glass substrate, the textured $ZnO:Al$, and the silicon layer stack. For both samples it appears that the μc-Si:H layer features columnar grains. From figure 6.4a and b it is evident that the nucleation of these columnar grains takes place on the textured $ZnO:Al$ substrates. Figure 6.4c and d show a zoom-in of the silicon layer stack. For the sample where the intrinsic absorber layer was fabricated at a deposition power of $20\,W$ (figure 6.4c) one can see a crystal grain which nucleation center appears to be at the spike of the $ZnO:Al$ substrate. This grain shows conical structure close to the substrate/film interface and seems to extend almost through the whole layer. For the sample where the intrinsic absorber layer was fabricated at a deposition power of $200\,W$ (figure 6.4d) smaller crystal grains are observed, compared to the sample shown in figure 6.4c, possibly leading to an increase in void density. However, from the images displayed here it would not be reasonable to comment on the void density.

From figure 6.4a and b it is not possible to see a drastic difference of the nucleation at the substrate film interface. In particular for both samples the presence of an incubation layer is not seen. This is somehow in contrast to the observations drawn from the bight field TEM images taken for the silicon layers (chapter 5, figure 5.11). There an incubation layer with a thickness of approximately $120\,nm$ was observed for the reference sample deposited at a deposition power of $20\,W$. The thickness of this incubation layer was observed to decrease with increasing deposition power. Consistent with the observations obtained from the TEM images of the silicon layers is that for both samples deposited at $20\,W$ a conical growth of the crystal columns is observed. Furthermore for both studies a decrease in column width with increasing deposition power is observed.

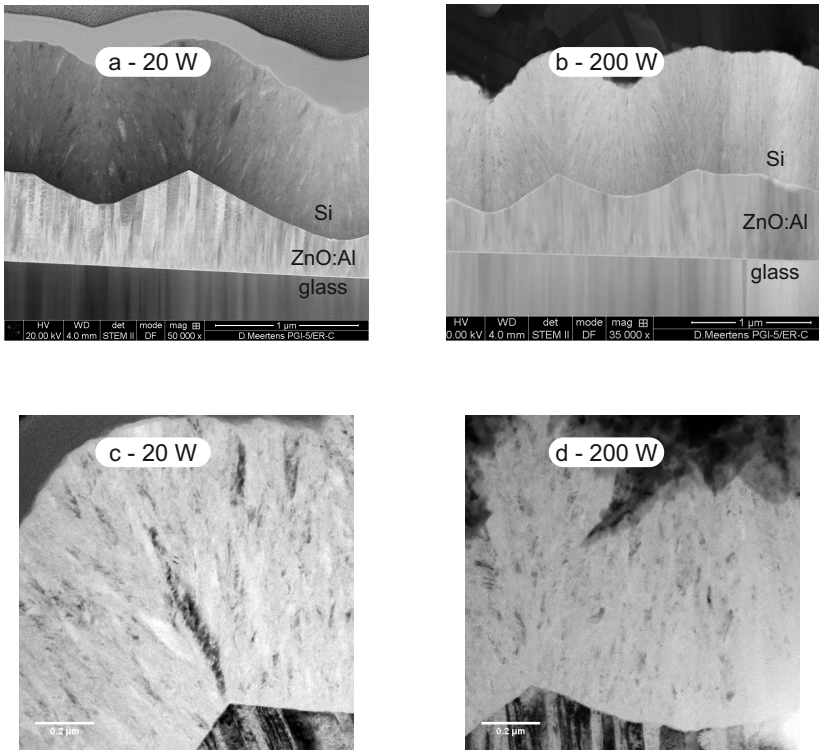

Figure 6.4: *TEM* images of two μc-Si:H single junction solar cells deposited on glass. The first one deposited at a deposition power of $20\,W$ (a, c). The second one deposited at a deposition power of $200\,W$ (b, d). Images showing the cross section of the lamella (a, b) and magnifications of the silicon layer stack (c, d) are shown. All images were taken in bright field modus.

		HWCVD buffer layer	*PECVD* buffer layer
substrate temperature T_{sub}	$[°C]$	150	200
silane concentration SC	$[\%]$	2	5.2
deposition power P	$[W]$	–	20
electrode distance d	$[mm]$	40	11
deposition pressure p	$[hPa]$	0.1	1
wire temperature T_{wire}	$[°C]$	1500	–
wire current I_{wire}	$[A]$	30	–

Table 6.2: Summary of the processing parameters of the applied buffer layers.

6.3 Application of buffer layers to μc-Si:H single junction solar cells

The application of buffer layers enables to investigate if the mediocre device performance of the solar cells shown in the preceding section is related to inferior material quality of the μc-Si:H absorber layer or due to a disturbance of the pi-interface. The buffer layers were either deposited by *HWCVD* or *PECVD*. Processing details can be found in table 6.2. To distinguish between the buffer layers deposited by *HWCVD* and *PECVD* the buffer layers will be referred to as *HWCVD*-buffer or *PECVD*-buffer layer, respectively. According to Schropp no ions are involved during the deposition of silicon layers with the *HWCVD* technique [183]. Therefore a damage of underlying layers due to ion bombardment is unlikely with *HWCVD*. In case of the *PECVD*-buffer layer the deposition rate was low. A damage of the pi-interface due to ion bombardment is not expected since high quality solar cells can be obtained with these deposition conditions as can be seen for sample A. The buffer layers thickness was set to 120 nm independent of the deposition technique. The deposition time for the i_2-layer was shortened accordingly to ensure a final thickness of the intrinsic layer of 1 μm.

6.3.1 The effect of buffer layers on the performance of thin-film solar cells

Figure 6.5 shows the photovoltaic parameters for samples A and B and for series C to G as a function of the deposition rate of the i_2-layer.

Overall the conversion efficiency decreases with increasing deposition rate independent of the applied deposition pressure and independent of the application of a buffer layer. Furthermore, the open-circuit voltage as well as the short-circuit current density and the fill factor decrease with increasing deposition rate. For the reference solar cell where the intrinsic absorber layer was deposited at a deposition rate of 0.2 nm/s the implementation of a *HWCVD*-buffer layer leads to an increase in conversion efficiency of 0.9% on absolute scale (samples A and B). This increase is mainly driven by an increase

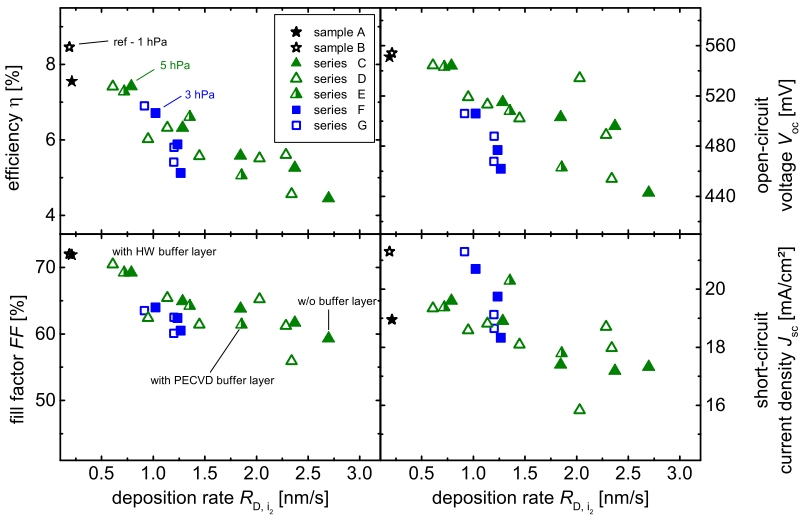

Figure 6.5: Photovoltaic parameters (efficiency η, fill factor FF, open-circuit voltage V_{oc}, and short-circuit current density J_{sc}) as a function of the deposition rate of the i_2-layer. Two pressure regimes at 3 hPa and 5 hPa have been investigated. In addition the application of buffer layers fabricated by $HWCVD$ and $PECVD$ was explored. Experimental data of solar cells deposited at low deposition rates with and without buffer layer are shown as a reference.

in short-circuit current density of 1.3 mA/cm^2 from 19 mA/cm^2 to 21.3 mA/cm^2. The fill factor and the open-circuit voltage are not affected by the implementation of the $HWCVD$-buffer layer.

For the sample series where the intrinsic absorber layer was deposited at a deposition pressure of 5 hPa without any buffer layer being applied (series C) the conversion efficiency decreases from 7.4% to 4.5% for an increase in deposition rate from 0.8 nm/s to 2.7 nm/s. For the same range in deposition rate the open-circuit voltage to decreases from 544 mV to 443 mV, the fill factor from 69% to 59%, and the short-circuit current density from 19.6 mA/cm^2 to 17.3 mA/cm^2.

Applying a $HWCVD$-buffer layer (series D) shows similar trends with increasing deposition rate as the sample series without buffer layer (series C). The conversion efficiency decreases from 7.4% to 4.6% with an increase in deposition rate from 0.6 nm/s to 2.3 nm/s of the μc-Si:H i_2-layer. For the same interval of deposition rate the open-circuit voltage decreases from 544 mV to 454 mV, the fill factor from 70% to 56%, and

the short-circuit current density from 19.3 mA/cm^2 to 18 mA/cm^2.

For the sample series where the *PECVD*-buffer layer was implemented (series E), the conversion efficiency decreases from 7.3% for a deposition rate of 0.7 nm/s to 5.1% for a deposition rate of 1.9 nm/s. At the same time the open-circuit voltage decreases from 543 mV to 463 mV, the fill factor from 69% to 61%, and the short-circuit current density from 19.4 mA/cm^2 to 17.8 mA/cm^2.

Comparing the photovoltaic parameters for the sample series without buffer layer, with a *HWCVD*-buffer layer, and with the *PECVD*-buffer layer (series C to E) similar values for a specific value of deposition rate are observed.

For a second pressure regime at 3 hPa μc-Si:H thin-film solar cells with a varied deposition rate for the intrinsic absorber layer with and without buffer layer have been fabricated. For the series without buffer layer (series F) the conversion efficiency decreases from 6.7% for a deposition rate of 1.0 nm/s to 5.1% for a deposition rate of 1.3 nm/s. For the same range in deposition rate the open-circuit voltage decreases from 506 mV to 462 mV, the fill factor from 64% to 60.5%, and the short-circuit current density from 20.7 mA/cm^2 to 18.3 mA/cm^2.

For the sample series wherein the *HWCVD*-buffer layer was applied (series G) the conversion efficiency decreases from 6.9% to 5.4% for an increase in deposition rate of the i_2-layer from 0.9 nm/s to 1.2 nm/s. At the same time the open-circuit voltage decreases from 506 mV to 468 mV, the fill factor from 63.5% to 60.1%, and the short-circuit current density from 21.3 mA/cm^2 to 18.7 mA/cm^2.

When comparing the photovoltaic parameters of the solar cells fabricated with and without buffer layer for the pressure regime of 3 hPa the values are observed to be similar.

Figure 6.6 shows the short-circuit current density measured under blue- (a) and red-light (b) both as a function of the deposition rate of the intrinsic absorber layer.

For the reference solar cell an increase in short-circuit current density measured under blue light $J_{sc,blue}$ of 0.35 mA/cm^2 is observed by the introduction of the *HWCVD*-buffer layer. For the sample series where the intrinsic absorber layer was fabricated at a deposition pressure of 5 hPa without any buffer layer (series C) the $J_{sc,blue}$ shows significant scatter. However, at a deposition rate of 2.7 nm/s the $J_{sc,blue}$ is observed at 3.27 mA/cm^2 which is even higher than the values observed for low deposition rates. By the application of the *HWCVD*-buffer layer for the same pressure regime (series D) the $J_{sc,blue}$ is constant at approximately 3.1 mA/cm^2 independent of the deposition rate. For the sample series of the same pressure regime with the *PECVD*-buffer layer (series E) the $J_{sc,blue}$ is constant at 3.0 mA/cm^2 for a deposition rate below 1.4 nm/s. At a deposition rate of 1.9 nm/s the $J_{sc,blue}$ decreases to 2.7 mA/cm^2.

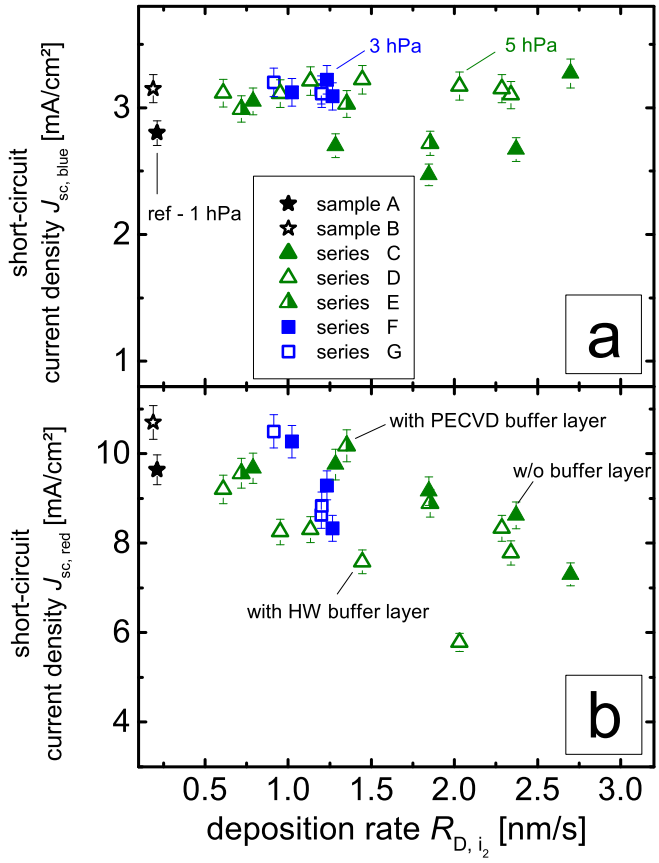

Figure 6.6: Short-circuit current density measured under blue light (bandpass centered around 480 *nm*) (a) and red light (low-pass filter with a cut-off wavelength of 590 *nm*) (b) as a function of the deposition rate of the i_2-layer. Two pressure regimes at 3 *hPa* and 5 *hPa* have been investigated. In addition the application of buffer layers fabricated by *HWCVD* or *PECVD* was explored. Experimental data of solar cells deposited at low deposition rates with and without buffer layer are shown as a reference.

For the sample series where the intrinsic absorber layer was deposited at a deposition pressure of 3 hPa the $J_{sc,blue}$ is constant around 3.1 mA/cm^2 independent of the deposition rate and independent of the application of a buffer layer (series F and G).
For the reference solar cell an increase in short-circuit current density measured under red light $J_{sc,red}$ of 1.1 mA/cm^2 is observed with the introduction of the $HWCVD$-buffer layer. For the sample series where the intrinsic absorber layer was fabricated at a deposition pressure of 5 hPa without a buffer layer being applied (series C), the $J_{sc,red}$ decreases from 9.7 mA/cm^2 to 7.3 mA/cm^2 with an increase in deposition rate from 0.8 nm/s to 2.7 nm/s. For the sample series deposited at the same pressure regime with the implementation of the $HWCVD$-buffer (series D) a reduction in $J_{sc,red}$ from 9.2 mA/cm^2 to 7.8 mA/cm^2 with an increase in deposition rate from 0.6 nm/s to 2.3 nm/s occurs. For the sample series with the $PECVD$-buffer layer a reduction in $J_{sc,red}$ from 9.6 mA/cm^2 to 8.9 mA/cm^2 is observed for an increase in deposition rate from 0.7 nm/s to 1.9 nm/s.
For the sample series where the pressure regime of 3 hPa was used for the deposition of the intrinsic absorber layer a reduction in $J_{sc,red}$ from 10.3 mA/cm^2 to 8.3 mA/cm^2 for an increase in deposition rate from 1.0 nm/s to 1.3 nm/s is observed for the sample series without buffer layer (series F). For the same pressure regime with the $HWCVD$-buffer layer (series G) a reduction in $J_{sc,red}$ from 10.5 mA/cm^2 to 8.6 mA/cm^2 with an increase in deposition rate from 0.9 nm/s to 1.2 nm/s is observed.
Overall a decrease in $J_{sc,red}$ with increasing deposition rate is observed. Despite the considerable scatter the general trends of a decrease in $J_{sc,red}$ with increasing deposition rate is observed independent of the fact if a buffer layer is applied or not. The $J_{sc,blue}$ is neither observed to be influenced by an increase in deposition rate nor by the application of a buffer layer.

6.3.2 Varying the thickness of the buffer layer for thin-film solar cells

The buffer layer thickness for series H was varied between 0 nm and 750 nm. For series I the buffer layer thickness was varied between 0 nm and 200 nm. Further processing details for both sample series can be found in table 6.1. The buffer layer for both series was fabricated by $PECVD$. The experimental data presented in the previous section showed similar photovoltaic parameters for the solar cells with a $HWCVD$-buffer layer compared to those with the $PECVD$-buffer layer. The $PECVD$ technique for the buffer layer deposition was used due to a shorter total processing time.

The aim of this experiment was to investigate which thickness of buffer layer is necessary to achieve a similar device performance as for the reference process. These investigations allowed to study to which extend the application of an intrinsic absorber layer fabricated at high growth rates can be detrimental for device performance.

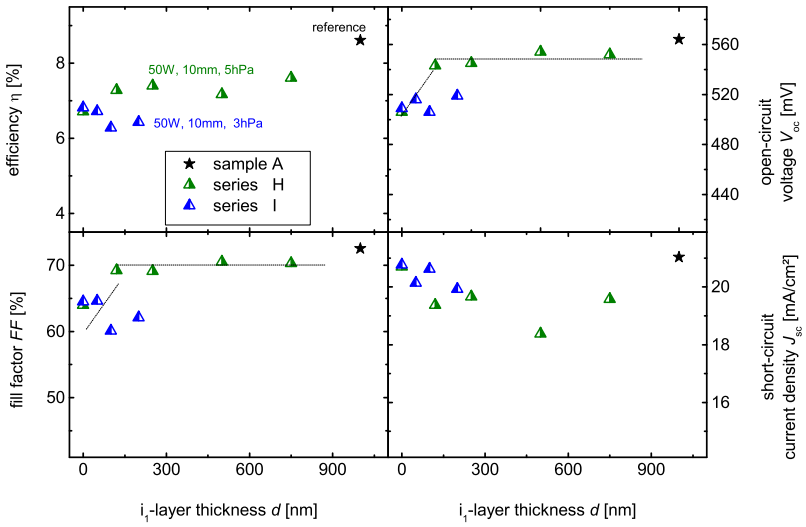

Figure 6.7: Photovoltaic parameters (efficiency η, fill factor FF, open-circuit voltage V_{oc}, and short-circuit current density J_{sc}) as a function of the thickness of the buffer layer. For this study the buffer layer was fabricated by *PECVD*. Two pressure regimes at 3 *hPa* and 5 *hPa* have been investigated.

The deposition time of the i_2-layer was adjusted according to the thickness of the i_1-layer in order to achieve a similar thickness of the intrinsic absorber layer for all devices of 1 μm. The deposition parameters of the buffer layer applied here correspond to the reference process for the processing of intrinsic absorber layers which yield high quality solar cells at low deposition rates.

Figure 6.7 shows the photovoltaic parameters of two sample series (series H and I) as a function of the buffer layer thickness. The thin-film solar cell presented in figure 6.7 with an i_1-layer thickness of 1 μm corresponds to a reference solar cell. For the sample series where the deposition pressure was set to 5 *hPa* for the i_2-layer deposition (series H) the conversion efficiency increases from 6.7% for the sample without buffer layer to 7.6% for a buffer layer thickness of 750 *nm*. For the same range in buffer layer thickness the open-circuit voltage increases from 506 *mV* to 552 *mV*, the fill factor from 64% to 70.3%, the short-circuit current density decreases from 20.7 mA/cm^2 to 19.6 mA/cm^2. For the sample series where the i_2-layer was deposited at a deposition pressure of 3 *hPa* (series I) the variation conversion efficiency is less pronounced than for the samples

of series H. For the sample with out buffer layer a conversion efficiency of 6.8% is observed. For a buffer layer thickness of 200 nm a conversion efficiency of 6.4% is seen. For the same variation in buffer layer thickness the open-circuit voltage increases from 509 mV to 519 mV, the fill factor decreases from 64.5% to 62.1%, and the short-circuit current density decreases from 20.8 mA/cm^2 to 20.0 mA/cm^2.

Figure 6.8 shows the short-circuit current density measured under the blue- (a) and red-light (b) both as a function of the buffer layer thickness for the samples of series H and I. For the samples where the i_2-layer was deposited at a deposition pressure of 5 hPa (series H) the $J_{sc,blue}$ is observed between 3.1 mA/cm^2 and 2.8 mA/cm^2. The results do not indicate a clear trend of the $J_{sc,blue}$. The $J_{sc,blue}$ for the sample series where the i_2-layer was deposited at 3 hPa stays close to 2.9 mA/cm^2 independent of the buffer layer thickness (series I).

The $J_{sc,red}$ is observed to decrease for both sample series with increasing buffer layer thickness. For the sample series where the intrinsic absorber layer was deposited at a deposition pressure of 5 hPa (series H) the $J_{sc,red}$ decreases from 10.3 mA/cm^2 to 9.4 mA/cm^2 by an increase in buffer layer thickness from 0 nm to 750 nm. Despite significant scatter it appears that the $J_{sc,red}$ for the sample series where the intrinsic absorber layer was deposited at a deposition pressure of 3 hPa (series I) decreases from 10.7 mA/cm^2 to 10.0 mA/cm^2 for an increase in buffer layer thickness from 0 nm to 200 nm.

The results of this experiment indicate that a decrease in device performance can not exclusively be attributed either to a decrease in absorber layer material quality nor to an impairment of the pi-interface. In contrary the results suggest that a combination of both accounts for the decrease in device performance.

6.3.3 About the challenge to keep the deposition rate high when implementing buffer layers

When targeting high deposition rates the application of a buffer layer deposited at low deposition rates can be counterproductive since the effective deposition rate of the whole intrinsic absorber layer decreases with increasing buffer layer thickness. Figure 6.9 shows the effective deposition rate of a stack of two intrinsic absorber layers as a function of the thickness of the buffer layer. The effective deposition rate is calculated by

$$R_{D,eff} = \frac{d_{total}}{t_{total}} = \frac{d_{total}}{\frac{d_{i1}}{R_{D,i1}} + \frac{d_{i2}}{R_{D,i2}}}, \tag{6.1}$$

where d_{total} is the total layer thickness which was set to 1 μm. The total deposition time t_{total} is the sum of the deposition time of the buffer layer and the second intrinsic layer.

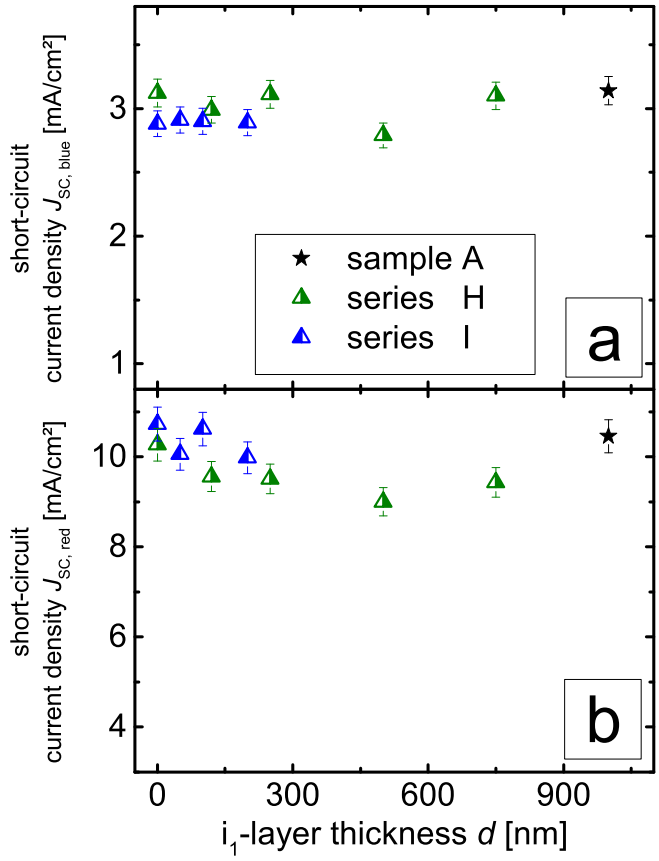

Figure 6.8: Short-circuit current density measured with blue light (a) and red light (b) as a function of the thickness of the buffer layer. For this study the buffer layer was fabricated by *PECVD*. Two pressure regimes at 3 *hPa* and 5 *hPa* have been investigated.

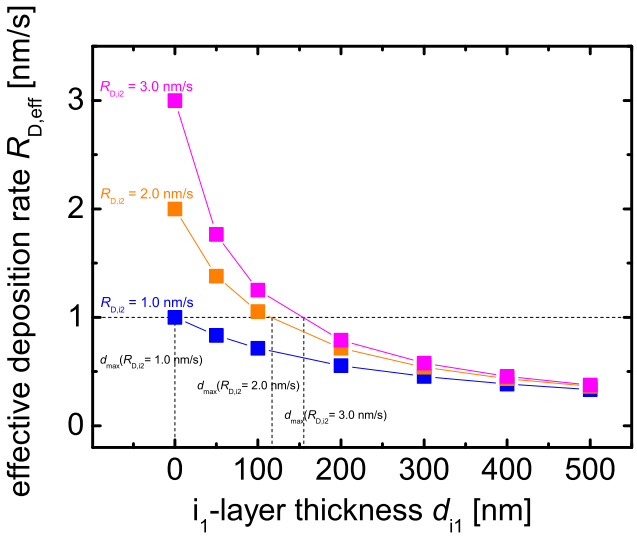

Figure 6.9: Effective deposition rate as a function of the thickness of the first layer. The effective deposition rate is calculated according to equation 6.1. The total thickness of the layer stack was set to $1\,\mu m$, the deposition rate of the i_1-layer was set to $0.2\,nm/s$. The deposition rate of the i_2-layer was varied between $1\,nm/s$, $2\,nm/s$, and $3\,nm/s$. The maximum i_1-layer thickness for a minimal effective deposition rate of $1\,nm/s$ is indicated.

The deposition time for the i_1-layer is calculated by the variable thickness d_{i1} and a set deposition rate $R_{D,i1}$ of $0.2\,nm/s$. The deposition time for the i_2-layer is calculated by the variable thickness d_{i2} ($1\,\mu m - d_{i1}$) and the variable deposition rate $R_{D,i2}$.
The effective deposition rate is calculated for various deposition rates $R_{D,i2}$ of $1\,nm/s$, $2\,nm/s$, and $3\,nm/s$ of the i_2-layer. With increasing i_1-layer thickness the effective deposition rate decreases independent of the deposition rate of the i_2-layer. Furthermore the effective deposition rate converges towards a value of approximately $0.33\,nm/s$ independent of the deposition rate of the i_2-layer.
Figure 6.9 allows to calculate the maximum thickness of the i_1-layer for a specific value of effective deposition rate. Here the procedure is exemplary shown for a effective deposition rate of $1\,nm/s$. For a deposition rate of the i_2-layer of $1\,nm/s$ the application of a buffer layer of any thickness leads to an effective deposition rate below $1\,nm/s$. For a deposition rate of the i_2-layer of $2\,nm/s$ the maximal buffer layer thickness is $117\,nm$ if the effective deposition rate should be equal or beyond to $1.0\,nm/s$. Accordingly

the maximal buffer layer thickness for a deposition rate of the i_2-layer of $3\,nm/s$ is calculated to $155\,nm$. In order to take advantage of the high deposition rates for the i_2-layer the thickness of the i_1-layer should be limited.

6.4 Simulation of the ion impact

The experimental data shown in the preceding sections suggest that along with a decrease in material quality a deterioration of the pi-interface is the reason for the reduced device performance when applying intrinsic absorber layers deposited at high deposition rates. The impairment of the pi-interface induced by high deposition rates may originate from ion bombardment, a variation of the nucleation conditions, or form structural inhomogeneities at the substrate/film interface. To further elucidate the origin of the impairment of the pi-interface simulations on the impact of ions on a silicon target have been performed.

6.4.1 Approach

The calculations of the stopping and range of ions in matter were performed with the *SRIM* software package. The software suite is openly available through the *SRIM*-website [184]. The program was introduced in 1985 by Ziegler et al. [185]. Since it was continuously improved with major updates approximately every six years [186, 187]. The *SRIM* database comprises 28000 stopping values and over 500 diagrams document the accuracy between simulation and experimental data [184]. A detailed introduction to the *SRIM* software suite and the theory of stopping and range of ions in matter can be found in the book of Ziegler et al. [185].

The software suite uses quantum mechanical calculations to describe ion-atom collisions including shell effects. The ions with their specific mass are assumed to move towards the stationary target. The stopping power describes the reduction in energy per unit distance. The ion trajectories in the target are calculated through the consideration of multiple ion-atom collisions. Each trajectory starts with a specific energy, direction, and position. The ion energy is reduced with each collision event. The collision partner atom absorbs energy while the ion changes its direction. The ion trajectory between two collision events is assumed to be a straight line. For each collision event nuclear and electronic energy reductions are considered. The trajectory is calculated until the ion energy vanishes through ion-atom collisions or when the ions transmits through the target. The trajectories elongation for each ion is limited by the conservation of momentum and energy of the whole system. The atoms in the target layer are assumed to be randomly distributed such that the lattice structure does not affect the stopping and the range of the ions in the target. The *SRIM* software package enables to calculate the

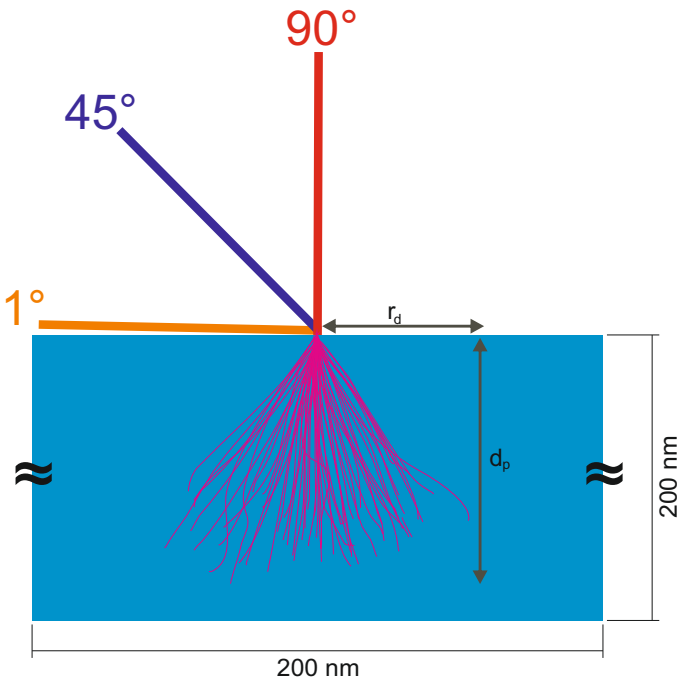

Figure 6.10: Schematic of the structure of the monte carlo simulation on the stopping and range of ions in matter. For each incident angle of 1°, 45°, and 90° with respect to the substrate surface the energy of the bombarding ions was varied between 10 eV and 200 eV. As species of the bombarding ions silicon ions have been chosen. A silicon layer with the dimension of 200 nm x 200 nm x 200 nm was assumed as target. The simulation enables to calculate the penetration depth d_p and the radial distribution r_d of the ions in the target.

final distribution of the ions in the target. Furthermore, excitation of atoms, sputtering yield, lattice displacements, and phonon production can be calculated.

Figure 6.10 shows a schematic drawing of the setup used for the calculation of the penetration depth and radial distribution of ions in a silicon substrate. The ion trajectories schematically shown in figure 6.10 are typical for an incident angle of 90°. Here the software version *SRIM* 2008.4 was used for the final ion distribution.

The calculations were performed for incident angles of 1°, 45°, and 90° with respect to the substrate surface. The energy of the bombarding silicon ions was varied between 10 eV and 200 eV. As target a layer of silicon with dimensions of 200 nm x 200 nm x 200 nm was assumed. For each set of input parameters the penetration depth d_p and the radial distribution r_d was calculated for 30000 ion trajectories. Typical values for the

energy of the bombarding ions range between $10\,eV$ and $100\,eV$ for the deposition of thin silicon films by *PECVD* [27]. Recently Bronneberg et al. suggested the ion energy for *HPD* process regimes to be at most at $19\,eV$. This estimation is based on measurements with a capacitive probe in the pressure range between $2\,hPa$ and $20\,hPa$ [188]. It is important to note that the measurements were performed for a hydrogen glow discharge at a gas pressure of $1\,hPa$ and an excitation frequency of $13.56\,MHz$. The energy of the bombarding ions is known to decrease with increasing gas pressure and increasing excitation frequency.

6.4.2 Penetration depth and radial distribution of ions with varying incident energy in silicon

Figure 6.11 shows the maximal penetration depth d_p (a) and the maximal radial distribution r_d (b) of ions in a silicon target both as a function of the energy of the impinging ions. The calculations have been performed for an incident angle of 1°, 45°, and 90° with respect to the substrate surface.

The penetration depth increases with increasing energy of the bombarding ions for all angles of incidence. For a specific energy value the penetration depth is observed to be highest for an angle of incidence of 90° and lowest for an angle of incidence of 1°. The maximal penetration depth is $1.1\,nm$ for an ion energy of $100\,eV$ for an incident angle of 90°. Considering the recently published maximal value of impinging ions of $19\,eV$ the penetration depth accounts less than $0.6\,nm$.

The radial distribution of the ions in the target increases with increasing energy of the bombarding ions. The increase in radial distribution is independent of the angle of incidence. The radial distribution is highest for an angle of incidence of 1° and lowest for an angle of incidence of 90°. The highest value for the radial distribution is $1.2\,nm$ for an ion energy of $100\,eV$ for an incident angle of 1°. Again, when considering a maximal value for the ion energy $19\,eV$ the radial distribution is observed to be less than $0.7\,nm$. The results obtained through the calculations of the ion impact in matter show that a deterioration of the pi-interface due to ion bombardment is unlikely.

6.5 Discussion

The aim of the study presented in this chapter was to investigate the effects on photovoltaic parameters of μc-Si:H solar cells when incorporating intrinsic absorber layer deposited at elevated growth rates. The study presented in this chapter based on the results of the preceding studies presented in chapters 4 and 5. With the established criteria in literature the material obtained at elevated growth rates was considered to be

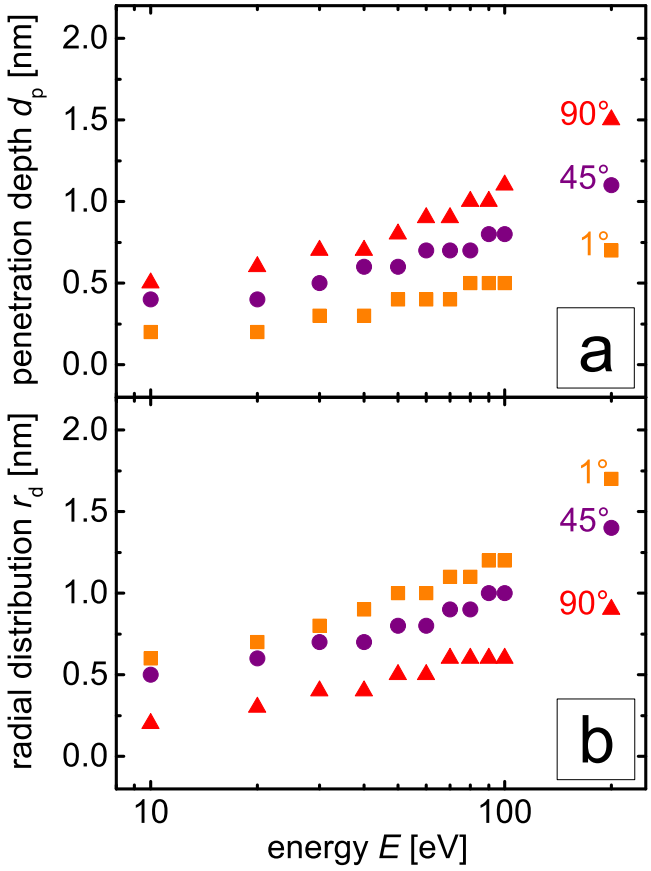

Figure 6.11: Maximal penetration depth d_p (a) and maximal radial distribution (b) of ions as a function of the bombarding energy of these ions. The calculations have been performed for an incident angle of the ions of 1°, 45°, 90° with respect to the substrate surface.

of device grade quality [148, 38]. However the study presented in chapter 5 suggest a considerable change in microstructure and porosity of the μc-Si:H films. The μc-Si:H films show pronounced tensile stress with increasing deposition rate. The presence of tensile stress can reflect in a reduction in open-circuit voltage when incorporating those materials in thin-film solar cells due to a disturbance of the electric field.

All photovoltaic parameters decrease with increasing deposition power (series C, figure 6.3). The decrease in fill factor can be related to inferior material quality of the intrinsic absorber layer with increasing deposition power. The short-circuit current density can phenomenologically be described as the sum of the $J_{sc,red}$ and a multiple of the $J_{sc,blue}$. Therefore a decrease in short-circuit current density can also be attributed to a decrease in $J_{sc,blue}$ induced by a deterioration of the pi-interface.

Implementing buffer layers between p-type and intrinsic absorber layers protects the pi-interface from possible damage induced by the application of high deposition rates. Thus, it enables to investigate if the reduced device performance is due to a deterioration of the pi-interface or due to inferior material quality of the intrinsic absorber layers.

Apart from the reference sample (sample B, figure 6.5) an effect of the buffer layer either fabricated by $HWCVD$ or $PECVD$ is not observed. This is an indication that the reduction in device performance is strongly related to a decrease in absorber layer material quality with increasing deposition rate. This assumption is supported by the results obtained through IV-measurements under blue and red light illumination. Considering the measurement uncertainty, the short-circuit density measured under blue light is neither influenced by an increase in deposition rate nor by an implementation of a buffer layer (see figure 6.6a). A decrease in short-circuit density measured under red light is observed with increasing deposition rate which points to an inferior material quality of the intrinsic absorber layer (see figure 6.6b).

On the other hand, an increase in open-circuit voltage and fill factor is observed with increasing thickness of the $PECVD$-buffer layer (series H and I, figure 6.7). When considering the open-circuit voltage and the fill factor as measures for the material quality of the intrinsic absorber layer the experimental data shown in figure 6.7 allow to draw two conclusions. First, independent of the $PECVD$-buffer layer thickness, neither the open-circuit voltage nor the fill factor of the reference sample were reached by any sample in series I (see figure 6.7). This supports the earlier conclusion that the device performance is limited by the absorber layer material quality. Second, with an increase in the buffer layer thickness up to $120\,nm$ an increase in open-circuit voltage and fill factor is observed. This shows that the device performance is also governed by the conditions of the pi-interface.

Van den Donker and Mai observed the formation of an a-Si:H incubation layer up to a

thickness of 100 nm when applying the HPD regime for the deposition of the intrinsic absorber layer [144, 149]. The presence of the a-Si:H incubation layer was claimed to be responsible for the poor device performance of the solar cells they presented. The formation of the a-Si:H incubation layer was explained by a transient depletion of silane source gas from the discharge zone shortly after the ignition of the glow discharge [144]. Here a pronounced fraction of a-Si:H at the pi-interface is not observed. In contrast TEM investigations performed on solar cells (see figure 6.4) and silicon layers (chapter 5, figure 5.11) point to a high Raman intensity ratio at the pi-interface when applying processes yielding high deposition rates. For the silicon layers (chapter 5, figure 5.11) the incubation layer thickness was observed to decrease with increasing deposition rate. These findings were supported by Raman depth profiles where the Raman intensity ratio was measured along the growth axis. From these measurements (chapter 5, figure 5.7b) one can also see a decrease in incubation layer thickness and an increase in Raman intensity ratio at the substrate/film interface. The fact that for the solar cells presented here no incubation layer is seen in the TEM images (figure 6.4) while for the silicon layers an a-Si:H incubation layer is observed (chapter 5, figure 5.11) is attributed to the use of different substrates. In case of the solar cells the intrinsic μc-Si:H absorber layer was deposited on a highly crystalline p-type layer which is expected to facilitate the nucleation compared to a glass substrate used for the silicon layers [169, 170, 132].
Furthermore an a-Si:H incubation layer is expected to impair the carrier extraction [149]. This should reflect in a reduction of the short-circuit current density measured under blue light, which is not observed here (see figure 6.8a). Conclusions on the detailed variations in Raman intensity ratio along the growth axis can not be given for the solar cells presented in this chapter since the Raman depth profile measurements were not performed.
Apart from the ion bombardment, which will be discussed later, a variation of the nucleation conditions at the pi-interface can be another origin for the impairment of this interface. The formation of a silicon film from a glow discharge process takes place through the adsorption of growth precursors on the surface of the growing film. One condition for the formation of a rigid network is that the growth precursors are able to move on the surface of the growing film until energetically favorable growth sites are found [90]. If the surface diffusion length is drastically reduced the probability for the formation of a defective material is increased. The application of high deposition rates may alter the surface chemistry by an increased precursor flux towards the surface of the growing film. Leading to a reduction in growth precursor diffusion length which may impair the pi-interface through the formation of a low-density network.
In chapter 5 an increase in tensile stress in the μc-Si:H layers was observed with in-

creasing deposition rate. The presence of tensile stress can lead to defect states in the intrinsic absorber layer. These defect states can if occupied in a p-i-n structure affect the electric field distribution which reflects in a reduced open-circuit voltage [178]. Indeed a reduction in open-circuit voltage is observed with increasing deposition rate which fits in the picture. Supporting the findings here Bugnon et al. showed a correlation between conversion efficiency and mechanical stress [189].

For the reference solar cell a positive influence in terms of device performance is observed by the incorporation of the *HWCVD*-buffer layer. The increase in conversion efficiency is mainly driven by an increase in short-circuit current density. An increase in open-circuit voltage like reported in earlier studies performed at the research center in Jülich is not observed [190, 191]. One reason for this discrepancy can be that the installation of the new deposition facilities with a pumping system which reaches pressures in the ultra high vacuum range enables to deposit layers with a higher material purity. A slight oxygen contamination could lead to a defect rich layer. When placed between p-type and intrinsic absorber layer this could lead to an increase in open-circuit voltage which was seen in the earlier studies.

The assumption of an inferior material quality for the intrinsic absorber layer deposited at elevated deposition rates is supported by the *TEM* investigations. With increased growth rate a decrease of the width of the crystal columns is observed, which can lead to an increase in void density. An increased void density and discontinued crystal grains can lead to an enhanced recombination due to an increase in defect density and thus a decrease in short-circuit current density.

Turning the attention to the results obtained through the simulation of impinging ions. The highest penetration depth for an incident angle of 90° is explained by the fact that the bombarding ions do not possess any energy fraction parallel to the substrate surface. For an incident angle of 1° the contribution parallel to the substrate surface is considerable. Therefore the penetration depth shows the lowest value while the radial distribution shows the highest values for an incident angle of 1°. Considering the estimation for the upper limit for the ion energy for *HPD* process regimes of $19\,eV$ [188] the maximal penetration depth is around $0.6\,nm$ while the maximal radial distribution is around $0.7\,nm$. That means that the maximal penetration depth corresponds to five monolayers of silicon atoms. The radial distribution corresponds at most six times the width of one silicon atom. Thus, a strong influence of the ion bombardment on the pi-interface seems unlikely.

Furthermore, serious damage of the pi-interface induced by ion bombardment can be excluded when comparing the upper limit for ion energies for the *HPD* process regime to the threshold values given in literature for the sputtering of silicon, the bulk, and

the surface displacement of silicon atoms. The threshold energy for the sputtering of silicon atoms is given in literature by $50\,eV$ [192]. The threshold energy for the bulk displacement of silicon atoms is calculated to $36\,eV$ while the threshold energy for the surface displacement of silicon was calculated to $16\,eV$ [193]. Thus, the sputtering of silicon atoms and the bulk displacement due to ion bombardment can be excluded. The surface displacement of silicon atoms is possible but not very likely since the energy of $19\,eV$ is regarded as a upper limit and the energy of the bombarding ions decreases with increasing deposition pressure and increasing excitation frequency. Therefore a serious damage of the pi-interface due to ion bombardment is unlikely. The mediocre device performance can be related to inferior material quality of the intrinsic absorber layer deposited at elevated deposition rates altogether with an impairment of the pi-interface due to a variation of the nucleation conditions or to structural inhomogeneities at the substrate/film interface. Amongst others van den Donker showed that tailored processes concentrating on the engineering of the pi-interface can lead to an improved device performance [144]. Future work could investigate dedicated processes for the pi-interface for the deposition conditions described here to overcome the limitations induced by an impairment of the pi-interface. The limitations of the device performance due to an inferior material quality of the intrinsic absorber layer is in some points in contrast to the findings presented in the preceding chapters. The experimental data gained through conductivity (chapter 4, figure 4.7) and *ESR* (chapter 4, figure 4.8) measurements suggest the feasibility to produce *OPM*-material at elevated deposition rates.

6.6 Conclusion

The effects of an increased deposition rate for the intrinsic absorber layer of μc-Si:H solar cells on the device performance was investigated. For an increased deposition rate the device performance decreases which is determined by a decrease of all photovoltaic parameters which is partly in contrast to the expectations raised from the investigations on μc-Si:H layers (see chapter 4). The incorporation of buffer layers either fabricated by *HWCVD* or *PECVD* between the p-type and intrinsic layer allowed to investigate if the reduced device performance at elevated deposition rates is related to a damage of the pi-interface and/or to an inferior material quality of the intrinsic absorber layer. The experimental results presented here showed the device performance to be limited by a combination of both effects. Monte carlo simulations on the ion impact showed that a serious damage of the pi-interface due to ion bombardment is unlikely. As possible sources for an impairment of the pi-interface a variation of the nucleation conditions

and structural inhomogeneities at the substrate/film interface have been discussed.

7 - Microcrystalline silicon absorber layers prepared at high deposition rates for thin-film tandem solar cells

In this chapter the results of a study with the aim to implement intrinsic μc-Si:H layers fabricated at elevated deposition rates as the absorber layer of the bottom solar cell of a-Si:H/μc-Si:H tandem solar cells are presented. The thin-film tandem solar cells are investigated with respect to their photovoltaic parameters, performance upon light induced degradation, and short-circuit current density matching between top and bottom solar cell before and after the light induced degradation. Finally EQE measurements of the multijunction solar cells are presented comparing the as deposited state and the device performance after 1000 h of light induced degradation.

7.1 Introduction

The processes developed during the material study presented in Chapter 4 as well as the results obtained while investigating μc-Si:H single junction solar cells presented in Chapter 6 served as starting point for the study presented in this chapter.

For the device fabrication commercially available glass covered with SnO_2:F (Asahi type VU) was used as substrate. The silicon layers were deposited by $PECVD$ on 10 cm x 10 cm substrates using the clustertool deposition system (see Chapter 3.1). For the a-Si:H top solar cell and the μc-Si:H bottom solar cell the p-i-n deposition sequence was used such that the solar cells were fabricated in superstrate configuration. The top solar cell is formed by a layer stack consisting of p-type a-SiC:H, intrinsic a-Si:H, and n-type μc-Si:H layer. The bottom solar cell is formed by a layer stack of p-type μc-Si:H, intrinsic μc-Si:H, and n-type a-Si:H. A layer sequence of sputtered ZnO:Al/Ag/ZnO:Al served as the back contact and back reflector of the final device. Apart from the deposition conditions of the μc-Si:H absorber layer of the bottom

	p [hPa]	d [mm]	P [W]	SC [%]
reference process	1	11	20	5.2
HPD process 1	3	10	50 - 100	3.4 - 3.9
HPD process 2	5	10	50 - 400	2.4 - 7.0

Table 7.1: Deposition parameters of the μc-Si:H absorber layer for the reference process and the two deposition regimes conducted at elevated deposition pressures. The deposition parameters are abbreviated as follows: deposition pressure p, electrode distance d, deposition power P, and silane concentration SC.

solar cell all deposition parameters remained unchanged during the experiments. The deposition rate of the absorber layer of the bottom solar cell was varied by adjusting the deposition power, the silane concentration, and the deposition pressure. To ensure a similar total thickness of the devices the deposition time of the bottom solar cells absorber layer was adapted according to the deposition rate. The deposition power was varied between $20\,W$ and $400\,W$, the silane concentration was varied between 2.4% and 7%, and the deposition pressure was varied between $1\,hPa$ and $5\,hPa$.

The absorber layers of the solar cells used as reference devices in this study were processed at a deposition power of $20\,W$, an electrode distance of $11\,mm$, a deposition pressure of $1\,hPa$, and an excitation frequency of $81.36\,MHz$. This parameter set yields a deposition rate for the reference process of approximately $0.2\,nm/s$.

For the solar cells where the μc-Si:H i-layer was processed at $3\,hPa$ the deposition power was varied between $50\,W$ and $100\,W$ with varying SC between 3.4 % and 3.9 %. For the solar cells where the μc-Si:H i-layer was processed at $5\,hPa$ the deposition power was varied between $50\,W$ and $400\,W$ while the SC was varied from 2.4 % to 7.0 %. The simultaneous variation of the deposition pressure, the deposition power, and the silane concentration was necessary to achieve the optimal phase mixture for the μc-Si:H i-layers at elevated deposition rates (see Chapter 4) and, thus, to guarantee the optimal processing conditions for the fabrication of high quality thin-film solar cells. The deposition parameters of the μc-Si:H absorber layer for the reference process as well as for the two deposition regimes conducted at elevated deposition pressures are summarized in Table 7.1.

7.2 Photovoltaic parameters

Figure 7.1 shows the photovoltaic parameters as a function of the deposition rate of the absorber layer of the μc-Si:H bottom solar cell prepared at various deposition pressures and deposition powers. The highest device performance with an conversion efficiency of

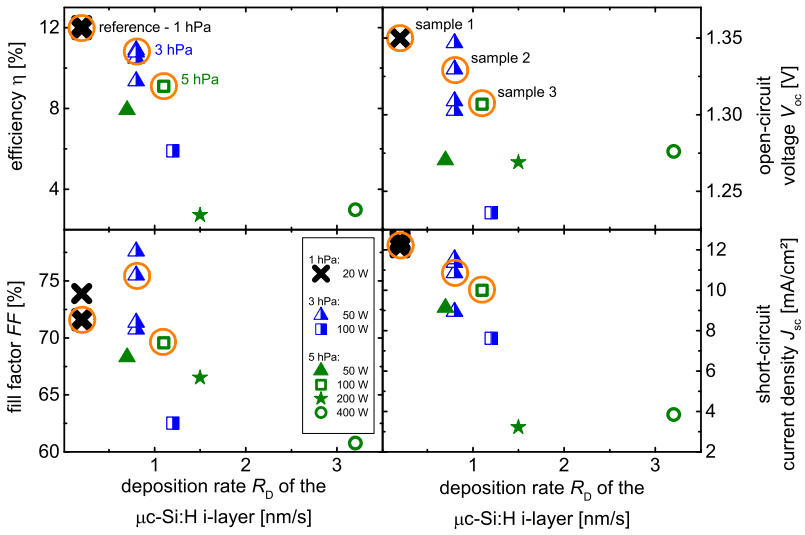

Figure 7.1: Photovoltaic parameters (conversion efficiency η, fill factor FF, open-circuit voltage V_{oc}, and short-circuit current density J_{sc}) as a function of the deposition rate R_D. The circles indicate samples 1, 2, and 3, which were further investigated by light induced degradation measurements.

12.1 % was achieved with the reference process at a deposition rate of $0.2\,nm/s$. With increasing deposition rate the conversion efficiency of the solar cells decreases to 9.1 % for a deposition rate of $1.1\,nm/s$. Increasing the deposition rate above $1.2\,nm/s$ results in a significant decrease of the device performance. The open-circuit voltage for those samples is below $1.3\,V$ while the short-circuit current density is below $4\,mA/cm^2$.
The best solar cells where the μc-Si:H i-layers were processed at elevated deposition pressures of $3\,hPa$ and $5\,hPa$ show conversion efficiencies of 10.9 % and 9.1% and deposition rates of $0.8\,nm/s$ and $1.1\,nm/s$, respectively. The photovoltaic parameters and the depositions conditions of the best solar cells of each regime are summarized in Table 7.2. In the following these solar cells will be referred to as sample 1, sample 2, and sample 3, according to Table 7.2. Comparing sample 1 and sample 3 an increase of the deposition rate from $0.2\,nm/s$ to $1.1\,nm/s$ resulted in a decrease of $45\,mV$ in the open-circuit voltage, and a decrease in the short-circuit current density of approximately $2\,mA/cm^2$. Comparing sample 1 and sample 2 the open-circuit voltage decreases by $20\,mV$ while the short-circuit current density decreases by $1.3\,mA/cm^2$, with an increase

	p [hPa]	d [mm]	P [W]	SC [%]	R_D [nm/s]	η [%]	FF [%]	J_{sc} [mA/cm^2]	V_{oc} [V]
sample 1	1	11	20	5.2	0.2	12.1	73.9	12.1	1.35
sample 2	3	10	50	3.8	0.8	10.9	75.5	10.8	1.33
sample 3	5	10	100	3.8	1.1	9.1	69.6	10.0	1.31

Table 7.2: Deposition and photovoltaic parameter for sample 1 (reference process) and samples 2 and 3. Samples 2 and 3 are the samples which show the highest conversion efficiency for the sample sets where the absorber layer of the bottom solar cell was processed at 3 hPa and 5 hPa, respectively. The deposition parameters are abbreviated as follows: deposition pressure p, electrode distance d, deposition power P, silane concentration SC, and deposition rate R_D. The photovoltaic parameters describe the conversion efficiency η, the fill factor FF, the open-circuit voltage V_{oc}, and the short-circuit current density J_{sc}.

of the deposition rate from 0.2 nm/s to 0.8 nm/s. The FF increases for 4% on absolute scale when comparing sample 1 and sample 2. Considering sample 1 and sample 3 a decrease in FF of approximately 2% on absolute scale is observed.
Samples 1 to 3 were further investigated by light-induced degradation (LID) and EQE measurements.

7.3 Light soaking

Figure 7.2 shows the photovoltaic parameters of samples 1 to 3 as function of the degradation time. The conversion efficiency of sample 1 decreases from 12.1 % to 10.4 % after 1000 h of LID. For sample 2 the conversion efficiency of the solar cell decreases from 10.9 % to 9.9 % after the light soaking procedure. For sample 3 a reduction in the solar cells conversion efficiency from 9.1 % to 8.0 % within the first 1000 h of LID is observed. No relation between the Jsc or Voc and the degradation time is seen for any sample. For sample 3 there is a decrease in short-circuit current density and open-circuit voltage at degradation times of 150 h and 300 h. This is attributed to contacting issues during the measurement of the IV-characteristic.
For the time frame of 0 h - 100 h of LID, the fill factors of all samples decrease with increasing degradation time. After 100 h of LID the fill factors for all three samples increases slightly with increasing degradation time. However, the interpretation of the fill factor of multijunction solar cells should be taken with care. For example a high value of FF can be caused by a mismatch between the currents generated by the top and the bottom solar cell. Thus, it is seen that the current matching between a-Si:H top solar cell and μc-Si:H bottom solar cell changes with proceeding degradation time.

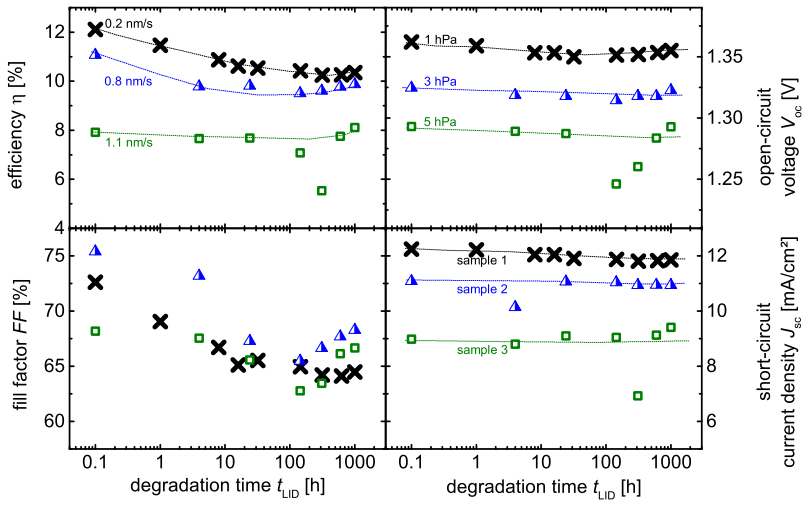

Figure 7.2: Photovoltaic parameters (conversion efficiency η, fill factor FF, open-circuit voltage V_{oc}, and short-circuit current density J_{sc}) as a function of time for light induced degradation (*LID*). The *LID* was performed with an illumination of $1000\,W/m^2$, and a controlled temperature of $50°C$.

Figure 7.3 shows the current density J_{QE} derived from EQE measurements for top and bottom solar cell as a function of deposition rate R_D before (Figure 7.3a) and after (Figure 7.3b) $1000\,h$ of *LID*. Before *LID* the J_{QE} generated by the top and the bottom solar cell decreases with increasing deposition rate. Although the thicknesses of each sub cell were kept similar across all samples, the considerable difference between the J_{QE} generated from the top solar cell and the bottom solar cell show non-ideal current matching conditions.

After *LID* the J_{QE} generated by the top solar cell increases slightly with increasing deposition rate, whereas the J_{QE} generated by the bottom solar cell decreases with increasing deposition rate. The values for the J_{QE} for the top solar cells are reduced after *LID* compared to the initial values due to the Staebler-Wronski-Effect. Prior to *LID* all samples are limited by the current of the bottom solar cell in the as-deposited state. After the *LID* samples 2 and 3 are still limited by the current of the bottom solar cell whereas sample 1 shows good current matching conditions between the a-Si:H top and μc-Si:H bottom solar cell. The quality of the matching between the top and the bottom solar cell current is visually expressed by the difference (ΔJ_{QE}) between the

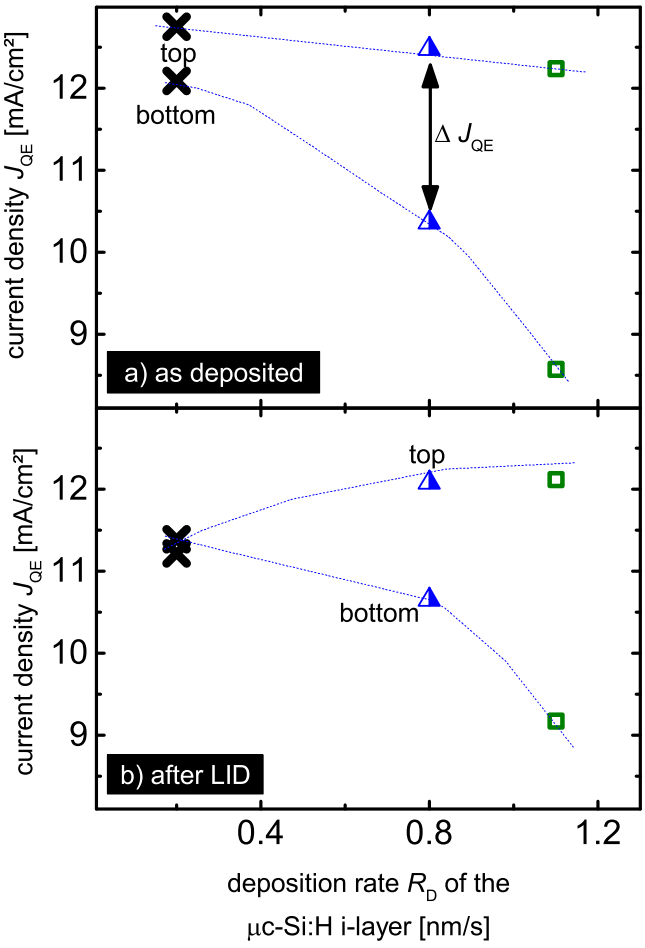

Figure 7.3: Current density J_{QE} of the top and the bottom solar cells, derived from EQE measurements, as a function of deposition rate R_D of the μc-Si:H i-layer before (a) and after (b) 1000 h of light induced degradation.

J_{QE} values for top and bottom solar cell for each sample. After *LID*, the difference ΔJ_{QE} decreases for sample 1 from $0.66\,mA/cm^2$ to $0.17\,mA/cm^2$, for sample 2 from $2.1\,mA/cm^2$ to $1.4\,mA/cm^2$, and for sample 3 from $3.7\,mA/cm^2$ to $3\,mA/cm^2$.

Figure 7.4a, 7.4b, and 7.4c shows the EQE for samples 1, 2, and 3, respectively. The current density values J_{QE} for the top and bottom solar cells before and after *LID* are displayed in each figure. The initial current values are displayed in bold face, and the EQE curves for the initial case are displayed as solid lines. The EQE curves for the stabilized solar cells are displayed by dashed lines.

The EQE curve of the top solar cell as well as the bottom solar cell of the reference sample are both reduced by the *LID* (see Figure 7.4a). The EQE of the top solar cell is reduced in the wavelength region between $380\,nm$ and $580\,nm$, whereas the EQE of the bottom solar cell is affected in the wavelength region between $650\,nm$ and $870\,nm$. Both samples deposited at elevated deposition rates show a reduced EQE for the bottom solar cell compared to sample 1 before and after *LID*. The reduction is more pronounced for the sample 3 compared to sample 2. Furthermore, the top and bottom solar cells of sample 2 and 3 are less affected by the *LID* compared to the reference sample 1.

7.4 Discussion

In the following the effect of a varied deposition rate on the device performance of the tandem solar cells presented in this chapter is discussed. Furthermore the *LID* of the tandem solar cells as well as the current matching conditions between the top and the bottom solar cell are discussed.

To achieve high deposition rates for the optimal phase mixture for microcrystalline silicon it is necessary to adjust the deposition parameters over a broad range (see Chapter 4). Adapting the deposition parameters may strongly influence the reactions in the glow discharge.

The fact that the quantum efficiency of the top solar cell is not strongly affected in the as deposited state by the application of high deposition rates for the intrinsic absorber layer of the bottom solar cell shows that the deposition conditions for the intrinsic absorber layer of the bottom solar cell are not such aggressive that the interface between the top and the bottom solar cell is damaged. As outlined in Chapter 6 a severe damage of the pi-interface of the bottom solar cell due to ion bombardment is unlikely. A deterioration of this interface due to structural inhomogeneities or altered nucleation conditions at the substrate/film interface at elevated growth rates can not be excluded. Therefore, the decrease of the open-circuit voltage and the short-circuit current density with increasing deposition rate in the as deposited case can either be attributed to interface effect or to a decrease in absorber layer material quality with increasing deposition rate.

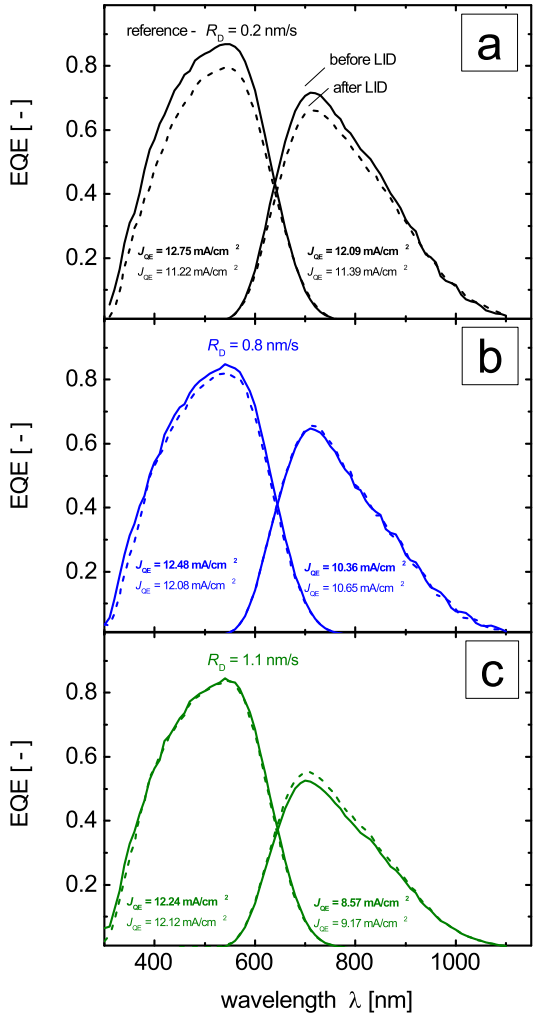

Figure 7.4: *EQE* measurements for the top and bottom solar cells of sample 1 (a), sample 2 (b), and sample 3 (c) before and after *LID*. The straight lines visualize the measurement results obtained for the as deposited state of the solar cell. The dashed lines show the measurement results after 1000 *h* of *LID*. The J_{QE} values for the top and the bottom solar cells are indicated close to the according *EQE* curve, in bold face for the as deposited state.

The determination of the photovoltaic parameters as a function of the degradation time show that samples 2 and 3 are less affected by the light induced degradation than sample 1. Relative to the initial value for sample 1 a decrease in conversion efficiency of 15% is observed. For sample 2 and 3 a decrease in conversion efficiency of 11% and 2% are observed, respectively. The EQE measurements support these observations. The top and the bottom solar cells of samples 2 and 3 are observed to be less affected by the light induced degradation. For the bottom solar cells of samples 2 and 3 this effect is attributed to a more homogeneous Raman intensity ratio throughout the whole layer for the silicon films deposited at elevated deposition rates compared to the reference layers. Investigations on the evaluation of the Raman intensity ratio along the growth axis were presented in Chapter 5. Thus, the intrinsic absorber layers of the bottom solar cell contain less amorphous tissue which is susceptible for light induced degradation. Bonnet-Eymard et al. showed the degradation of the top solar cell to be influenced by deposition rate of the bottom solar cell's intrinsic absorber layer [194]. However, the effect of a less pronounced degradation of the top solar cell with increasing deposition rate of the μc-Si:H absorber layer is counter intuitive. This effect needs more clarification in the future through a dedicated experiment. For such an experiment the power matching method should be considered. This method enables to investigate the degradation of each sub cell independent of the current matching conditions [195]. Here a final conclusion based on the EQE measurement of three solar cells would not be reasonable.

A slight increase of the conversion efficiency of sample 2 and 3 is observed for degradation times beyond $100\,h$ (see Figure 7.2). Additionally, an increase of the fill factor is observed for all samples for degradation times exceeding $100\,h$. Both effects can be attributed to a bottom limited device and improved current matching conditions after the light induced degradation (see Figure 7.3). In case of a bottom limitation of a thin-film tandem solar cell the superposition of the current-voltage characteristics for both sub-cells leads to a final current-voltage characteristic with a steep slope at the interception with the x-axis. This can lead to an erroneous determination of the fill factor.

In summary, all photovoltaic parameters decrease with increasing deposition rate. However under an economical point of view it might be reasonable to scale the processes which yield high deposition rates for intrinsic μc-Si:H from laboratory scale to industry scale if the decrease in device performance is overbalanced by a decrease in processing time. To which extend this applies to the deposition processes developed here is discussed in Chapter 8.

7.5 Conclusion

The effect of the deposition rate of μc-Si:H absorber layers was investigated in the range of $0.2\,nm/s$ to $3.2\,nm/s$ on the performance of thin-film silicon tandem solar cells. All photovoltaic parameters are observed to decrease with increasing deposition rate. For a deposition rate of $0.8\,nm/s$, which corresponds four times the deposition rate of the reference process, an initial conversion efficiency of 10.9% with a stabilized conversion efficiency of 9.9% was observed. For selected samples the photovoltaic parameters were measured as a function of the degradation time. The samples where the intrinsic absorber layer of the bottom solar cells was deposited at elevated growth rates show to be less affected by the light induced degradation than the reference sample. Calculations on possible cost benefits when implementation process steps yielding high deposition rates for intrinsic μc-Si:H are presented in the following chapter.

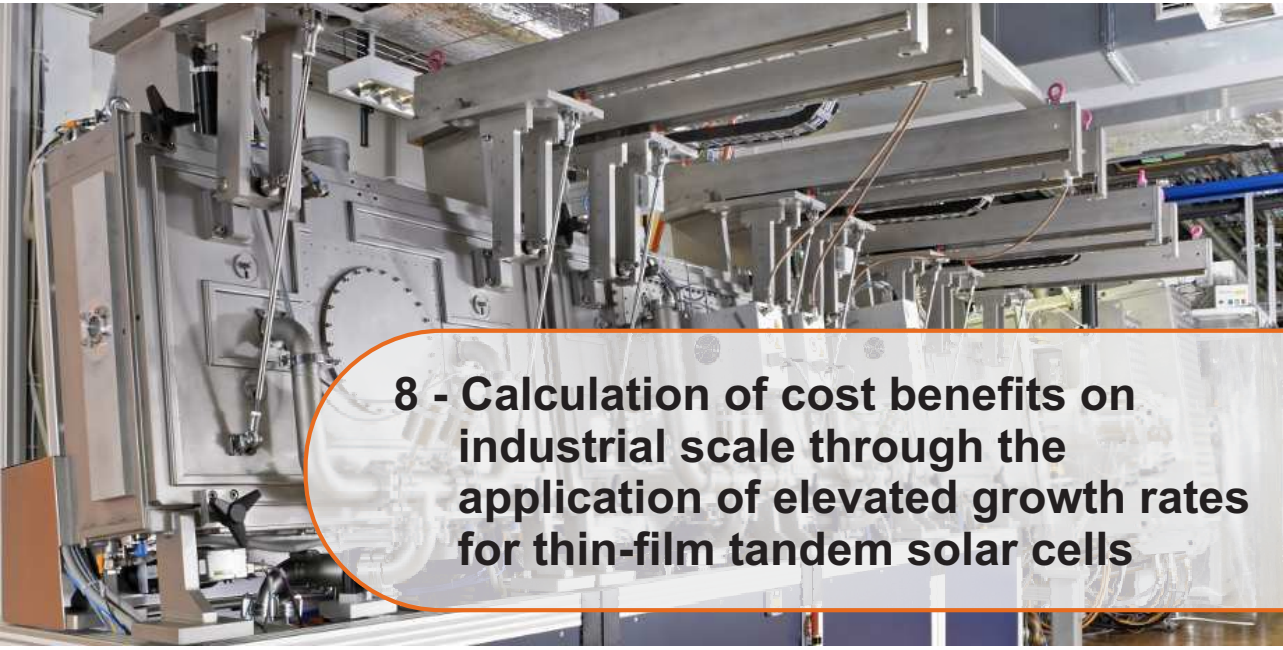

8 - Calculation of cost benefits on industrial scale through the application of elevated growth rates for thin-film tandem solar cells

In this chapter the results of a calculation on the cost benefits when implementing deposition processes which yield high growth rates for the μc-Si:H intrinsic absorber layer of the bottom solar cell into the process chain are presented.

8.1 Introduction

The device performance was shown to decrease for μc-Si:H single junction solar cells (see Chapter 6) as well as for a-Si:/μc-Si:H tandem solar cells (see Chapter 7). But despite this decrease in device performance a reduction of the production cost is possible due to shortened processing times. A faster processing time increases the output of a production line and thus can overcompensate the decrease in device performance. To deduce possible benefits from the application of high deposition rates for the fabrication of the μc-Si:H bottom solar cells absorber layer model calculations are presented in this chapter. A detailed calculation of the processing time for the front end for an a-Si:H/μc-Si:H tandem module is first motivated by an estimation of a possible increase in production output based on the results presented in Chapter 7.

8.2 Approach

An estimation is presented to deduce a value for the cost benefits that can be used to compare two processes used to fabricate sample 1 (low deposition rate, $0.2\,nm/s$) and sample 2 (high deposition rate, $0.8\,nm/s$) presented in Chapter 7. No further losses in the device performance during the up-scaling of the processes to large areas are assumed. Possible interconnection losses which may be introduced during the module

fabrication process are excluded. Considering the efficiency of sample 1 of 12.1 % and an illumination intensity of $1000\,W/m^2$ together with the processing time of $180\,min$ the output for the i-chamber can be calculated to $40.33\,W/(m^2\,h)$, according to:

$$12.1\,\% \xrightarrow{1000\,W/m^2} 121 W/m^2 \xrightarrow{/\,180\,min} 40.3\,W/(m^2\,h) \tag{8.1}$$

For sample 2, with an efficiency of 10.9 % and a processing time of $70\,min$ for the absorber layer of the bottom solar cell the output value is calculated in an analogous way to $93.4\,W/(m^2\,h)$. Thus, by the introduction of processes leading to elevated deposition rates it is possible to increase the output of the i-chamber by a factor of 2.3.
Considering possible gains of production output of more than a factor of 2 a detailed calculation for the processing time of an a-Si:H/μc-Si:H tandem module follows. Figure 8.1 visualizes the process chain which was considered for the calculation. The process chain is adapted to the production line proposed by TEL Solar [196].

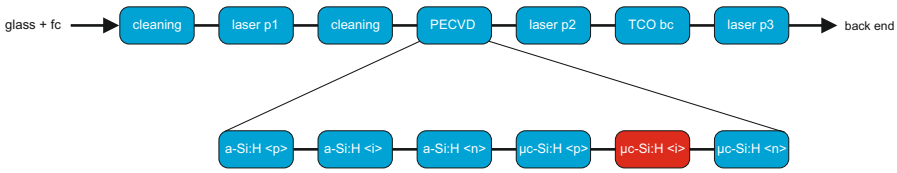

Figure 8.1: Process chain for the front end of an a-Si:H/μc-Si:H tandem solar cell considered to perform the model calculations. The processing steps were the parameters remained unchanged during the calculation are visualized in blue. The processing step were the parameter were varied during the calculated are highlighted in red.

Here the front end of the process chain of an a-Si:H/μc-Si:H solar module production line is considered for the model calculation. The following assumptions are taken as boundary conditions for the model calculation: first the choice of glass already coated with a transparent conductive oxide as substrate for the subsequent solar module fabrication, and second the termination of the front end by the last laser scribing step (p3 laser line). The front end for the processing of an a-Si:H/μc-Si:H tandem module consists of: a cleaning step ($180\,s$), the p1 laser scribing step ($203\,s$), a second cleaning step ($180\,s$), the deposition of the silicon layers by *PECVD* ($1732\,s$ + variable time for μc-Si:H i-layer), the p2 laser scribing step ($203\,s$), the application of a transparent conductive oxide as back contact ($417\,s$), and the p3 laser scribing step ($203\,s$). Details about the p1, p2, and p3 laser scribing steps as well as the concept of integrated series

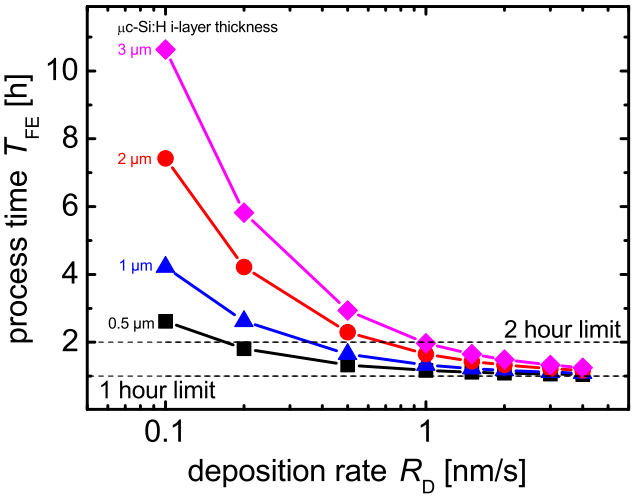

Figure 8.2: Processing time for the front end of an a-Si:H/μc-Si:H tandem solar cell based on the described model as a function of the deposition rate for the μc-Si:H absorber layer. The calculations were performed for various thicknesses of the μc-Si:H absorber layer.

connection of solar cells can be found in the work of Haas [197]. For the *PECVD* processes the following processing times were taken: a-Si:H p-layer (30 *nm*, 300 *s*), a-Si:H i-layer (250 *nm*, 655 *s*), a-Si:H n-layer (30 *nm*, 150 *s*), μc-Si:H p-layer (30 *nm*, 330 *s*), μc-Si:H i-layer (variable), and the μc-Si:H n-layer (40 *nm*, 297 *s*). For the calculation all parameter remained unchanged apart from the deposition rate and the thickness for the μc-Si:H bottom solar cell absorber layer. A substrate size of 130 *cm* x 110 *cm* with 130 cell stripes was assumed.The exact model parameter can be found in Appendix C.

Exact statements concerning the deposition rates, the absorber layer thicknesses, the processing and station times are matter of great secrecy when approaching equipment manufacturer and solar cell producer. Thus, the processing times assumed for the model calculation are based on experience gained through consultancy work and from interviewing equipment manufacturer and solar cell producer at various conferences and project meetings. Figure 8.2 shows the processing time for the front end based on the described model as a function of the deposition rate for the μc-Si:H absorber layer. The calculations were performed for various thicknesses of the μc-Si:H absorber layer. The processing time decreases with decreasing deposition rate. Independent from

the thickness of the absorber layer it shows an exponential decrease stabilizing around $1\,h$ of processing time. This exponential decrease is caused by the amount of constant processing time of approximately $52\,min$.
For an absorber layer thickness of $2\,\mu m$ the total processing time is reduced from $4.2\,h$ to $1.65\,h$ by increasing the deposition rate from $0.2\,nm/s$ to $1\,nm/s$. For a thickness of $1\,\mu m$ the gain in total processing time is less than for $2\,\mu m$. With an increase in deposition rate from $0.2\,nm/s$ to $1\,nm/s$ the total processing time is reduced from $2.6\,h$ to $1.3\,h$ for a absorber layer thickness of $1\,\mu m$. This corresponds to a reduction in processing time for the front end of an a-Si:H/μc-Si:H tandem module of a factor of 2.5 for $2\,\mu m$ and a factor 2.0 for $1\,\mu m$ absorber layer thickness of the μc-Si:H bottom solar cell.
Since the processing of the μc-Si:H absorber layer is the limiting step during the production of a-Si:H/μc-Si:H tandem modules most production lines use several deposition chambers for intrinsic μc-Si:H layers. Thus, a reduction of the processing time of more than a factor of 2 can lead to a lower demand of deposition chambers for intrinsic μc-Si:H layers and investment costs can be reduced.

8.3 Conclusion

Despite the reduction in efficiency of 1.2% for the solar cells processed at a deposition rate of $0.8\,nm/s$ compared to the reference solar cell processed at a deposition rate of $0.2\,nm/s$ (see Chapter 7), the model calculations show that the output of the deposition system in terms of Watts per hour and area can be increased by a factor of 2.3 due to reduced processing times. Furthermore, detailed calculations for the processing time of the front end for an a-Si:H/μc-Si:H tandem module show an decrease in processing time by more than a factor of 2 which can result in reduced running and investment costs.

9 - Conclusion

In the present work the relation between growth rate, material quality, and device grade conditions was investigated for intrinsic μc-Si:H. Investigations were performed for single layers on glass or on silicon wafers (Chapter 4 and 5). Based on these studies the deposition parameters leading to the most promising material composition were applied to μc-Si:H single junction solar cells (Chapter 6) as well as a-Si:H/μc-Si:H tandem (Chapter 7) solar cells. An examination of cost benefits when implementing high growth rates for the deposition of intrinsic μc-Si:H to tandem solar cells finalized the study (Chapter 8).

The study presented showed that an adaption of the deposition parameters enable to reach deposition rates up to $2.8\,nm/s$ for *OPM*-material. According to the established criteria in the field of thin-film silicon *OPM*-material with good electrical properties is considered to be of device grade quality. This syllogism is supported here by results from conductivity and *ESR* measurements. No link between defect density and deposition rate was found.

To further research the detailed implications of high growth rates for μc-Si:H investigations on the microstructure, porosity, and susceptibility for oxygen uptake were presented. The *OPM*-material deposited beyond a deposition rate of approximately $1\,nm/s$ suffered from considerable oxygen uptake. This effect is observed to increase with increasing deposition rate. The process of oxygen uptake was shown to occur along the grain boundaries open to the ambient atmosphere. Observations deduced from a shift of the TO phonon mode suggest an increase in tensile stress with increasing deposition rate. The presence of tensile stress can lead to defect states and a variation of carrier mobility. When implemented in thin-film solar cells these effects are known to cause a reduction in open-circuit voltage due to an impairment of the electric field

of the p-i-n junction. A decrease in open-circuit voltage with increasing deposition rate is also seen here. The presence of additional defect states induced by tensile stress is in contrast to the results obtained through *ESR* measurements. The investigations performed with *ESR* did not show a significant increase in defect density with increasing deposition rate. The origin of this discrepancy remains unknown and may be clarified in future studies. To prevent the creation of defect states future work could focus an the compensation of these states by e. g. micro doping. Additionally a decrease in crystal grain size accompanied by an increase in grain boundary density was observed for the *OPM*-material deposited at high deposition rates. Raman depth measurements as well as the observations gained through *TEM* imaging showed that all layers deposited at high deposition rates showed the development of a thinner incubation layer compared to the reference layer.

The effects of high deposition rates for μc-Si:H on the photovoltaic parameter of single junction solar cells presented show a decreasing device performance with increasing deposition rate. This decrease in device performance is related to an inferior material quality of the intrinsic absorber layer and to an impairment of the pi-interface by the application of processes yielding high deposition rates. The short-circuit current density measured under blue light showed to be independent of the deposition rate of the μc-Si:H absorber layer as well as of the application of a buffer layer. This suggest that the reduced device performance is related to an inferior material quality of the μc-Si:H absorber layer. However, also an increase in open-circuit voltage and fill factor with increasing buffer layer thickness was found which underlines the importance of the pi-interface for the device performance. As possible sources for an impairment of the pi-interface variation of the nucleation conditions, ion bombardment, and structural inhomogeneities at the substrate/film interface were presented. Calculation on the impact of ions in matter showed the maximal penetration depth of the bombarding ions to extend at most as far as five monolayers. These findings along with along with recently published literature values on the maximal ion energies for the *HPD* regime suggest that the damage of the pi-interface due to ion bombardment is unlikely. The impairment of pi-interface is presumably related to structural inhomogeneities or varied nucleation conditions. Future work could investigate dedicated processes with the aim to protect the pi-interface from the detrimental influence originated from the application of deposition processes yielding high deposition rates.

The results presented show that the implication that *OPM*-material is of device grade quality does not apply for intrinsic μc-Si:H deposited at deposition rates beyond $1\,nm/s$. In order to classify this material as being of device grade condition quantities describing the microstructure, the oxygen uptake, and the mechanical stress should be added to the

present criteria. The identification and formulation of specific threshold values can be subject of future work.

The application of μc-Si:H deposited at high deposition rates to thin-film tandem solar cells confirmed the effect of a decreasing device performance with increasing deposition rate. However, the solar cell with the intrinsic μc-Si:H absorber layer fabricated at high deposition rates show to be less affected by light induced degradation relative to their initial values. The experimental data suggests that the degradation of the top solar cell is affected by the deposition rate of the bottom solar cell's absorber layer. This interesting results needs more research by a dedicated experiment before the association between degradation of the top solar cell and the deposition rate of the bottom solar cell is clearly understood.

Finally, calculations on cost benefits show that from an economical point of view the decrease in device performance can be overcompensated by a decrease in processing time. Thus, the application of high deposition rates can lead to decreased cost per produced unit, an increase in system throughput, and to reduced investment costs.

As outlined in the introduction of this work the investigation of deposition processes which yield high deposition rates for μc-Si:H are of great interest for academia as well as for the industry. On the one hand, the limitations for the μc-Si:H layers and thin-film solar cells induced by the increase in deposition rate were shown. On the other hand, a benefit for the industrial application of high deposition rates for μc-Si:H was demonstrated.

Appendix

Appendix A: Detection of laterally inhomogenous element distribution by secondary ion mass spectrometry (*SIMS*)

The possibility to detect laterally inhomogenous element distribution by secondary ion mass spectrometry has already be described elsewhere [156, 137] and will therefore be described briefly.

The relation between the monomer and dimer carbon concentration for a lateral homogeneous distribution is derived in the following. This relation was proven experimentally by investigations on the emission of mono- and diatomic carbon during *SIMS* depth profiling of a *CZ*-wafer with lateral homogeneously implanted carbon [137]. The carbon atoms have been implanted at $150\,keV$ in a silicon *CZ*-grown wafer leading to a lateral carbon concentration of $10^{16}\,cm^{-2}$. The reaction between carbon and silicon can be described by the reaction equation:

$$4\,C + 4\,Si \rightleftharpoons C_2 + 2\,SiC + Si_2 \tag{A.1}$$

The law of mass action allows to derive the equilibrium constant K,

$$\Rightarrow K_c = \frac{[C_2]\,[SiC]^2\,[Si_2]}{[C]^4\,[Si]^4} = \text{const} \tag{A.2}$$

With the assumption that the carbon concentration is significantly smaller than the silicon concentration, the silicon monomer and dimer concentrations can be considered to be constant:

$$[C] \ll [Si] \Rightarrow [Si] \approx \text{const} \wedge [Si_2] \approx \text{const} \tag{A.3}$$

$$\Rightarrow \frac{[Si]^4}{[Si_2]} K_c = \frac{[C_2]\,[SiC]^2}{[C]^4} \tag{A.4}$$

From the above assumption it is also valid to assume the silicon carbide concentration to be proportional to the carbon concentration:

$$[C] \ll [Si] \Rightarrow [SiC] \propto [C] \tag{A.5}$$

$$\Rightarrow \underbrace{\frac{[Si]^4}{[Si_2]} K_c}_{=\text{const}} [C]^4 = [C_2]\,[SiC]^2 \tag{A.6}$$

Thus for a lateral homogeneous distribution of carbon it is possible to show the carbon dimer concentration to be proportional to the square of the carbon monomer concentration:

$$\Rightarrow [C_2] \propto [C]^2 \tag{A.7}$$

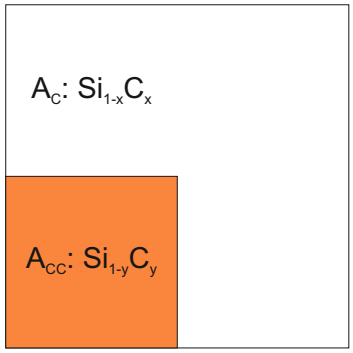

Figure A.1: Schematic of a silicon layer with an inhomogenous distribution of carbon. A_c represents the lateral area of the silicon film slightly contaminated with carbon. A_{cc} represents the lateral area of the silicon film heavily contaminated with carbon.

Figure A.1 schematically shows a silicon layer with an inhomogenous distribution of carbon. With A_c describing the lateral area of the silicon film slightly contaminated with carbon and A_{cc} describing the lateral area of the silicon film heavily contaminated with carbon. Considering equation *A.7* it is possible to calculate the mean concentrations of the carbon monomers and dimers:

$$[C]_{mean} \propto \frac{A_c\, x + A_{cc}\, y}{A_c + A_{cc}} \tag{A.8}$$

$$[C_2]_{mean} \propto \frac{A_c\, x^2 + A_{cc}\, y^2}{A_c + A_{cc}} \tag{A.9}$$

Assuming x and y being constant with the heavily contaminated area being smaller than the total area it is possible to express the average carbon dimer concentration to be proportional to the average carbon monomer concentration:

$$\begin{aligned} &x = \text{const} \ \wedge y = \text{const for } 0 < A_{cc} < A_c + A_{cc} = A_{tot} \\ &\Rightarrow [C_2]_{mean} \propto [C]_{mean} \end{aligned} \tag{A.10}$$

Finally, when displaying the carbon dimer concentration versus the carbon monomer

concentration on a double logarithmic scale both normalized to the silicon concentration it is possible to deduce the relation between the carbon monomer and dimer concentrations from the slope of the characteristic. For a μc-Si:H layer the presence of an inhomogenous distribution of carbon suggests the uptake of atmospheric gases to happen along the grain boundaries (see Chapter 5).

Appendix B: samples list

During the course of the studies presented here, a large number of silicon layers, layer stacks, and solar cells have been prepared. In the following the detailed deposition parameters and measurement results for the samples are given:

Sample list: silicon films deposited during the process and material development study (see Chapter 4)

sample name	p $[hPa]$	d $[mm]$	P $[W]$	SC $[\%]$	R_D $[nm/s]$	σ_d $[S/cm]$	σ_{ph} $[S/cm]$	σ_d/σ_{ph} $[-]$	I_c^{RS} $[\%]$	series
10P-285	3	10	100	3.4	1.2	4.6×10^{-7}	2.8×10^{-5}	61	69.9	B
11P-150	5	10	50	2.4	0.7	7.7×10^{-9}	3.6×10^{-6}	468	70.6	C
11P-189	5	10	100	3.4	1.1	1.7×10^{-6}	9.4×10^{-5}	56	63.6	A B C
11P-214	5	5	100	2.4	0.4	2.9×10^{-8}	3.4×10^{-5}	1194	54.3	A
11P-222	5	7	100	2.4	0.9	1.9×10^{-7}	8.4×10^{-6}	43	68.6	A
11P-231	8	10	100	1.5	0.4	3.8×10^{-9}	3.2×10^{-6}	832	81.0	B
11P-264	5	10	200	5.7	1.5	4.7×10^{-7}	9.7×10^{-5}	206	54.2	C
11P-399	5	10	400	7.4	2.4	1.1×10^{-10}	2.9×10^{-6}	27810	57.8	C
11P-469	5	10	600	9.9	2.8	1.8×10^{-7}	3.2×10^{-5}	175	43.0	C

Table A.1: Deposition parameters and measurement results for the samples considered to be of optimal phase mixture (see Chapter 4). The deposition parameters are abbreviated as follows: deposition pressure p, electrode distance d, deposition power P, silane concentration SC, deposition rate R_D. The measurement results describe the dark conductivity σ_d, the photo conductivity σ_{ph}, photosensitivity σ_d/σ_{ph}, and the Raman intensity ratio I_c^{RS}.

Sample list: silicon films deposited at high growth rates to investigate the porosity, atmospheric gas diffusion, and microstructure (see Chapter 5)

sample name	p $[hPa]$	d $[mm]$	P $[W]$	SC $[\%]$	R_D $[nm/s]$	I_c^{RS} $[\%]$	SiH_x peak position $[cm^{-1}]$	C_O^{180} $[\%]$	ΔC_O $[\%]$	sample set
12P-189	5	10	600	4.8	1.4	75	2102	4.2	1.4	set 1
12P-190	5	10	400	3.8	1.2	78	2100	5.7	0.9	set 1
12P-191	5	10	100	3.8	1.1	78	2100	0.4	0.4	set 1
12P-193	5	10	200	2.9	1.0	80	2100	6.9	1.4	set 1
12P-208	5	10	100	3.8	1.1	74	2086	0.3	-0.1	set 2
12P-216	5	10	200	5.7	2.0	62	2055	2	0.0	set 2
12P-218	5	10	400	7.0	2.3	60	2048	3.6	-0.3	set 2
12P-226	5	10	600	7.0	2.0	43	2009	3.3	-0.1	set 2
12P-299	1	11	20	5.2	0.2	69	2075	0	0.0	reference

Table A.2: Deposition parameters and measurement results for the samples with the detailed investigation of microstructure and porosity (see Chapter 5). The deposition parameters are abbreviated as follows: deposition pressure p, electrode distance d, deposition power P, silane concentration SC, deposition rate R_D. The measurement results describe the Raman intensity ratio I_c^{RS}, the SiH_x peak position, the oxygen content after 180 days of storage at ambient C_O^{180}, and the difference in oxygen upon the HF dip ΔC_O.

Sample list: μc-Si:H single junction solar cells with the μc-Si:H absorber layer deposited at varying deposition rates (see Chapter 6)

sample name	p [hPa]	d [mm]	P [W]	SC [%]	R_D [nm/s]	η [%]	FF [%]	V_{oc} [mV]	J_{sc} [mA/cm^2]	
13P-209	1	11	20	5.2	0.2	7.6	71.9	554.0	19.0	sample A
13P-214	1	11	20	5.2	0.2	8.5	72.0	551.0	21.3	sample B
13P-288	5	10	200	5.2	1.8	5.6	63.8	503.0	17.4	series C
13P-289	5	10	50	2.0	0.8	7.4	69.2	544.0	19.6	series C
13P-290	5	10	100	3.4	1.3	6.3	64.9	515.0	18.9	series C
13P-291	5	10	400	7.0	2.4	5.3	61.7	496.0	17.2	series C
13P-296	5	10	600	8.3	2.7	4.5	59.3	443.0	17.3	series C
13P-223	5	10	100	3.8	1.0	6.0	62.4	519.0	18.6	series D
13P-227	5	10	50	2.0	0.6	7.4	70.4	544.2	19.3	series D
13P-238	5	10	100	3.4	1.1	6.3	65.4	513.0	18.8	series D
13P-239	5	10	200	5.2	1.4	5.6	61.4	502.0	18.1	series D
13P-242	5	10	400	7.0	2.0	5.5	65.2	534.0	15.8	series D
13P-273	5	10	400	7.0	2.3	4.6	55.9	454.0	18.0	series D
13P-275	5	10	600	8.3	2.3	5.6	61.2	489.0	18.7	series D
13P-297	5	10	200	5.2	1.9	5.1	61.4	463.0	17.8	series E
13P-298	5	10	50	2.0	0.7	7.3	69.2	543.0	19.4	series E
13P-299	5	10	100	3.4	1.4	6.6	64.2	508.0	20.3	series E
13P-293	3	10	100	3.4	1.2	5.9	62.4	477.0	19.8	series F
13P-294	3	10	200	3.8	1.3	5.1	60.5	462.0	18.3	series F
13P-295	3	10	50	2.9	1.0	6.7	64.0	506.0	20.7	series F
13P-225	3	10	100	3.4	1.2	5.4	60.1	468.0	19.1	series G
13P-226	3	10	50	2.9	0.9	6.9	63.5	506.0	21.3	series G
13P-241	3	10	200	3.8	1.2	5.8	62.5	488.0	18.7	series G
13P-298	5	10	50	2.0	1.0	7.3	69.2	543.0	19.4	series H
13P-324	5	10	50	2.0	1.0	7.2	70.5	554.0	18.4	series H
13P-325	5	10	50	2.0	1.0	7.6	70.3	552.0	19.6	series H
13P-326	5	10	50	2.0	1.0	7.4	69.1	545.0	19.7	series H
13P-295	5	10	50	2.0	1.0	6.7	64.0	506.0	20.7	series H
13P-067	3	10	50	2.9	1.1	6.8	64.5	509.0	20.8	series I
13P-069	3	10	50	2.9	1.1	6.7	64.6	516.0	20.1	series I
13P-070	3	10	50	2.9	1.1	6.4	62.1	519.0	19.9	series I
13P-071	3	10	50	2.9	1.1	6.3	60.1	506.0	20.6	series I

Table A.3: Deposition and photovoltaic-parameters for the samples discussed in Chapter 6. The deposition parameters are abbreviated as follows: deposition pressure p, electrode distance d, deposition power P, silane concentration SC, and deposition rate R_D. The deposition parameter refer to the intrinsic absorber layer of the μc-Si:H bottom solar cell. The photovoltaic parameters describe the efficiency η, the fill factor FF, the open-circuit voltage V_{oc}, and the short-circuit current density J_{sc}.

Sample list: thin-film tandem solar cells with the μc-Si:H absorber layer deposited at elevated deposition rates (see Chapter 7)

sample name	p [hPa]	d [mm]	P [W]	SC [%]	R_D [nm/s]	η [%]	FF [%]	J_{sc} [mA/cm^2]	V_{oc} [V]	
12P-170	1	11	20	5.2	0.2	12	71.5	12.5	1.4	
12P-225	1	11	20	5.2	0.2	12.1	73.9	12.1	1.4	sample 1
12P-158	1	11	20	5.2	0.2	11.9	71.7	12.4	1.4	
12P-374	3	10	50	3.8	0.8	10.9	75.9	10.8	1.3	sample 2
12P-258	3	10	50	3.8	0.8	9.3	77.6	8.9	1.3	
12P-275	3	10	50	3.8	0.8	10.5	70.7	11.4	1.3	
12P-390	3	10	50	3.8	0.8	10.8	71.4	11.5	1.3	
12P-391	3	10	100	3.4	1.2	5.9	62.5	7.6	1.2	
12P-367	5	10	400	7.0	3.2	3.0	60.8	3.9	1.3	
12P-368	5	10	100	3.8	1.1	9.1	69.6	10.0	1.3	sample 3
12P-369	5	10	200	5.7	1.5	2.7	66.5	3.2	1.3	
12P-373	5	10	50	2.4	0.7	7.9	68.3	9.1	1.3	

Table A.4: Deposition and photovoltaic-parameters for the samples discussed in Chapter 7. The deposition parameters are abbreviated as follows: deposition pressure p, electrode distance d, deposition power P, silane concentration SC, deposition rate R_D, and processing time t. The deposition parameter refer to the intrinsic absorber layer of the μc-Si:H bottom solar cell. The photovoltaic parameters describe the efficiency η, the fill factor FF, the open-circuit voltage V_{oc}, and the short-circuit current density J_{sc}.

Appendix C: Input parameter for the model calculation (see Chapter 8)

Input parameter for cleaning procedure, laser processes, and the application of the TCO back contact:

cleaning		laser p1/p2/p3		TCO back contact	
		number of lines	130	R_D $[nm/s]$	1.4
		speed of laser $[cm/s]$	100	thickness $[nm]$	80
transport $[s]$	60	transport $[s]$	60	transport $[s]$	60
process $[s]$	120	process $[s]$	143	pumping $[s]$	30
				pre conditioning $[s]$	180
				deposition $[s]$	57.1
				post conditioning $[s]$	60
				pumping $[s]$	30
sum $[s]$	180	sum $[s]$	203	sum $[s]$	417

Input parameter for the amorphous top solar cell:

a-Si:H <p>		a-Si:H <i>		a-Si:H <n>	
R_D $[nm/s]$	0.6	R_D $[nm/s]$	0.4	R_D $[nm/s]$	
thickness $[nm]$	30	thickness $[nm]$	250	thickness $[nm]$	30
transport $[s]$	60	transport $[s]$	0	transport $[s]$	0
pumping $[s]$	30	pumping $[s]$	30	pumping $[s]$	30
pre conditioning $[s]$	10	pre conditioning $[s]$	0	pre conditioning $[s]$	0
deposition $[s]$	50	deposition $[s]$	625	deposition $[s]$	60
post conditioning $[s]$	0	post conditioning $[s]$	0	post conditioning $[s]$	60
pumping $[s]$	0	pumping $[s]$	0	pumping $[s]$	0
chamber cleaning $[s]$	150	chamber cleaning $[s]$	0	chamber cleaning $[s]$	0
sum $[s]$	300	sum $[s]$	655	sum $[s]$	150

Input parameter for the microcrystalline bottom solar cell:

μc-Si:H <p>		μc-Si:H <i>		μc-Si:H <n>	
R_D $[nm/s]$	0.2	R_D $[nm/s]$	var	R_D $[nm/s]$	0.15
thickness $[nm]$	30	thickness $[nm]$	var	thickness $[nm]$	40
transport $[s]$	60	transport $[s]$	0	transport $[s]$	0
pumping $[s]$	30	pumping $[s]$	30	pumping $[s]$	30
pre conditioning $[s]$	20	pre conditioning $[s]$	0	pre conditioning $[s]$	0
deposition $[s]$	150	deposition $[s]$	var	deposition $[s]$	267
post conditioning $[s]$	70	post conditioning $[s]$	0	post conditioning $[s]$	0
pumping $[s]$	0	pumping $[s]$	0	pumping $[s]$	0
chamber cleaning $[s]$	0	chamber cleaning $[s]$	0	chamber cleaning $[s]$	0
sum $[s]$	330	sum $[s]$	var	sum $[s]$	297

Appendix D: Symbols and abbreviations

symbol	description	unit
Ag	silver	–
A	area	m^2
$AM\,1.5$	standardized $AM\,1.5$ spectrum	–
a-Si:H	hydrogenated amorphous silicon	–
α	absorption coefficient	cm^{-1}
A_e	electrode area	–
BB	Bragg-Brentano geometry	–
BF	bright field image	–
CZ	Choralski	–
J_{sc}	short circuit current density	$A\,m^{-2}$
I_{MPP}	short circuit current at the MPP	$A\,m^{-2}$
$J_{sc,blue}$	short circuit current density measured with a $BG7$-filter	$A\,m^{-2}$
$J_{sc,red}$	short circuit current density measured with a $OG590$-filter	$A\,m^{-2}$
I_{sc}	short circuit current	A
I	current	A
CF	crossflow mode gas distribution	–
J_{ph}	photo current density	$A\,m^{-2}$
I	current	A
c-Si	crystalline silicon	–
J_{QE}	short circuit current density derived from EQE measurement	$A\,m^{-2}$
C_{tot}	sum of the capacitance of both plasma sheath	F
$cat-CVD$	catalytic chemical vapor deposition	–
C_H	hydrogen content	%
C_H^*	hydrogen content, uncorrected	%
C_O	oxygen content	%
d	thickness	m
d_p	diameter of the electrode	m
DSR	differential spectral response	–
d	electrode distance	m
δ	crystal size of the coherent domains	nm
DF	dark field image	–
η	efficiency	%
EQE	external quantum efficiency	–
η_{ini}	initial efficiency	%
η_{stb}	stabilized efficiency	%
ESR	electron spin resonance	–
E	energy	eV
E_G	bandgap energy	eV
$EEDF$	electron energy distribution function	–
E_{max}	maximum ion energy of bombarding ions	eV
$FTIR$	Fourier Transform Infrared Spectroscopy	–
$FWHM$	full width half maximum	cm^{-1}
GI	grazing incidence geometry	–

γ	fixed angle used in *GI* geometry	$^\circ$
$HWCVD$	hot wire chemical vapor deposition	–
HS	heating station of the deposition system	–
H_2	hydrogen	–
HPD	high pressure depletion	–
I_c^{RS}	Raman intensity ratio	%
I_{cc}	integrated crystalline intensity	–
I_a	integrated amorphous intensity	–
I_R	Raman intensity	–
I_c^{XRD}	crystalline volume fraction measured through XRD	%
I_c	crystallinity	%
KOH	potassium hydroxide	–
l	length of silver pads	m
λ	wavelength	m
MPP	Maximum Power Point	–
$MC1$	load lock 1 of the deposition system	–
$MC2$	load lock 2 of the deposition system	–
N_H	amount of bonded hydrogen atoms	cm^{-3}
N_O	amount of bonded oxygen atoms	cm^{-3}
N_D	defect density	cm^{-3}
ν	frequency	Hz
ν_{ex}	excitation frequency	Hz
ω	angular frequency	s^{-1}
ω_i	angular frequency of incident photons	s^{-1}
ω_s	angular frequency of scattered photons	s^{-1}
ω_k	angular frequency of emitted/annihilated phonons	s^{-1}
OPM	optimal phase mixture	–
$PECVD$	plasma enhanced chemical vapor deposition	–
P_{in}	incident power	W
P_{MPP}	maximum power generated by solar cells	W
$PC\,i$	for $i = 1..5$, process chamber i of the deposition system	–
PH_3	phosphine	–
Φ	photon flux	$m^{-2}\,s^{-1}$
P	deposition power	W
p	deposition pressure	hPa
$P[SiH_4]$	silane particle flow	s^{-1}
$Q[SiH_4]$	silane mass flow	$sccm$
$Q[H_2]$	hydrogen mass flow	$sccm$
RF	radio frequency	–
R	resistance	Ω
R_D	deposition rate	–
SnO_2	tin dioxide	–
SiH_4	silane	–
SH	showerhead mode gas distribution	–
s	space between silver pads	m
σ	conductivity	S/cm

σ_d	dark conductivity	S/cm
σ_{ph}	photoconductivity	S/cm
SWE	Staebler-Wronski effect	–
$SIMS$	Secondary Ion Mass Spectrometry	–
TC	transfer chamber of the deposition system	–
TMB	trimethylboron	–
T	temperature	$^\circ C$, K
T_W	wire temperature	$^\circ C$

Appendix E: Constants

constant	description	value
A_{640}	proportionality constant to calculate the hydrogen content	$2 \times 10^{19}\, cm^{-2}$
A_O	proportionality constant to calculate the oxygen content	$7.8 \times 10^{18}\, cm^{-2}$
c	speed of light	$299792458\, m\, s^{-1}$
e	elementary charge	$1.602176565 \times 10^{-19}\, C$
$\hbar$	reduced Planck constant	$1.054571726 \times 10^{-34}\, J\, s$
h	Planck constant	$6.62606957 \times 10^{-34}\, J\, s$
N_{Si}	silicon atom density	$5 \times 10^{22}\, cm^{-3}$

List of Figures

List of Tables

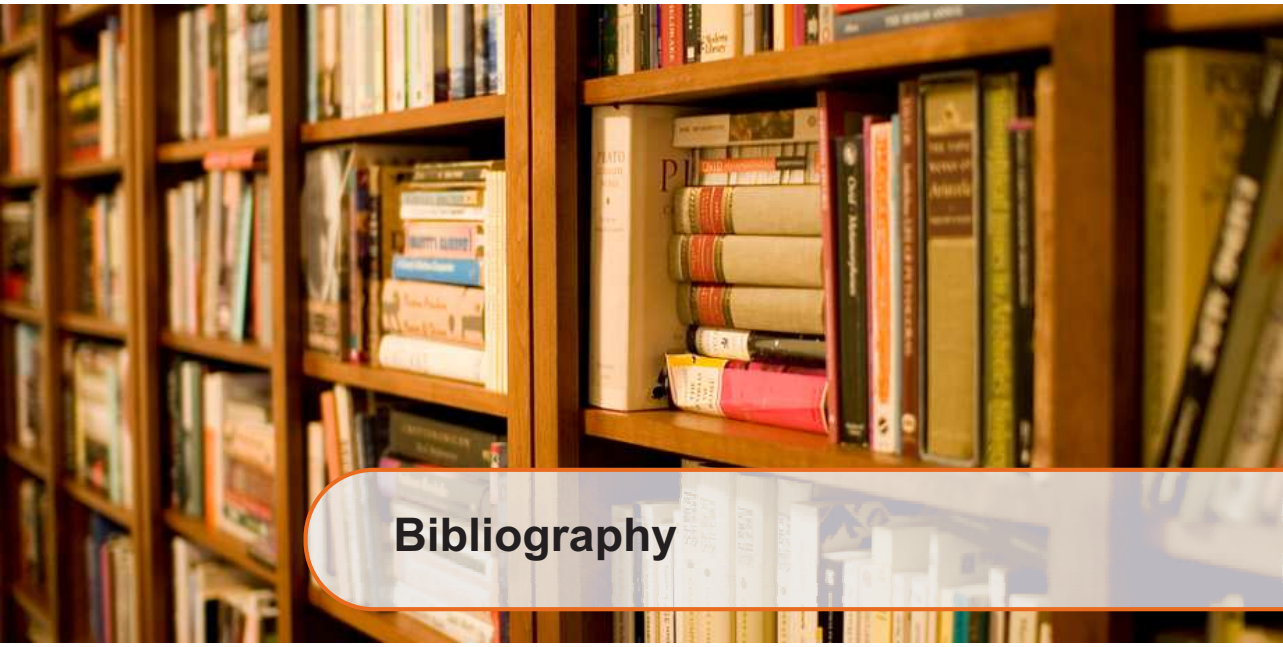

Bibliography

[1] Our Common Future, From One Earth to One World. Technical report, United Nations World Commission on Environment and Development, 1987.

[2] A Goetzberger and VU Hoffmann. *Photovoltaic Solar Energy Generation*. Springer, Berlin, first edit edition, 2005.

[3] DM Chapin, CS Fuller, and GL Pearson. A new Silicon p-n junction Photocell for Converting Solar Radiation into electrical Power. 54:676–677, 1954.

[4] NREL - National Center For Photovoltaics, Best Research-Cell Efficiencies, http://www.nrel.gov/ncpv/images/efficiency_chart.jpg (30.01.2014), 2014.

[5] DE Carlson and CR Wronski. Amorphous silicon solar cell. *Applied Physics Letters*, 28(11):671–673, 1976.

[6] J Meier, R Flückiger, H Keppner, and A Shah. Complete microcrystalline p-i-n solar cell - Crystalline or amorphous cell behavior ? *Applied Physics Letters*, 65(7):860–862, 1994.

[7] O Vetterl, F Finger, R Carius, P Hapke, L Houben, O Kluth, A Lambertz, A Mück, B Rech, and H Wagner. Intrinsic microcrystalline silicon: A new material for photovoltaics. *Solar Energy Materials and Solar Cells*, 62(1-2):97–108, April 2000.

[8] H Keppner, J Meier, P Torres, D Fischer, and A Shah. Microcrystalline silicon and micromorph tandem solar cells. *Applied Physics A: Materials Science & Processing*, 69(2):169–177, August 1999.

[9] K Yamamoto, T Suzuki, M Yoshimi, and A Nakajima. Optical Confinement Effect for below $5\mu\,m$ Thin Film Poly-Si Solar Cell on Glass Substrate. *Japanese Journal of Applied Physics*, 36:569–572, 1997.

[10] G Nakamura, K Sato, and Y Yukimoto. High Performance Tandem Type Amorphous Solar Cells. In *16th IEEE Photovolt. Specialist Conf.*, pages 1331–1337, New York, 1982.

[11] J Yang, A Banerjee, and S Guha. Triple-junction amorphous silicon alloy solar cell with 14.6% initial and 13.0% stable conversion efficiencies. *Appl. Phys. Lett.*, 70(22):2975–2977, 1997.

[12] D Cardwell and K Bradsher. U . S . Will Place Tariffs on Chinese Solar Panels, http://www.nytimes.com/2012/10/11/business/global/us-sets-tariffs-on-chinese-solar-panels.html?_r=0 (30.01.2014), 2012.

[13] U . S . looking into new dumping complaints on solar products from China, http://finance.yahoo.com/news/u-looking-dumping-complaints-solar-215506981.html (30.01.2014), 2014.

[14] A Shah, E Moulin, and C Ballif. Technological status of plasma-deposited thin-film silicon photovoltaics. *Solar Energy Materials and Solar Cells*, 119:311–316, December 2013.

[15] S Hänni, G Bugnon, G Parascandolo, M Boccard, J Escarré, M Despeisse, F Meillaud, and C Ballif. High-efficiency microcrystalline silicon single-junction solar cells. *Progress in Photovoltaics: Research and Applications*, 21(5):821–826, 2013.

[16] S Kim, JW Chung, H Lee, J Park, Y Heo, and HM Lee. Remarkable progress in thin-film silicon solar cells using high-efficiency triple-junction technology. *Solar Energy Materials and Solar Cells*, 119:26–35, December 2013.

[17] S Guha, J Yang, and B Yan. High efficiency multi-junction thin film silicon cells incorporating nanocrystalline silicon. *Solar Energy Materials and Solar Cells*, 119:1–11, December 2013.

[18] H Curtins, N Wyrsch, and A Shah. High-Rate Deposition of Amorphous Hydrogenated Silicon: Effect of Plasma Excitation Frequency. *Electronics Letters*, 23(5):228–230, 1987.

[19] F Finger, P Hapke, M Luysberg, R Carius, H Wagner, and M Scheib. Improvement of grain size and deposition rate of microcrystalline silicon. *Applied Physics Letters*, 65(20):2588–2590, 1994.

[20] J Meier, E Vallat-Sauvain, S Dubail, U Kroll, J Dubail, S Golay, L Feitknecht, P Torres, S Fay, D Fischer, and A Shah. Microcrystalline/micromorph silicon thin-film solar cells prepared by VHF-GD technique. *Solar Energy Materials and Solar Cells*, 66(1-4):73–84, February 2001.

[21] L Guo, M Kondo, M Fukawa, K Saitoh, and A Matsuda. High Rate Deposition of Microcrystalline Silicon Using Conventional Plasma-Enhanced Chemical Vapor Deposition. *Japanese Journal of Applied Physics*, 37(10):1116–1118, 1998.

[22] A Matsuda. Microcrystalline silicon. Growth and device application. *Journal of Non-Crystalline Solids*, 338-340:1–12, 2004.

[23] AA Howling, JL Dorier, C Hollenstein, U Kroll, and F Finger. Frequency effects in silane plasmas for plasma enhanced chemical vapor deposition. *Journal of Vacuum Science & Technology A: Vacuum, Surfaces, and Films*, 10(4):1080–1085, July 1992.

[24] F Finger, U Kroll, V Viret, A Shah, W Beyer, XM Tang, J Weber, AA Howling, and C Hollenstein. Influences of a high excitation frequency (70 MHz) in the glow discharge technique on the process plasma and the properties of hydrogenated amorphous silicon. *Journal of Applied Physics*, 71(11):5665–5674, 1992.

[25] C Beneking, F Finger, and H Wagner. Silane Deposition Plasma And Reactor Characterization In The VHF Range. In *11th E.C. Photovoltaic Solar Energy Conference*, pages 586–589, Montreux, 1992.

[26] W Schwarzenbach, AA Howling, M Fivaz, S Brunner, and C Hollenstein. Sheath impedance effects in very high frequency plasma experiments. *Journal of Vacuum Science & Technology A: Vacuum, Surfaces, and Films*, 14(1):132–138, January 1996.

[27] J Dutta, U Kroll, P Chabloz, A Shah, AA Howling, JL Dorier, and C Hollenstein. Dependence of intrinsic stress in hydrogenated amorphous silicon on excitation frequency in a plasma-enhanced chemical vapor deposition process. *Journal of Applied Physics*, 72(7):3220–3222, 1992.

[28] JL Dorier, C Hollenstein, AA Howling, and U Kroll. Powder dynamics in very high frequency silane plasmas. *Journal of Vacuum Science & Technology A: Vacuum, Surfaces, and Films*, 10(4):1048–1052, July 1992.

[29] M Kondo, M Fukawa, L Guo, and A Matsuda. High rate growth of microcrystalline silicon at low temperatures. *Journal of Non-Crystalline Solids*, 266-269:84–89, May 2000.

[30] EAG Hamers, WGJHM van Sark, J Bezemer, H Meiling, and WF van der Weg. Structural properties of a-Si:H related to ion energy distributions in VHF silane deposition plasmas. *Journal of Non-Crystalline Solids*, 226(3):205–216, June 1998.

[31] D Weaire and MF Thorpe. Electronic Properties of an Amorphous Solid. I.A Simple Tight-Binding Theory. *Physical Review B*, 4(8):2508–2520, 1971.

[32] F Bloch. Über die Quantenmechanik der Elekronen in Kristallgittern. *Zeitschrift für Physik A*, 52(7-8):555–600, 1928.

[33] RA Street. *Hydrogenated amorphous silicon*. Cambridge University Press, Cambridge, 1 edition, 1991.

[34] D Weaire. Existence of a Gap in the Electronic Density of States of a Tetrahedrally Bonded Solid of Arbitrary Structure. *Physical Review Letters*, 26(25):1541–1543, 1971.

[35] S Veprek and V Marecek. The preparation of thin layers of Ge and Si by chemical hydrogen plasma transport. *Solid-State Electronics*, 11:683–684, 1968.

[36] RW Collins and Yang; BY. In situ ellipsometry of thin-film deposition: Implications for amorphous and microcrystalline Si growth. *Journal of Vacuum Science & Technology B: Microelectronics and Nanometer Structures*, 7(5):1155–1164, September 1989.

[37] M Luysberg, C Scholten, L Houben, R Carius, F Finger, and O Vetterl. Structural properties of microcrystalline Si solar cells. *Materials Research Society*, 664:A15.2.1–A15.2.6, 2001.

[38] O Vetterl, A Gross, T Jana, S Ray, A Lambertz, R Carius, and F Finger. Changes in electric and optical properties of intrinsic microcrystalline silicon upon variation of the structural composition. *Journal of Non-Crystalline Solids*, 299-302:772–777, April 2002.

[39] AL Baia Neto, A Lambertz, R Carius, and F Finger. Relationships between structure, spin density and electronic transport in 'solar-grade' microcrystalline silicon films. *Journal of Non-Crystalline Solids*, 299-302:274–279, April 2002.

[40] S Veprek, Z Iqbal, RO Kühne, P Capezzuto, FA Sarott, and JK Gimzewski. Properties of microcrystalline silicon : IV . Electrical conductivity , electron spin resonance and the effect of gas adsorption. *Journal of Physics C: Solid State Physics*, 6241-6262(16):21, 1983.

[41] F Diehl, B Schröder, and H Oechsner. Light scattering and enhanced optical absorption in hot wire microcrystalline silicon. *Journal of Applied Physics*, 84(6):3416–3418, 1998.

[42] M Vanecek, A Poruba, Z Remes, N Beck, and M Nesladek. Optical properties of microcrystalline materials. *Journal of Non-Crystalline Solids*, 227-230(967-972):1–6, 1998.

[43] A Matsuda. Formation Kinetics And Control Of Microcrystallite In μc-Si:H From Glow Discharge Plasma. *Journal of Non-Crystalline Solids*, 59 & 60:767–774, 1983.

[44] CC Tsai, R Thompson, C Doland, A Ponce, GB Anderson, and B Wacker. Transition From Amorphous To Crystalline Silicon Effect Of Hydrogen On Film Growth. In *Mat. Res. Soc. Symp. Proc. Vol. 1181*, pages 49–54, 1988.

[45] CC Tsai, GB Anderson, R Thompson, and B Wacker. Control of Silicon Networks Structure in Plasma Deposition. *Journal of Non-Crystalline Solids*, 114:151–153, 1989.

[46] H Shirai, D Das, J Hanna, and I Shimizu. A novel preparation technique for preparing hydrogenated amorphous silicon with a more rigid and stable Si network. *Applied Physics Letters*, 59(9):1096–1098, 1991.

[47] K Nakamura, K Yoshino, S Takeoka, and I Shimizu. Roles of Atomic Hydrogen in Chemical Annealing. *Japan Journal of Applied Physics*, 34:442–449, 1995.

[48] DL Staebler and CR Wronski. Reversible conductivity changes in discharge-produced amorphous Si. *Applied Physics Letters*, 31(4):292–294, 1977.

[49] M Stutzmann, WB Jackson, and CC Tsai. Light-induced metastable defects in hydrogenated amorphous silicon: A systematic study. *Physical Review B*, 32(1):23–46, 1985.

[50] Y Wang, X Geng, H Stiebig, and F Finger. Stability of microcrystalline silicon solar cells with HWCVD buffer layer. *Thin Solid Films*, 516(5):733–735, 2008.

[51] P Würfel. *Physik der Solarzelle*. Spektrum Akademischer Verlag, Heidelberg, 1995.

[52] SM Sze and KNG Kwok. *Physics of semiconductor devices*. John Wiley & Sons, Hoboken, third edit edition, 2007.

[53] J Nelson. *The Physics Of Solar Cells*. Imperial College Press, London, 2003.

[54] A Gross, O Vetterl, A Lambertz, F Finger, H Wagner, and A Dasgupta. N-side illuminated microcrystalline silicon solar cells. *Applied Physics Letters*, 79(17):2841–2843, 2001.

[55] A Shah, J Dutta, N Wyrsch, K Prasad, H Curtins, F Finger, AA Howling, and C Hollenstein. VHF Plasma Depositions: A Comparative Overview. In *Mat. Res. Soc. Symp. Proc. Vol. 258*, pages 15–26, 1992.

[56] A Matsuda and T Goto. Role Of Surface And Growth-Zone Reactions In The Formation Process of μc-Si:H. *Mat. Res. Soc. Symp. Proc. Vol. 164*, 164:3–14, 1990.

[57] DL Flamm. Frequency effects in plasma etching. *J. Vac. Sci. Technol.*, 4(3):729–738, May 1986.

[58] M Moisan, R Barbeau, R Claude, CM Ferreira, J Margot, AB Paraszczak, G Sauve, and MR Wertheimer. Radio frequency or microwave plasma reactors? Factors determining the optimum frequency of operation. *Journal of Vacuum Science & Technology B: Microelectronics and Nanometer Structures*, 9(1):8–25, January 1991.

[59] H Curtins, N Wyrsch, M Favre, and AV Shah. Influence of plasma excitation frequency for a-Si:H thin film deposition. *Plasma Chemistry and Plasma Processing*, 7(3):267–273, September 1987.

[60] U Kroll, A Shah, H Keppner, J Meier, P Torres, and D Fischer. Potential of VHF-plasmas for low-cost production of a-Si: H solar cells. *Solar Energy Materials and Solar Cells*, 48(1-4):4559–4564, November 1997.

[61] CM Ferreira and J Loureiro. Electron energy distributions and excitation rates in high-frequency argon discharges. *J. Phys. D: Appl. Phys.*, 16:2471–2483, 1983.

[62] MR Wertheimer and M Moisan. Comparison of microwave and lower frequency plasmas for thin film deposition and etching. *Journal of Vacuum Science & Technology A: Vacuum, Surfaces, and Films*, 3(6):2643, November 1985.

[63] S Oda, J Noda, and M Matsumura. Diagnostic Study of VHF Plasma and Deposition of Hydrogenated Amorphous Silicon Films. *Japanese Journal of Applied Physics*, 29:1889–1895, 1990.

[64] M Heintze and R Zedlitz. VHF Plasma Deposition for Thin-film Solar Cells. *Progress in Photovoltaics: Research and Applications*, 1:213–224, 1993.

[65] M Heintze, R Zedlitz, and GH Bauer. Analysis of high-rate a-Si:H deposition in a VHF plasma. *Power*, 26:1781–1786, 1993.

[66] K Köhler, DE Horne, and JW Coburn. Frequency dependence of ion bombardment of grounded surfaces in rf argon glow discharges in a planar system. *Journal of Applied Physics*, 58(9):3350, 1985.

[67] L Sansonnens and J Schmitt. Shaped electrode and lens for a uniform radio-frequency capacitive plasma. *Applied Physics Letters*, 82(2):182–184, 2003.

[68] J Kuske, U Stephan, O Steinke, and S Röhlecke. Power Feeding In Large Area PECVD Of Amorphous Silicon. *Mat. Res. Soc. Symp. Proc. Vol. 377*, 1:27–32, 1995.

[69] T Zimmermann, T Merdzhanova, M Meier, and A Gordijn. Dynamic deposition of microcrystalline silicon. *SPIE Newsroom*, 0:1–3, 2013.

[70] JK Rath, RHJ Franken, A Gordijn, REI Schropp, and WJ Goedheer. Growth mechanism of microcrystalline silicon at high pressure conditions. *Journal of Non-Crystalline Solids*, 338-340:56–60, June 2004.

[71] A Gordijn, M Vanecek, WJ Goedheer, JK Rath, and REI Schropp. Influence of Pressure and Plasma Potential on High Growth Rate Microcrystalline Silicon Grown by Very High Frequency Plasma Enhanced Chemical Vapour Deposition. *Japanese Journal of Applied Physics*, 45(8A):6166–6172, 2006.

[72] U Graf, J Meier, U Kroll, J Bailat, C Droz, E Vallat-Sauvain, and A Shah. High rate growth of microcrystalline silicon by VHF-GD at high pressure. *Solar Energy Materials and Solar Cells*, 427(1-2):37–40, March 2003.

[73] G Parascandolo, G Bugnon, A Feltrin, and C Ballif. High-rate deposition of microcrystalline silicon in a large-area PECVD reactor and integration in tandem solar cells. *Progress in Photovoltaics: Research and Applications*, 18:257–264, 2010.

[74] T Matsui, M Kondo, and A Matsuda. Origin of the Improved Performance of High-Deposition-Rate Microcrystalline Silicon Solar Cells by High-Pressure Glow Discharge. *Japanese Journal of Applied Physics*, 42(8A):L901–L903, August 2003.

[75] AHM Smets, T Matsui, and M Kondo. High-rate deposition of microcrystalline silicon p-i-n solar cells in the high pressure depletion regime. *Journal of Applied Physics*, 104(3):034508/1–034508/11, 2008.

[76] A Lambertz, O Vetterl, and F Finger. High Deposition Rate For μc-Si:H Absorber Layers Using VHF PECVD At Elevated Discharge Power And Deposition Pressure. In *17th EC PVSEC*, pages 2977–2981, Munich, 2001.

[77] Y Mai, S Klein, X Geng, and F Finger. Structure adjustment during high-deposition-rate growth of microcrystalline silicon solar cells. *Applied Physics Letters*, 85(14):2839–2841, 2004.

[78] Y Mai, S Klein, R Carius, J Wolff, A Lambertz, F Finger, and X Geng. Microcrystalline silicon solar cells deposited at high rates. *Journal of Applied Physics*, 97(11):114913.1–114913.12, 2005.

[79] A Gordijn, A Pollet-Villard, and F Finger. At the limit of total silane gas utilization for preparation of high-quality microcrystalline silicon solar cells at high-rate plasma deposition. *Applied Physics Letters*, 98(21):211501/1–211501/3, 2011.

[80] B Strahm, AA Howling, L Sansonnens, and C Hollenstein. Plasma silane concentration as a determining factor for the transition from amorphous to microcrystalline silicon in SiH_4/H_2 discharges. *Plasma Sources Science and Technology*, 16(1):80–89, February 2007.

[81] F Paschen. Ueber die zum Funkenübergang in Luft, Wasserstoff und Kohlensäure bei verschiedenen Drucken erforderliche Potentialdifferenz. *Annalen der Physik*, 273:69–96, 1889.

[82] T Kilper, T Repmann, B Rech, G Bräuer, and S Wieder. Development Of Microcrystalline Silicon Solar Cells Using Large Area Capacitively Coupled Planar Electrodes. In *20th European PVSEC*, pages 1544–1547, Barcelona, 2005.

[83] F Meillaud, A Billet, C Battaglia, M Boccard, P Cuony, M Despeisse, L Ding, J Escarre-palou, H Simon, L Linus, S Nicolay, G Parascandolo, M Stückelberger, and C Ballif. Latest Developments of High-Efficiency Micromorph Tandem Silicon Solar Cells Implementing Innovative Substrate Materials and Improved Cell Design. *IEEE Journal of Photovoltaics*, 2(3):236–240, 2012.

[84] S Oda. Frequency effects in processing plasmas of the VHF band. *Plasma Sources Sci. Technol.*, 2(26):26–29, 1993.

[85] S Michard. *Entwicklung und Herstellung von Siliziumschichten und Schichtsystemen zur Applikation in Dünnfilm-Solarzellen durch Einsatz eines innovativen Clustertool Depositionssystems*. Diploma thesis, RWTH Aachen, 2011.

[86] B Bayindirli. *In-Situ Temperature Measurements in CVD Processes for Silicon Thin Film Solar Cells*. Master thesis, FH Aachen University of Applied Sciences, 2013.

[87] A Gordijn, A Pollet-Villard, MN van Den Donker, J Wolff, and F Finger. Influence of the gas flow geometry on the performance of microcrystalline silicon p-i-n solar cells. In *22nd EUPVSEC-Milan*, Milan, 2007.

[88] B Chapman. *Glow discharge processes : sputtering and plasma etching*. Wiley-Interscience, New York, 1980.

[89] MA Lieberman and AJ Lichtenberg. *Principles of Plasma Discharges And Materials Processing*. John Wiley & Sons, Hoboken, 2 edition, 2005.

[90] K Tanaka and A Matsuda. Glow-Discharge Amorphous Silicon: Growth Process And Structure. *Materials Reports 2*, 139-184:139–182, 1987.

[91] S Veprek, FA Sarrott, S Rambert, and E Taglauer. Surface hydrogen content and passivation of silicon deposited by plasma induced chemical vapor deposition from silane and the implications for the reaction mechanism. *J. Vac. Sci. Technol.*, A7(4):2614–2624, 1989.

[92] S Veprek and M Heintze. The Mechanism of Plasma-Induced Deposition of amorphous Silicon from Silane. *Plasma Chemistry and Plasma Processing*, 10(1):3–26, 1990.

[93] P Roca i Cabarrocas. Plasma enhanced chemical vapor deposition of amorphous, polymorphous and microcrystalline silicon films. *Journal of Non-Crystalline Solids*, 269-299:31–37, 2000.

[94] H Wiesmann, AK Ghosh, T McMahon, and M Strongin. a-Si : H produced by high-temperature thermal decomposition of silane. *Journal of Applied Physics*, 50(5):3752–3754, 1979.

[95] H Matsumura and H Tachibana. Amorphous silicon produced by a new thermal chemical vapor deposition method using intermediate species SiF_2. *Applied Physics Letters*, 47(8):833–835, 1985.

[96] H Matsumura. Formation of Polysilicon Films by Catalytic Chemical Vapor Deposition (cat-CVD) Method. *Japan Journal of Applied Physics*, 30(8B):1522–1524, 1991.

[97] JK Rath, H Meiling, and REI Schropp. Low-temperature deposition of polycrystalline silicon thin films by hot-wire CVD. *Solar Energy Materials and Solar Cells*, 48(1-4):269–277, November 1997.

[98] S Klein, F Finger, R Carius, T Dylla, B Rech, M Grimm, L Houben, and M Stutzmann. Intrinsic microcrystalline silicon prepared by hot-wire chemical vapour deposition for thin film solar cells. *Thin Solid Films*, 430(1-2):202–207, April 2003.

[99] Y Mai, S Klein, R Carius, H Stiebig, X Geng, and F Finger. Open circuit voltage improvement of high-deposition-rate microcrystalline silicon solar cells by hot wire interface layers. *Applied Physics Letters*, 87(7):073503.1–073503.3, 2005.

[100] T Chen, Y Huang, D Yang, R Carius, and F Finger. Microcrystalline silicon-carbon alloys as anti-reflection window layers in high efficiency thin film silicon solar cells. *physica status solidi (RRL) - Rapid Research Letters*, 2(4):160–162, August 2008.

[101] T Chen, D Yang, R Carius, and F Finger. Highly Conductive p-Type Silicon Carbon Alloys Deposited by Hot-Wire Chemical Vapor Deposition. *Japanese Journal of Applied Physics*, 49(4):041303/1–041303/6, April 2010.

[102] A Gallagher. Some physics and chemistry of hot-wire deposition. *Thin Solid Films*, 395(1-2):25–28, September 2001.

[103] H Matsumura. Formation of Silicon-Based Thin Films Prepared by Catalytic Chemical Vapor Deposition (Cat-CVD) Method. *Japan Journal of Applied Physics*, 37:3175–3187, 1998.

[104] EAG Hamers, A Fontcuberta i Morral, C Niikura, R Brenot, and P Roca i Cabarrocas. Contribution of ions to the growth of amorphous, polymorphous, and microcrystalline silicon thin films. *Journal of Applied Physics*, 88(6):3674–3688, 2000.

[105] S Klein. *Microcrystalline Silicon Prepared by Hot Wire CVD*. PhD thesis, Technische Universität München, München, 2003.

[106] O Kluth. *Texturierte Zinkoxidschichten für Silizium-Dünnschichtsolarzellen*. Berichte des Forschungszentrums Jülich; Band 3928, Jülich, 2001.

[107] CV Raman and KS Krishnan. A new Type of Secondary Radiation. *Nature*, 121(3048):501–502, 1928.

[108] CV Raman. A Change of Wave-length in Light Scattering. *Nature*, 121(3051):619, 1928.

[109] M Cardona and G Güntherodt. *Light Scattering in Solids VII - Fullerenes, Semiconductor, Surfaces, Coherent Phonons*. Springer, Berlin, 8 edition, 2000.

[110] PY Yu and M Cardona. *Fundamentals of Semiconductors - Physics and Material Properties*. Springer, 4 edition, 2010.

[111] H Richter. *Elektronen und Photonen in mikrokristallinem Silizium*. PhD thesis, Universität Stuttgart, 1983.

[112] RJ Kobliska and SA Solin. Raman Spectrum of Wurtzite Silicon. *Physical Review B*, 8(8):3799–3802, 1973.

[113] F Köhler, S Schicho, B Wolfrum, A Gordijn, SE Pust, and R Carius. Gradient etching of silicon-based thin films for depth-resolved measurements: The example of Raman crystallinity. *Thin Solid Films*, 520(7):2605–2608, January 2012.

[114] P Hapke. *VHF-Plasmaabscheidung von mikrokristallinem Silizium(uc-Si:H): Einfluss der Plasmaanregungsfrequenz auf die strukturellen und elektrischen Eigenschaften*. PhD thesis, Rheinisch-Westfälische Technische Hochschule Aachen, Aachen, 1995.

[115] H Wagner and W Beyer. Reinterpretation of the silicon-hydrogen stretch frequencies in amorphous silicon. *Solid State Communications*, 48(7):585–587, 1983.

[116] G Lucovsky, J Yang, SS Chao, JE Tyler, and W Czubatyj. Oxygen-bonding enviroments in glow-discharge-deposited amorphous silicon-hydrogen alloy films. *Physical Review B*, 28(6):3225–3233, 1983.

[117] W Beyer and MS Abo Ghazala. Absoprtion strengths of Si-H vibrational modes in hydrogenated silicon. In *Mat. Res. Soc. Symp. Proc. Vol. 507*, pages 601–606. Materials Research Society, 1998.

[118] M Pinarbasi, N Maley, MJ Kushner, A Myers, JR Abelson, and JA Thornton. Effect of hydrogen on the microstructural, optical, and electronic properties of a-Si:H thin films deposited by direct current magnetron reactive sputtering. *J. Vac. Sci. Technol.*, 7(3):1210–1214, May 1989.

[119] CJ Fang, KJ Gruntz, L Ley, M Cardona, FJ Demond, G Müller, and S Kalbitzer. The Hydrogen Content Of a-Ge:H And a-Si:H As Determined by IR Spetroscopy, Gas Evolution And Nuclear Reaction Techniques. *Journal of Non-Crystalline Solids*, 35&36:255–260, 1980.

[120] AA Langford, ML Fleet, BP Nelson, WA Lanford, and N Maley. Infrared absorption strength and hydrogen content of hydrogenated amorphous silicon. *Physical Review B*, 45(23):13367–13377, 1992.

[121] N Maley. Critical Investigation Of the Infrared-Transmission-Data Analysis Of Hydrogenated Amorphous Silicon Alloys. *Physical Review B*, 46(4):2078–2085, 1992.

[122] M Stutzmann, MS Brandt, and MW Bayerl. Spin-dependent processes in amorphous and microcrystalline silicon: a survey. *Journal of Non-Crystalline Solids*, 266-269:1–22, May 2000.

[123] K Lips, M Fehr, and J Behrends. Electron-Spin Resonance (ESR) in Hydrogenated Amorphous Silicon (a-Si:H). In D Abou-Ras, T Kirchartz, and U Rau, editors, *Advanced Characterization Techniques for Thin Film Solar Cells*. Wiley-VCH, Weinheim, 2011.

[124] F Finger, C Malten, P Hapke, R Carius, R Flückiger, and H Wagner. Free electrons and defects in microcrystalline silicon studied by electron spin resonance. *Philosophical Magazine Letters*, 70(4):247–254, October 1994.

[125] F Finger, J Müller, C Malten, R Carius, and H Wagner. Electronic properties of microcrystalline silicon investigated by electron spin resonance and transport measurements. *Journal of Non-Crystalline Solids*, 266-269:511–518, May 2000.

[126] O Astakhov, R Carius, F Finger, Y Petrusenko, V Borysenko, and D Barankov. Relationship between defect density and charge carrier transport in amorphous and microcrystalline silicon. *Physical Review B*, 79(10):104205/1–104205/14, March 2009.

[127] C Malten. *Pulsed Electron Spin Resonance of Amorphous and Microcrystalline Semiconductors*. Berichte des Forschungszentrums Jülich; 3273, Jülich, 1996.

[128] L Xiao, O Astakhov, and F Finger. Silicon Thin Film Powder Samples for Electron Spin Resonance Investigation: Role of Substrate and Preparation Procedure. *Japanese Journal of Applied Physics*, 50(7):071301\1–071301\7, July 2011.

[129] L Spieß, G Teichert, R Schwarzer, H Behnken, and C Genzel. *Moderne Röntgenbeugung*. Vieweg + Teubner, Wiesbaden, 2 edition, 2009.

[130] F Köhler. *Zur Mikrostruktur siliziumbasierter Dünnschichten für die Photovoltaik*. Forschungszentrum Jülich; Reihe Energie & Umwelt Band 176, Jülich, 2012.

[131] A Rosenauer. *Transmission Electron Microscopy of Semiconductor Nanostructures*. Springer-Verlag, Berlin, 2003.

[132] L Houben. *Plasmaabscheidung von mikrokristallinem Silizium: Merkmale und Mikrostruktur und deren Deutung im Sinne von Wachstumsvorgängen*. Berichte des Forschungszentrums Jülich; Band 3753, Jülich, 1999.

[133] Anna Heidt. *Lokale strukturelle und elektronische Eigenschaften mikrokristalliner Siliziumkarbidverbindungen für die Dünnschichtphotovoltaik*. PhD thesis, RWTH Aachen, 2013.

[134] D Briggs, A Brown, and JC Vickerman. Handbook of Static Secondary Ion Mass Spectrometry, 1989.

[135] F Reniers and CR Tewell. In-Depth Analysis/Profiling. In JC Riviere and S Myhra, editors, *Handbook of Surface and Interface Analysis - Methods for Problem-Solving*, chapter 10. Taylor & Francis Group, Boca Raton, 2 edition, 2009.

[136] A Mück, U Zastrow, O Vetterl, and B Rech. SIMS depth profile analysis of oxygen contamination in hydrogenated amorphous and microcrystalline silicon. In A Benninghoven, P Bertrand, HN Migeon, and HW Werner, editors, *Secondary Ion Mass Spetrometry - SIMS XII*, pages 689–693, Amsterdam, 2000.

[137] U Zastrow and S Michard. Dimer Formation Probability in Sputter Depth Profiling : Influence of laterally inhomogeneous Element Distribution on nm-Scale. In *Particle - surface interactions: from surface analysis to materials processing, PASI 2013*, volume 77, Luxembourg, 2013.

[138] T Repmann. *Stapelsolarzellen aus amorphem und mikrokristallinem Silizium*. Berichte des Forschungszentrums Jülich; 4082, Jülich, 2003.

[139] W Reetz, H Stiebig, T Brammer, B Rech, J Fölsch, and H Wagner. Spectral Response of Stacked Solar Celles Based on a-Si:H. In *2th ISEC-Europe Solar Congress*, Portoroz, 1998.

[140] J Metzdorf. Calibration of solar cells. 1: The differential spectral responsivity method. *Applied Optics*, 26(9):1701–1708, 1987.

[141] W Luft, B von Roedern, B Stafford, and L Mrig. Second Controlled Light-Soaking Experiment For Amorphous Silicon Modules. In *23rd IEEE Photovoltaic Specialist Conference*, number April 1992, pages 860–866, Louisville, 1993.

[142] JK Rath. Low temperature polycrystalline silicon: a review on deposition, physical properties and solar cell applications. *Solar Energy Materials and Solar Cells*, 76(4):431–487, April 2003.

[143] A Matsuda. Growth mechanism of microcrystalline silicon obtained from reactive plasmas. *Thin Solid Films*, 337:1–6, 1999.

[144] MN van den Donker. *Plasma Deposition of Microcrystalline Silicon Solar Cells: Looking Beyond the Glass*. Number december. Forschungszentrum Jülich, Jülich, schriften edition, 2006.

[145] F Finger, S Klein, T Dylla, AL Baia Neto, O Vetterl, and R Carius. Defects in microcrystalline silicon prepared with Hot Wire CVD. In *Mat. Res. Soc. Symp. Proc. Vol. 715*, pages A16.3.1–A16.3.12. 715, 2002.

[146] T Dylla. *Electron Spin Resonance and Transient Photocurrent Measurements on Microcrystalline Silicon*. Schriften des Forschungszentrums Jülich; Reihe Energietechnik Band 43, Jülich, 2005.

[147] G Bugnon, A Feltrin, F Meillaud, J Bailat, and C Ballif. Influence of pressure and silane depletion on microcrystalline silicon material quality and solar cell performance. *Journal of Applied Physics*, 105(6):064507/1–064507/7, 2009.

[148] R Schropp and M Zeman. *Amorphous and microcrystalline silicon solar cells*. Kluwer Academic Publishers, London, 1998.

[149] Y Mai. *Microcrystalline silicon layers for thin film solar cells prepared with Hot Wire Chemical Vapour Deposition and Plasma enhanced Chemical vapour Deposition*. Berichte des Forschungszentrums Jülich; 4254, Jülich, 2006.

[150] M Sendova-Vassileva, F Finger, S Klein, and A Lambertz. Impact of instability in μc-Si:H i-layers on the performance of solar cells. *Journal of Optoelectronics and Advanced Materials*, 7(1):481–484, 2005.

[151] F Finger, R Carius, T Dylla, S Klein, S Okur, and M Günes. Stability of microcrystalline silicon for thin film solar cell applications. *IEE Proceedings*, 150(4):300–308, 2003.

[152] V Smirnov, S Reynolds, C Main, F Finger, and R Carius. Aging effects in microcrystalline silicon films studied by transient photoconductivity. *Journal of Non-Crystalline Solids*, 338-340:421–424, June 2004.

[153] M Günes, H Cansever, G Yilmaz, V Smirnov, F Finger, and R Brüggemann. Metastability effects in hydrogenated microcrystalline silicon thin films investigated by the dual beam photoconductivity method. *Journal of Non-Crystalline Solids*, 358(17):2074–2077, September 2012.

[154] M Sendova-Vassileva, S Klein, A Lambertz, and F Finger. Stability of Microcrystalline Solar Cells Under Treatment In Water, Air And Vacuum. In *19th European Photovoltaic Solar Energy Conference*, pages 1423–1426, Paris, 2004.

[155] JA Kilner, BCH Steele, and L Ilkov. Oxygen Self-Diffusion Studies Using Negative-Ion Secondary Ion Mass Spectrometry (SIMS). *Solid State Ionics*, 12:89–97, 1984.

[156] U Zastrow, K Szot, W Beyer, and W Speier. Depth Profiling of ^{18}O Tracer Diffusion In $SrTiO_3$ Using O_2^- Secondary Ion Detection. In *Secondary Ion Mass Spetrometry - SIMS XI*, pages 393–396, Orlando, 1998.

[157] K Wang, D Han, DL Williams, B Huie, JR Weinberg-Wolf, B Yan, J Yang, and S Guha. Structural and Electronic Properties of Hydrogenerated Nanocrystalline Silicon Films Made with Hydrogen Dilution Profiling Technique. In *Mater. Res. Soc. Symp. Proc. Vol. 862*, pages 117–122, 2005.

[158] L Houben, M Luysberg, and R Carius. Microtwinning in microcrystalline silicon and its effect on grain-size measurements. *Physical Review B*, 67:045312/1–045312/10, January 2003.

[159] I De Wolf. Micro-Raman spectroscopy to study local mechanical stress in silicon integrated circuits. *Semiconductor Science and Technology*, 11(2):139–154, February 1996.

[160] U Kroll, J Meier, A Shah, S Mikhailov, and J Weber. Hydrogen in amorphous and microcrystalline silicon films prepared by hydrogen dilution. *Japanese Journal of Applied Physics*, 80(9):4971–4975, 1996.

[161] W Beyer and H Wagner. The Role Of Hydrogen In a-Si:H - Results Of Evolution And Annealing Studies. *Journal of Non-Crystalline Solids*, 59&60:161–168, 1983.

[162] F Finger, R Carius, T Dylla, S Klein, S Okur, and M Günes. Instability Phenomena In Microcrystalline Silicon Films. *Journal of Optoelectronics and Advanced Materials*, 7(1):83–90, 2005.

[163] T Matsui, M Tsukiji, H Saika, T Toyama, and H Okamoto. Correlation between Microstructure and Photovoltaic Performance of Polycrystalline Silicon Thin Film Solar Cells. *Japanese Journal of Applied Physics*, 41:20–27, 2002.

[164] T Matsui, M Tsukiji, H Saika, T Toyama, and H Okamoto. Influence of substrate texture on microstructure and photovoltaic performances of thin film polycrystalline silicon solar cells. *Journal of Non-Crystalline Solids*, 299-302:1152–1156, April 2002.

[165] E Vallat-Sauvain, U Kroll, J Meier, A Shah, and J Pohl. Evolution of the microstructure in microcrystalline silicon prepared by very high frequency glow-discharge using hydrogen dilution. *Journal of Applied Physics*, 87(6):3137–3142, 2000.

[166] T Sugano, T Kitagawa, Y Sobajima, T Toyama, and H Okamoto. Hybrid-phase growth in microcrystalline silicon thin films deposited by plasma enhanced chemical vapor deposition at low temperatures. *Journal of Applied Physics*, 97(9):094910/1–094910/6, 2005.

[167] S Schicho. *Amorphous and microcrystalline silicon applied in very thin tandem solar cells*. Jülich, 2011.

[168] S Schicho, F Köhler, R Carius, and A Gordijn. The relationship of structural properties of microcrystalline silicon to solar cell performance. *Solar Energy Materials and Solar Cells*, 98:391–397, March 2012.

[169] M Kondo, Y Toyoshima, A Matsuda, and K Ikuta. Substrate dependence of initial growth of microcrystalline silicon in plasma-enhanced chemical vapor deposition. *Journal of Applied Physics*, 80(10):6061–6063, 1996.

[170] M Tzolov, F Finger, R Carius, and P Hapke. Optical and transport studies on thin microcrystalline silicon films prepared by very high frequency glow discharge for solar cell applications. *Journal of Applied Physics*, 81(11):7376–7385, 1997.

[171] E Amanatides, E Katsia, D Mataras, A Soto, and GA Voyiatzis. Temperature effect and stress on microcrystalline silicon thin films deposited under high pressure plasma conditions. *Thin Solid Films*, 511-512:603–607, 2006.

[172] Z Iqbal, S Veprek, AP Webb, and P Capezzuto. Raman Scattering From Small Particle Size Polycrystalline Silicon. *Solid State Communications*, 37(1980):993–996, 1981.

[173] Z Iqbal and S Veprek. Raman scattering from hydrogenated microcrystalline and amorphous silicon. *Journal of Physics C: Solid State Physics*, 15:377–392, 1982.

[174] V Paillard, P Puech, and P Roca i Cabarrocas. Measurement of stress gradients in hydrogenated microcrystalline silicon thin films using Raman spectroscopy. *Journal of Non-Crystalline Solids*, 299-302:280–283, April 2002.

[175] RB Wehrspohn, SC Deane, ID French, I Gale, J Hewett, MJ Powell, and J Robertson. Relative importance of the Si–Si bond and Si–H bond for the stability of amorphous silicon thin film transistors. *Journal of Applied Physics*, 87(1):144–154, 2000.

[176] T Iida, T Itoh, D Noguchi, Y Takanashi, Y Takano, and Y Kanda. Residual lattice strain in thin silicon-on-insulator bonded wafers: Effects on electrical properties and Raman shifts. *Journal of Applied Physics*, 89(4):2109–2114, 2001.

[177] M Stutzmann. Role of mechanical stress in the light-induced degradation of hydrogenated amorphous silicon. *Applied Physics Letters*, 47(1):21–23, 1985.

[178] T Matsui, C Chang, M Kondo, K Ogata, and M Isomura. Effect of illumination-induced space charge on photocarrier transport in hydrogenated microcrystalline $Si_{1-x}Ge_x$ p-i-n solar cells. *Applied Physics Letters*, 91(10):102111/1–102111/3, 2007.

[179] IH Campbell and PM Fauchet. The Effects of Microcrystal Size And Shape On The One Phonon Raman Spectra Of Crystalline Semiconductors. *Solid State Communications*, 58(10):739–741, 1986.

[180] PM Fauchet and IH Campbell. Critical Review Of Raman Spectroscopy As A Diagnostic Tool For Semiconductor Microcrystals. In *Mat. Res. Soc. Symp. Proc. Vol. 184*, pages 259–264, 1990.

[181] M Python, E Vallat-Sauvain, J Bailat, D Dominé, L Fesquet, A Shah, and C Ballif. Relation between substrate surface morphology and microcrystalline silicon solar cell performance. *Journal of Non-Crystalline Solids*, 354(19-25):2258–2262, May 2008.

[182] M Python, O Madani, D Dominé, F Meillaud, E Vallat-Sauvain, and C Ballif. Influence of the substrate geometrical parameters on microcrystalline silicon growth for thin-film solar cells. *Solar Energy Materials and Solar Cells*, 93(10):1714–1720, October 2009.

[183] REI Schropp. Present status of micro- and polycrystalline silicon solar cells made by hot-wire chemical vapor deposition. *Thin Solid Films*, 451-452:455–465, March 2004.

[184] SRIM webpage: http://www.srim.org (18.01.2014), 2014.

[185] JF Ziegler, JP Biersack, and U Littmark. *The Stopping And Range Of Ions In Solids*. Pergamon Press, Inc, New York, 1985.

[186] JF Ziegler. SRIM-2003. *Nuclear Instruments and Methods in Physics Research Section B: Beam Interactions with Materials and Atoms*, 219-220:1027–1036, June 2004.

[187] JF Ziegler, MD Ziegler, and JP Biersack. SRIM – The stopping and range of ions in matter (2010). *Nuclear Instruments and Methods in Physics Research Section B: Beam Interactions with Materials and Atoms*, 268(11-12):1818–1823, June 2010.

[188] AC Bronneberg, X Kang, J Palmans, PHJ Janssen, T Lorne, M Creatore, and MCM van de Sanden. Direct ion flux measurements at high-pressure-depletion

conditions for microcrystalline silicon deposition. *Journal of Applied Physics*, 114(6):063305/1–063305/6, 2013.

[189] G Bugnon, A Feltrin, R Bartlome, B Strahm, AC Bronneberg, G Parascandolo, and C Ballif. Microcrystalline and micromorph device improvements through combined plasma and material characterization techniques. *Solar Energy Materials and Solar Cells*, 95(1):134–137, January 2011.

[190] Y Mai, S Klein, R Carius, and H Stiebig. Open circuit voltage improvement of high-deposition-rate microcrystalline silicon solar cells by hot wire interface layers. *Applied Physics Letters*, 87, 2005.

[191] F Finger, Y Mai, S Klein, and R Carius. High efficiency microcrystalline silicon solar cells with Hot-Wire CVD buffer layer. *Thin Solid Films*, 516(5):625, 2008.

[192] K Wittmaack. Analytical description of the sputtering yields of silicon bombarded with normally incident ions. *Physical Review B*, 68:235211/1–235211/11, 2003.

[193] ZQ Ma, YF Zheng, and BX Liu. Ion-Induced Surface and Bulk Displacement Threshold for Epitaxial Growth. *Physica Status Solidi (a)*, 169(2):239–248, October 1998.

[194] M Bonnet-Eymard, M Boccard, G Bugnon, F Sculati-Meillaud, M Despeisse, and C Ballif. Optimized short-circuit current mismatch in multi-junction solar cells. *Solar Energy Materials and Solar Cells*, 117:120–125, October 2013.

[195] B Blank, C Ulbrich, C Zahren, BE Pieters, A Gerber, and U Rau. Optimization of the Stabilized Efficiency of Thin-Film Tandem Solar Cells through Power Matching. In *28th European Photovoltaic Solar Energy Conference and Exhibition*, pages 2218–2221, Paris, 2013.

[196] TEL Solar Switzerland. TEL solar webpage: http://www.solar.tel.com/products-solutions/turnkey-solutions/ (04.11.2013), 2013.

[197] S Haas. *Untersuchung und Optimierung der Serienverschaltung von Silizium-Dünnschicht-Solarmodulen*. Schriften des Forschungszentrums Jülich; Reihe Energie & Umwelt Band 91, Jülich, 2010.

Publications List

Publications as first author

- S Michard, M Meier, U Zastrow, O Astakhov, F Finger. Investigation of porosity and atmospheric gas diffusion in microcrystalline silicon fabricated at high growth rates. Canadian Journal of Physics, 92 (999), 1-4, 2013.
- S Michard, V Balmes, M Meier, A Lambertz, T Merdzhanova, F Finger. Microcrystalline silicon absorber layers prepared at high deposition rates for thin-film tandem solar cells. European Physical Journal Photovoltaics, 4, 45201/p1 - 45201/p6 ,2013.
- S Michard, M Meier, B Grootoonk, O Astakhov, A Gordijn, F Finger. High deposition rate processes for the fabrication of microcrystalline silicon thin films. Materials Science and Engineering: B, 178, 691 - 694, 2013.

Publications as co-author

- S Reynolds, S Michard, S Wang, V Smirnov. Electronic properties of undoped microcrystalline silicon oxide films. Canadian Journal of Physics, 2014 (in press).
- M Meier, UW Paetzold, M Ghosh, W Zhang, T Merdzhanova, G Jost, S Michard, A Gordijn. Fabrication of Light-Scattering Multiscale Textures by Nanoimprinting for the Application of Thin-Film Silicon Solar Cells. IEEE Journal of Photovoltaics, 4(3), 772-777, 2014.
- UW Paetzold, W Zhang, M Prömpers, J Kirchhoff, T Merdzhanova, S Michard, R Carius, A Gordijn, M Meier. Thin-film silicon solar cell development on imprint-textured glass substrates. Materials Science and Engineering: B, 178, 617 - 622, 2013.
- D König, D Hiller, M Zacharias, S Michard, C Flynn. Static hot carrier populations as a function of optical excitation energy detected through energy selective contacts by optically assisted IV. Progress in Photovoltaics: Research and Applications, 2013.

thx . . .

Acknowledgments

I would like to express the deepest appreciation to Professor Rau for giving me the possibility to pursue my research at the research center in Jülich. I am thankful for his support, for valuable and intense discussions and for his interest in my work.

I thank Professor Knoch for kindly accepting to report on my thesis.

I am deeply grateful to Dr. Friedhelm Finger for his guidance, his leadership, for giving me the opportunity to pursue my research with the greatest possible freedom. His constructive comments and encouragements helped me to improve my personal skills, my publications, and the present work.

I thank Dr. Matthias Meier for being such a tremendous mentor for me, for encouraging my research and for allowing me to grow as a research scientist. His good advice, support, and friendship has been invaluable on both an academic and a personal level.

I would particularly like to thank Dr. Steve Reynolds for intense discussions and for his hospitality during my visits at the University of Dundee. These journeys were clearly highlights during my time as a PhD researcher.

I thank Drs. Gordijn, Smirnov, Astakhov, Köhler, and Chen for many rewarding discussion.

I admire Andreas Lambertz's energy, passion, and creativity with respect to research on thin-film silicon. He was always open to share his experience he gained over more than ten years and helped me to move forward.

Special thanks to Andreas Schmalen and Johannes Wolff for excellent technical support. Their immense experience helped to tackle every technical challenge.

For scientific discussions as well as for discussions of general nature I thank Drs. Aeberhard, Augarten, Paetzold, and Merdzhanova.

I am grateful for the assistance given by Andreas Bauer, Ulrike Gerhards, Markus Hülsbeck, Josef Klomfaß, Sandra Moll, Andrea Mülheims, Hilde Siekmann, and Janine Worbs.

For pursuing various interesting side projects as well as for social activities I thank Nicolas Sommer and Bugra Turan.

I thank Horst Windgassen for his friendship.

I thank Liesel and Bernd Stalz as well as Pascal and Elisabeth Michard for constant support and encouragement throughout my studies and my time as a PhD researcher.

Mes dernières pensées vont vers Linda Michard qui m'a soutenue dès le début, qui m'a aidé dans les périodes de doute, qui me fait rire, et qui me change les idées de temps en temps. Merci!

Band / Volume 246
Nanostructured Si-alloys for silicon solar cells
K. Ding (2015), 210 pp
ISBN: 978-3-95806-024-1

Band / Volume 247
Electrochemical Texturing and Deposition of Transparent Conductive Oxide Layers for the Application in Silicon Thin-Film Solar Cells
J.-P. Becker (2015), ix, 156, XXIV pp
ISBN: 978-3-95806-027-2

Band / Volume 248
Stoffliche Charakterisierung radioaktiver Abfallprodukte durch ein Multi-Element-Analyseverfahren basierend auf der instrumentellen Neutronen-Aktivierungs-Analyse – MEDINA –
A. W. Havenith (2015), 311 pp
ISBN: 978-3-95806-033-3

Band / Volume 249
Quantitative Two-Layer Inversion and Customizable Sensor-Array Instrument for Electromagnetic Induction based Soil Conductivity Estimation
A. T. Mester (2015), viii, 119 pp
ISBN: 978-3-95806-035-7

Band / Volume 250
Partial Neutron Capture Cross Sections of Actinides using Cold Neutron Prompt Gamma Activation Analysis
C. Genreith (2015), vii, 166, XXXII pp
ISBN: 978-3-95806-036-4

Band / Volume 251
Long Term Aerosol Composition Measurements at the CESAR Tower at Cabauw, NL
P. Schlag (2015), iii, 228 pp
ISBN: 978-3-95806-037-1

Band / Volume 252
Modellbasierte Spezifikationsmethodik zur effizienten Systementwicklung von Brennstoffzellenantrieben
R. Biurrun Sotelo (2015), 255 pp
ISBN: 978-3-95806-038-8

Band / Volume 253
Three-dimensional ray-tracing simulations of convective gravity waves
S. Kalisch (2015), iii, 183 pp
ISBN: 978-3-95806-040-1

Band / Volume 254
First-Principles Study on Pyrites and Marcasites for Photovoltaic Application
T. Schena (2015), 206 pp
ISBN: 978-3-95806-041-8

Band / Volume 255
Glass-Ceramic Sealant Reinforcement for High-Temperature Applications
B. Cela Greven (2015), xi, 119 pp
ISBN: 978-3-95806-042-5

Band / Volume 256
Entwicklung planarer $Ba_{0,5}Sr_{0,5}Co_{0,8}Fe_{0,2}O_{3-\delta}$-Membranmodule zur Sauerstoffabtrennung und Analyse ihres Transportverhaltens
P. Niehoff (2015), VIII, 134 pp
ISBN: 978-3-95806-044-9

Band / Volume 257
Extension of the Reactor Dynamics Code MGT-3D for Pebble-bed and Block-type High-Temperature-Reactors
D. Shi (2015), x, 162 pp
ISBN: 978-3-95806-045-6

Band / Volume 258
Failure Analysis of Thin Film Solar Modules using Lock-in Thermography
M. Siegloch (2015), XIII, 131 pp
ISBN: 978-3-95806-047-0

Band / Volume 259
Relation between growth rate, material quality, and device grade condition for intrinsic microcrystalline silicon:
From layer investigation to the application to thin-film tandem solar cells
S. Michard (2015), vi, 184 pp
ISBN: 978-3-95806-048-7

Weitere ***Schriften des Verlags im Forschungszentrum Jülich*** unter
http://wwwzb1.fz-juelich.de/verlagextern1/index.asp

Energie & Umwelt /
Energy & Environment
Band / Volume 259
ISBN 978-3-95806-048-7